# IMPROVED SOLAR CELLS BY INTEGRATION OF CRYSTALLINE ORGANIC NANOSTRUCTURES

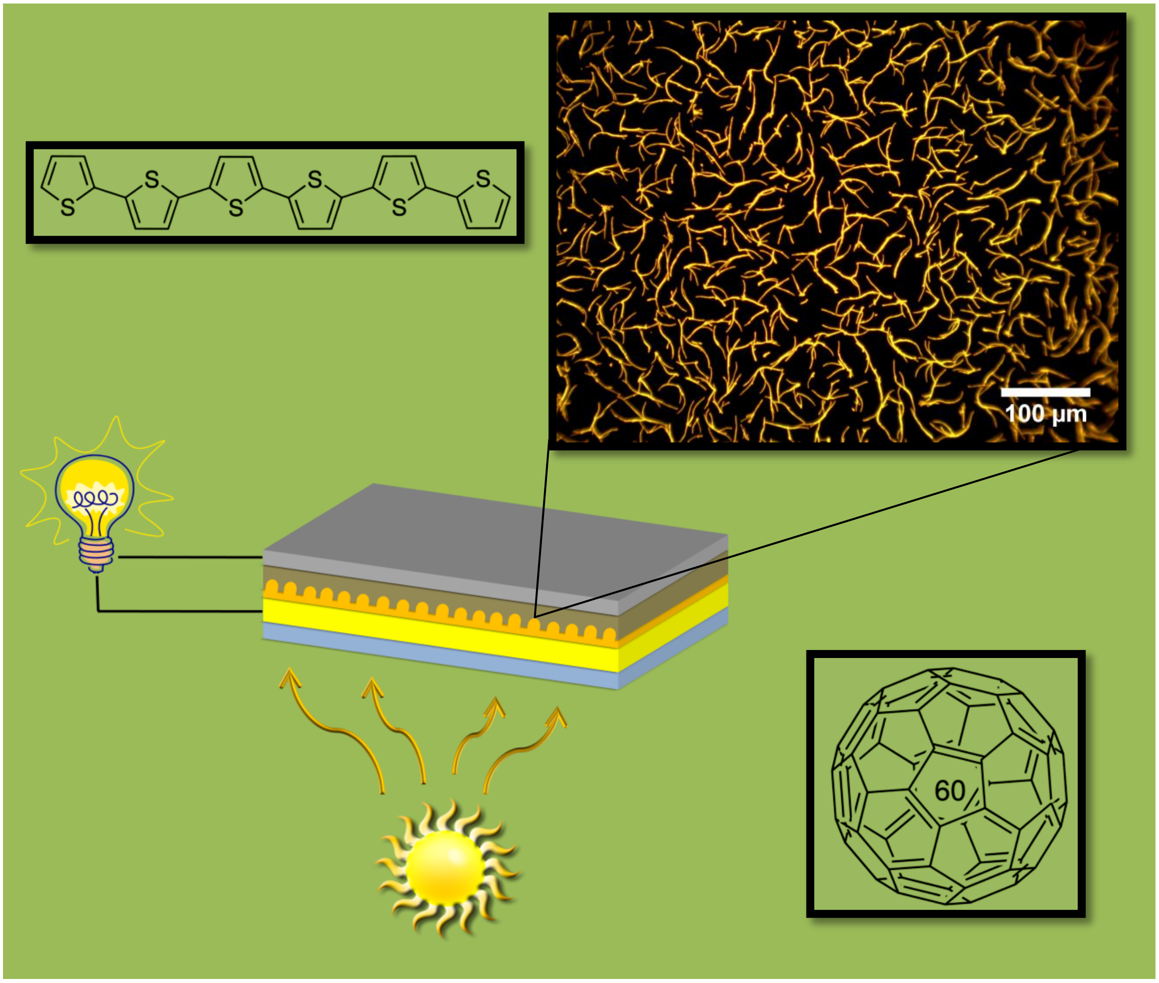

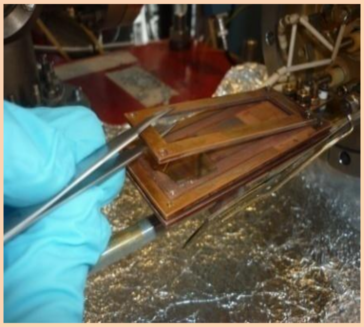

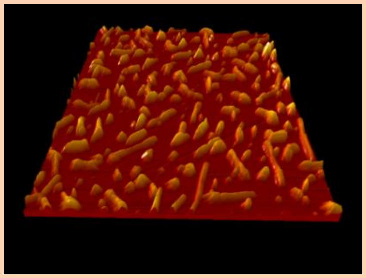

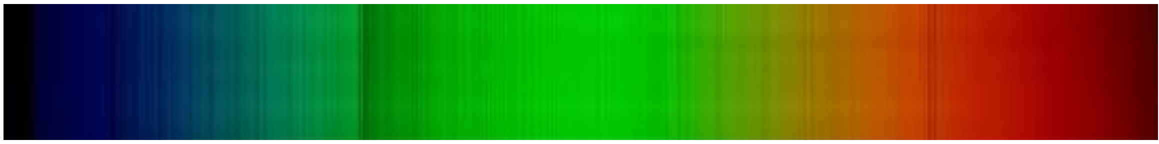

2012

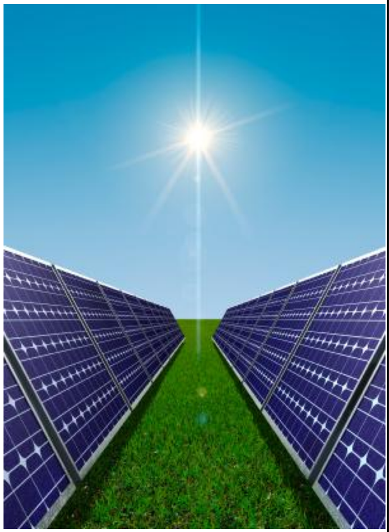

BY ARKADIUSZ JAROSLAW GOSZCZAK

# Improved Solar Cells by Integration of Crystalline Organic Nanostructures

**Master Thesis**
by
**Arkadiusz Jaroslaw Goszczak**

presented to

The Department of Engineering
Mads Clausen Institute
University of Southern Denmark

under the supervision of

**Assistant Professor Morten Madsen**

Sønderborg, June 2012

# Acknowledgement

I would like to express my gratitude to my supervisor, Morten Madsen for the trust he has shown in me and his patience in answering all the questions I had. Without his encouragement, guidance and support from the beginning to the end of this project I would not be able to gain a deeper understanding in the project, the technologies and the equipment accompanying it.

I would also like to thank the PhD student Michal Radziwon for motivating me, providing information and pushing me to my limits in order to finish this project.

Special thank you goes to my mother Ewa Goszczak and my father Lech Goszczak for the financial support without which I would not be able to conduct my Master studies and most importantly for the moral support and encouragement throughout my life.

Last but not least, I offer my regards and blessings to all of those who supported me in any respect during the completion of the project.

*Arkadiusz J. Goszczak*

## SUNLIGHT HARVESTING

*Sunlight provides the energy for almost all life on Earth. It is harvested by plants, including microscopic algae living in water. Photons of sunlight (represented as red dots) enter the food producing regions within the algal cell which act like solar panels. Here the molecules of the green pigment, chlorophyll, are arranged in clusters and absorb the energy of the photons. That energy is used to turn carbon dioxide and water into food, releasing excess oxygen. Algae are eaten by daphnia ('water fleas') and these are caught by roach, small fish which are preyed on by herons. The heron ultimately depends on a vast number of algal cells to supply it with food. The scale of sizes in the painting gradually changes from the magnified part of a single algal cell, covering the lower third of the painting, to the Earth's atmosphere at the top of the painting. The oxygen in our atmosphere was itself created by ancestral forms of algae, beginning millions of years ago, when they were among the most advanced life forms on earth. They changed the ancient atmosphere of the Earth, making it possible for oxygen-breathing animals to evolve. Even today, about 90% of all oxygen production and carbon dioxide use is carried out by algae living in the seas and freshwaters.*

*From a painting by Glynn Gorik, 113 Hemingford Road, Cambridge CB1 3BY, UK (Image and text with permission by G. Gorik ©).*

# Abstract

Organic photovoltaic devices have attracted much attention over the past few years as renewable and clean energy sources, due to their low fabrication cost and ease of processing. Oligothiophene (alpha-sexithiophene: α-6T) is well known as a good hole transport material while fullerene ($C_{60}$) as a good electron transport material making them proper candidates for applications in organic solar cell fabrication. Yet the efficiencies of these organic devices remain low compared to their inorganic counterparts. One of the limiting factors in the efficiency of the organic solar cells is the ability to construct the active layer from crystalline structures, while simultaneously controlling the morphology of these structures. In this research we investigate the controlled structuring of a-sexithiophene (α-6T) deposited via organic molecular beam deposition (OMBD) on Au covered glass substrates by tuning the substrates temperature. We report the growth of α-6T as polycrystalline thin films at room temperature to the so-called nanofibers at temperatures higher than 100˚C. The present study found that these structures are not yet applicable for solar cells as the fabricated devices show ohmic behavior on Au substrates, in comparison to cells made on ITO covered with PEDOT:PSS where photovoltaic effect was observed.

# Table of Contents

# Chapter 1
# Aims and outline

## 1.1 Aims

The great potential of solar energy is apparent considering that the total amount of energy from sunlight, which strikes the earth in one hour (445 EJ (1)), is comparable to the worlds total energy consumption within one year (550EJ in 2010 (2)). In order to harvest this energy the concept of solar cells was employed. Today, the solar cell industry is completely dominated by the silicon based solar cells, covering more than 80% of the world's wide solar cell production (3).

Solar cells made from organic materials is a rather novel technology which typically incorporates nanostructured blends (bulk-heterojunction) of electron donor and acceptor materials, which efficiently separates electron-hole pairs generated during photo-excitation (4), (5). Among many organic materials poly- and oligothiophene (α-6T) and fullerene ($C_{60}$) show intriguing properties for solar cells application and are constantly under the scope of solar cell research (4), (6), (7).

These solar cells typically show efficiencies which are lower than commercially available cells, however, their unique advantages lie in their low cost and tuning of the material properties through chemical synthesis. Although this method has resulted in the highest efficiencies reported for organic solar cells, the bulk heterojunction morphology suffer from recombination of charge carriers in isolated materials (8), i.e. material which is not in contact with the electrode, which limits their overall performance. To overcome this problem, the morphology of the interpenetrating network of mixed n- and p-type organic materials needs to be controlled at the nanoscale.

It is the final aim of this thesis to produce solar cell structures with control over the morphology of the organic layer at the nanoscale. As a starting point we wish to investigate the growth behavior of a-sexithiophene (α-6T). In order to do so an appropriate layer that will allow the structuring of the material is required. α-6T on mica presents similar growth behavior to para-hexaphenylene (p-6P) on mica (9), whereas on the other hand growth of p-6P on gold (Au) shows similar growth behavior as on mica dependant on the Au thickness (10). Since there is relevance on the growth behavior of p-6P and α-6T, Au is the starting layer of choice in order to observe any effect of α-6T structures. Additionally deposition of a thin layer of gold on glass substrate provides enough transparency for light to pass to the active layer and can serve as an anode for solar cell structures.

By depositing α-6T via organic molecular beam deposition (OMBD) we intend to inspect the dependency of the nanostructure morphology on the substrates temperature. This investigation consist the first milestone of the research.

After this investigation we aim to produce a solar cell structure using the results from the previous investigation. In this part the Au layer will serve as the anode for the structure, α-6T as the donor material while using for acceptor material a layer of $C_{60}$. To complete the structure aluminum (Al) layer is intended to be used as cathode, deposited by thermal evaporation. This last investigation consists the second milestone of this research.

## 1.2 Outline

In Chapter 2 we start by explaining why solar energy is important. We present the background theory of solar cells that is mainly based on inorganic solar cells, showing how they operate and how solar energy can be converted into usable energy. We point out the important characteristics of the solar cells used for general solar cell comparison and characterization. Additionally we present the losses that prevent the solar cells converting solar radiation into 100% usable form.

In Chapter 3 we show a small part of the history that lies behind solar cells. We point out the available technologies of inorganic and organic solar cells and what efficiencies these technologies offer nowadays.  We finish the chapter by doing a general comparison of inorganic versus organic solar cells.

In Chapter 4 we introduce the organic solar cell structures. We show the main differences between inorganic and organic, while indicating the key advantages and disadvantages of organic solar cells, what factors lead to the poor efficiencies of the organic solar cells and how those can be overcome. As organic solar cells are our key interest we go into more detail on how these operate and what mechanisms take place in order to convert solar radiation to consumable energy. Some materials that are commonly used for organic solar cells are presented, as well as the reason why we selected the specific donor and acceptor materials. We conclude the chapter by showing the desired result of this work and how this involves the donor/acceptor materials.

Chapter 5 is dedicated to the experimental work done in this research. We begin by showing how the anode and cathode contacts have been created while pointing out the reason for using different deposition methods for these contacts. We continue by introducing the concept of organic molecular beam deposition (OMDB). We present the OMDB setup that was used for this research in more detail. We showing the final modified setup that was used, present the obstacles that we came upon and indicate the changes that were applied in order to overcome these problems and end up to the final OMDB setup on which we proceeded with further experiments.

Chapter 6 is dedicated to the two milestones of this research, which are regarding the structural growth behavior of α-6T on Au substrates and the integration of the results into solar cell structures. The first part of the chapter is devoted on the work done around structuring α-6T material. We present growth of α-6T at different substrate temperatures while showing some key points of interest. Additionally we do a small comparison of the initial OMDB setup and the final modified setup regarding the effects in the α-6T deposition and growth. The second part is related to the implementation of the findings to a solar cell structure. The fabricated solar cell structures on Au substrates are shown as well as related issues to their function. We present I-V characteristics obtained for a bilayer, α-6T:$C_{60}$, solar structures made on Au covered glass and on ITO covered with PEDOT:PSS that was used a reference.

We finish this report by deriving conclusions and making suggestions for future work.

# Chapter 2
# Theory of Solar Cells

## 2.1 Introduction

The sun is the biggest energy source of earth. Practically every living species relies on the sun for food and warmth. What is of importance though is that solar energy can be harvested in order to produce electrical energy. This can be achieved with the use of solar cells.

A solar cell is an electronic device that can gather and directly convert sunlight into consumable energy. When multiple solar cells are assembled together they are often referred to as solar panels. Solar panels are used in order to power buildings, vehicles, even towns (11), while solar cells or small solar modules can be used to provide supply to domestic devices like lamps or they can be used as chargers for small devices, for example Mp3's or mobile phones.

Of course the applications do not stop here, as the technology grows bigger fields that this technology can be adopted increase in parallel.

## 2.2 Why solar energy?

The majority of the world's current electricity supply is generated from fossil fuels such as coal, oil and natural gas. Due to increase in population over the past years, the demand in energy increases year by year, the resources decrease while the prices of these fuels go higher (12). This together with the huge environmental impact this has, leaded the power industries into alternative energy sources such as wind, water and sun. Many researches have been conducted in order to prove the most efficient solution of these three, but the most efficient solution is not always the easiest applicable in everyday life (13).

Between these three competitors the answer to which one is better is objective, but we would like to express our personal opinion on this matter by putting a simple question. Suppose you have a pure electric car (no gas or petrol) that gets its supply from stations that in turn draw power from wind or water generators. The weather is sunny and with plenty of wind, if you are in the middle of the road without any accessible stations close by and you run out of "fuel", what would be your preference to have on the roof a solar panel or a wind mill?

Of course there is much debate on this question but it was made just to prove a point and this was that solar energy nowadays is easily adoptable almost everywhere (Figure 1).

Figure 1. (a) Solar powered air-conditioning system in Toyota Prius (www.toyota.com), (b) Solar modules on bags (www.konarka.com) and (c) Solar panels on buildings, here at the University of Southern Denmark Campus Sønderborg.

## 2.3 Solar cell structure

A typical solar cell (Figure 2) consists of an antireflection coating that constrains the incident light within the solar cell and prevents it to simply bounce off the surface, this coating is usually made of a transparent or semi transparent material like glass or plastic in order to allow light to pass into the cell.

The main "body" or base of the solar cell is made of a material that allows the generation of positive and negatives charges when light is absorbed by the material.

The base additionally offers the driving forces that can separate the generated positive and negative charges (electron-hole pair) and push the charges through an external electric circuit to do work and return to the solar cell.

The collection of the charges is done by contacts made of good conductor material located on the top and bottom part of the solar cell. The whole assembly then is embedded in some type of transparent usually housing that seals the solar cell and prevents any residuals entering and affecting the solar cell operation.

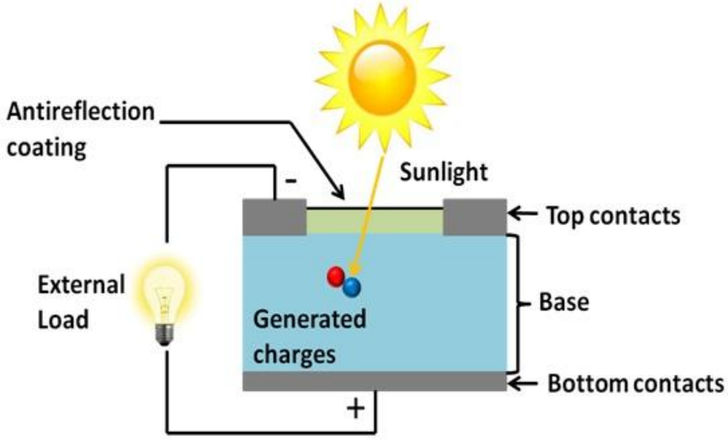

Figure 2. The sketch illustrates the cross section of a typical solar cell, indicating the basic parts composing the solar cells structure. Upon light absorption, charges are generated in the base where they are separated, and collected by the contacts.

## 2.4 Solar cell operation principle

Capturing the light, generating charges and separating them are not enough in order to give rise to power generation. It is well known that power is generated with the generation of voltage and current. To do so in a solar cell a process known as the "photovoltaic effect" is adopted, that is the creation of voltage or electric field in a material upon exposure to light. Let us take the part of the solar cell that is responsible for this, that is the base we mentioned in the previous section.

Imagine two semiconductor materials sandwiched together. Semiconductors are used as materials for fabrication of solar cells as they can provide electrons and holes upon small excitation, this though is a simplified explanation as the reason of why we use semiconductors instead of insulators or conductors lies more deep in the theory of the band gap of the materials (14).

From this two sandwiched semiconductors one is doped so it forms an n-type material, meaning that the semiconductor will have an excess in electrons available for conduction, and one is doped so it forms a p-type material, meaning that it will have excess in holes available for conduction Figure 3.

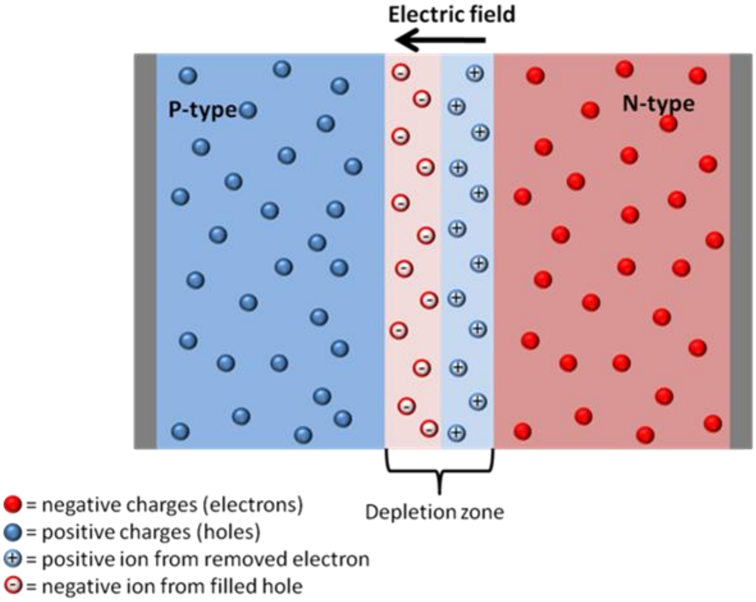

Figure 3. The sketch shows the P-N junction formation upon contact of two doped semiconductors. Electrons (red) tend to diffuse to the p-type region while holes (blue) tend to diffuse to the n-type region. The depletion region that is formed after some charges have diffused stops further diffusion. (Image after (23))

By doping pure silicon with Group V elements from the periodic table, such as phosphorus, extra electrons are added that become unbonded from individual atoms and allow the compound to be an electrically conductive n-type semiconductor.

Doping with Group III elements from the periodic table, which are missing an electron, creates "broken bonds" (holes) in the silicon that are free to move. The result is an electrically conductive p-type semiconductor.

At the point that those n and p type doped semiconductors are connected a depletion zone is created, as some electrons near the p-n interface diffuse to the p-type region and some holes diffuse to the n-type region. This depletion region creates an electric field opposing the diffusion process for both electrons and holes. This electric field acts like a diode, allowing electrons to flow from the p-side to the n-side but not the other way around.

Since no more electrons can transfer through the depletion zone we can state that an equilibrium state is achieved. In the case of equilibrium there is no current flow in our circuit. In order to have current flow this equilibrium has to be “disturbed”.

It is well known that sunlight is made up of packets of energy called photons (15). Upon incident light on the solar cell, a portion of these photons can be absorbed by the semiconductor material. When a photon is absorbed, the energy of the photon is transferred to an electron in the semiconductor.

Upon light absorption an electron is knocked off to the conduction band leaving a hole behind. If this happens close enough to the junction the electric field will then separate the charges, sending the electron to the n side and the hole to the p side. The equilibrium now has changed.

If we connect an external load to our circuit we actually provide a path for the electrons to pass and fill a hole on the other side of the junction. The electron flow provides current and the electric filed provides the voltage (16) hence we have power.

## 2.5 Photovoltaic characterization

Photovoltaic cells can be modeled as a current source parallel with a diode. When there is no light present there is a relatively small amount of current flow, called the dark current. The dark current flows in the opposite direction and is caused by a potential between the terminals. As the intensity of incident light increases, current is generated by the photovoltaic cell. Additionally to this equivalent circuit there are two resistances present, series and parallel. The series resistance comes from the cell’s material resistance to the current flow as the cell is not a perfect conductor, while the parallel resistance is caused by leakage of current through the cell (17).

The equivalent circuit for a typical solar cell is shown in Figure 4 as well as the I-V characteristic of such cell under dark and illumination. Where it can be observed that upon illumination there is shift of the curve with indication in current flow.

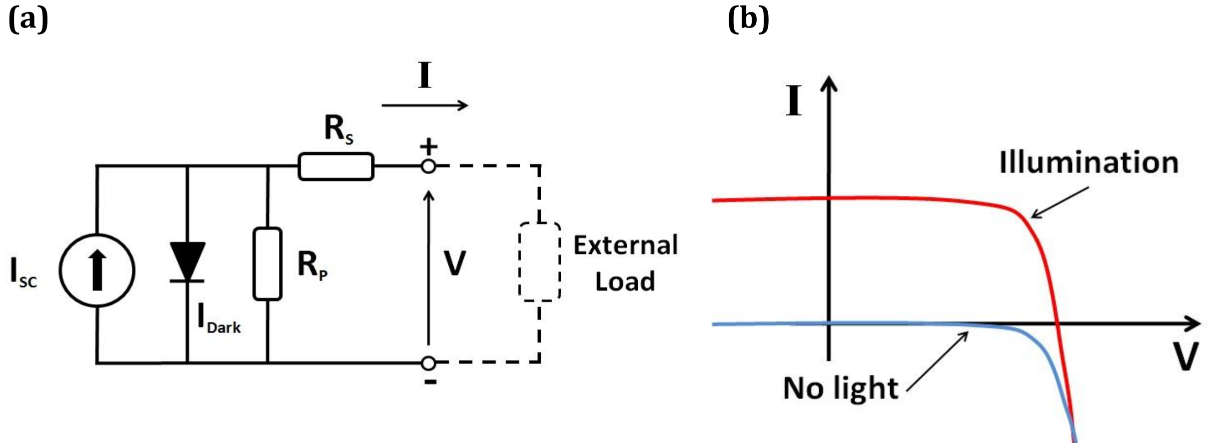

Figure 4. (a) Equivalent circuit model for a photovoltaic cell connected to a load, and in (b) The relevant I-V curve of an ideal cell under no light and under illumination. (Images after (17))

As it was described above when light is absorbed by the solar cell the equilibrium within is disturbed, then two important phenomena can be observed.

When the terminals of the solar cell are isolated the voltage developed has its maximum value, this is called *open circuit voltage* and is denoted as $V_{OC}$. When $V_{OC}$ is maximal there is no external electric current flow between the terminals.

With the presence of load and the terminals connected there is current flowing through the circuit, this is the *short circuit current*, denoted as $I_{SC}$. Maximum current occurs when the voltage across the terminals is zero.

Under constant illumination intensity the solar cell will deliver a voltage from 0 to $V_{OC}$ and current that is given by $I=V/R_L$ where $R_L$ is the load resistance, therefore from I-V measurements one can obtain the I-V characteristic of a solar cell (18), as shown also in Figure 5, for convention the axes are reverted.

The power of the solar cell at maximum current and voltage, $I_{SC}$ and $V_{OC}$ accordingly, is zero. The solar cell can deliver the largest output power at the point where the current and the voltage get maximized, $I_m$ and $V_m$ accordingly.

Graphically expressed maximum power is the point in the I-V characteristic of the solar cell where the largest rectangle can be found beneath the curve (rectangle $A$ in Figure 5) and it is generated at the operating point which forms the "knee" in the curve ($P_{MAX}$) (17).

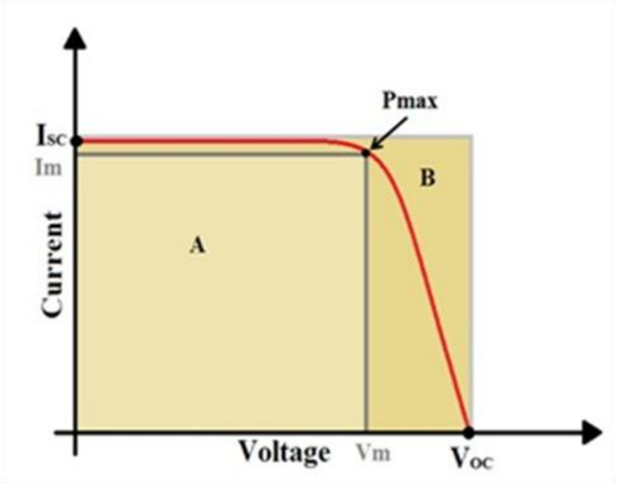

Figure 5. I-V characteristic of a solar cell denoted with the red line. Maximum power can be delivered where the current and the voltage get maximized, $I_m$ and $V_m$ accordingly.

A commonly used parameter that characterizes the maximum power of the solar cell is the fill factor, FF, which is the maximum power from the solar cell to the product of $V_{OC}$ and $I_{SC}$ (19).

$$FF = \frac{I_m V_m}{I_{SC} V_{OC}} = \frac{P_{max}}{I_{SC} V_{OC}} \quad (1)$$

In order to compare the performance of one solar cell to another, or even to check how good a fabricated solar cell is, one needs to look at the efficiency of the solar cell. The efficiency ($n$) is defined as the ratio in percentage of the maximum output power ($P_{max}$) from the solar cell to the input energy of the sun ($P_{in}$) (17).

$$n = \frac{P_{max}}{P_{in}} = \frac{I_m V_m}{P_{in}} \quad (2)$$

These four quantities $I_{SC}$, $V_{OC}$, FF and $n$ define the performance of a solar cell, and are thus the key characteristics needed to test and compare a solar cell.

Of course it should be mentioned that those are not the only parameters that one will face when analyzing solar cells but instead there are many more parameters in correlation to the above four mentioned, but since it is not the intent of this paper to analyze them, the reader is advised to refer to (17) and (20) in order to get a more in depth detailed knowledge.

## 2.6 Losses

When solar radiation strikes a solar cell not all the incident energy is absorbed and converted into useful energy. This is because of some loss processes that take place in and on the solar cells, in Figure 6 we can see these loss processes.

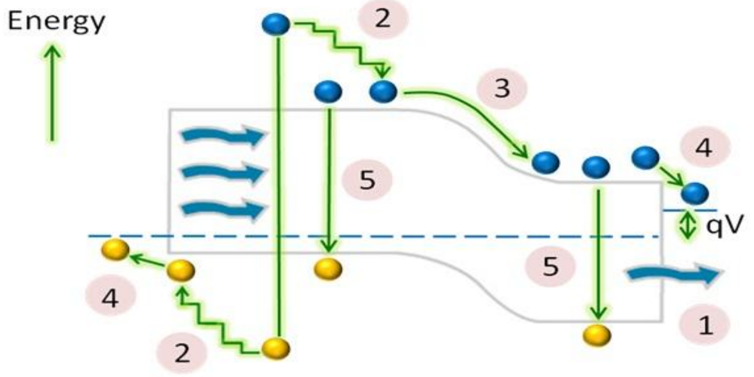

Figure 6. Typical solar cell loss mechanisms. (1) Non-absorption of below band gap photons, (2) lattice thermalisation loss, (3) and (4) junction and contact voltage losses and (5) recombination loss. (Image after (17))

From the 100% of the sun's total incident energy on a solar cell, 18% just passes through the solar cell without any effect to the solar cell structure. Materials have certain bandgap energy, this means from the incident light only photons that have sufficient energy to knock off electrons from the valence band to the conduction band in the material will be used (1), this fact combined with the junction and contact voltage losses (3) and (4), as well as the recombination losses (5), give an approximate energy loss of 10%. Excited electrons can lose energy to the materials lattice in the form of heat through a process called thermalisation (2), here the lost energy is approximately 47%. The remaining 25% energy is converted in current which is also the approximate efficiency value for silicon solar cells (21), (22).

In general the efficiency of a solar cell depends on the spectrum and the intensity of the incident light, as well as from the temperature of the solar cell, therefore to test as solar cell or be able to compare solar modules, standard test conditions have been developed (17), (23).

The standard test conditions (STC) for solar cells in the photovoltaic (PV) industry specifies a temperature of 25°C and an irradiance of 1000 W/m$^2$ with an air mass (AM) of 1.5 spectrum. Those parameters correspond to the irradiance and spectrum of sunlight incident on a clear day upon a sun, facing 37° tilted surface, with the sun at an angle of 48.2° above the horizon (24) Figure 7 (b). It has to be noted that the average sun power density on Earth is 170 W/m$^2$, which is roughly five times lower than the testing conditions.

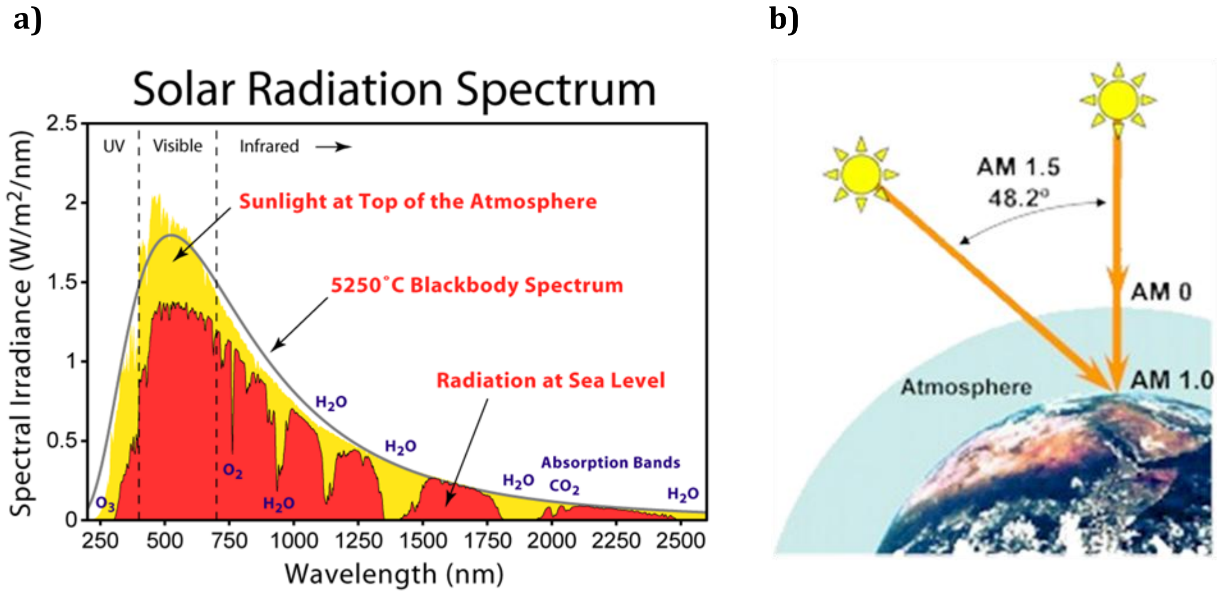

Figure 7. (a) Solar cell irradiance above Earth's atmosphere and at the sea level (83). (b) The air mass (AM) which is a measure of how far light travels through the Earth's atmosphere. AM0 is the solar irradiance in space, AM1 represents solar irradiance directly overhead and AM1.5 is the standard solar cell testing.

# Chapter 3
# The Battle for Efficiency

## 3.1 Introduction

In 1894, Charles Fritts prepared what is believed to be the first solar cell by using junctions formed by coating selenium (a semiconductor) with an extremely thin layer of gold (20). Later it was Russell Ohl in 1941, which discovered the silicon solar cell with better efficiency from the previous mentioned (25). But it was the three American researchers Gerald Pearson, Calvin Fuller and Daryl Chapin, in 1954 that “fired up” the solar cell evolution by making an array of several silicon strips that under sunlight illumination produced power. They had created the first solar panels. But the efficiencies were still low.

Since then there have been many investments in the solar cell industry in order to increase efficiencies of solar cells. The chart in APPENDIX 1 is showing how the efficiency and the technology of the solar cells have been evolving over the years until now according to the National Renewable Energy Laboratory (NREL).

Let us just point out here that the development and greater interest in organic solar cell has begun after 2000. In Figure 8 a zoom-in on the chart in APPENDIX 1 indicates how the research in organic solar cells (orange dots) and their efficiencies increase year after year.

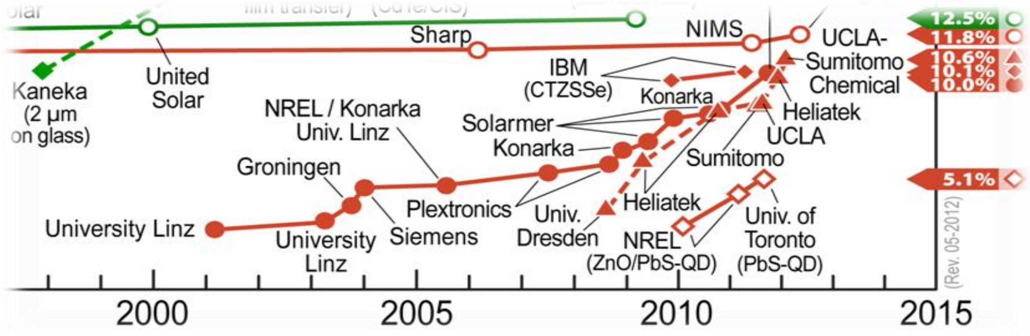

Figure 8. Zoom-in on the organic solar cell records in efficiencies (orange dots) over the years according to NREL.

## 3.2 Inorganic solar cells

Wafer based crystalline Silicon solar cells (Figure 9 (a)) produce efficiencies of the order of 15-24.5% (26), (27). These types of solar cells are based on the formation of a p-n junction as mentioned in the previous chapter. This is done by introducing dopants into the silicon in order to from the p-n junction, covered by an antireflection coating and contacted with Ag grid on front and Al layer on the rear. This type of solar cells even though they offer good efficiencies, they usability is limited to photovoltaic panel like structures, so they can be mounted in fields or roofs, in general areas with rather flat surfaces as silicon wafer like solar cells are thick (28), fragile and inflexible.

The demand of being able to implement solar panels at any type of surface, flat and non-flat, big surface areas or small and on any type of material like cloth, paper ect. has given rise to the need for the fabrication of flexible solar cells. Fan et al. in 2009 reported a type of solar cell consisting of single-crystalline CdS (n-type) nanopillars (Figure 9 (b)) on anodized alumina foil covered with CdTe (p-type) and embedded in flexible polydimethylsiloxane (PDMS) (29). But this type of solar cells are complicated and expensive to produce massively, additionally the efficiency of these flexible solar cells remains rather low <10%.

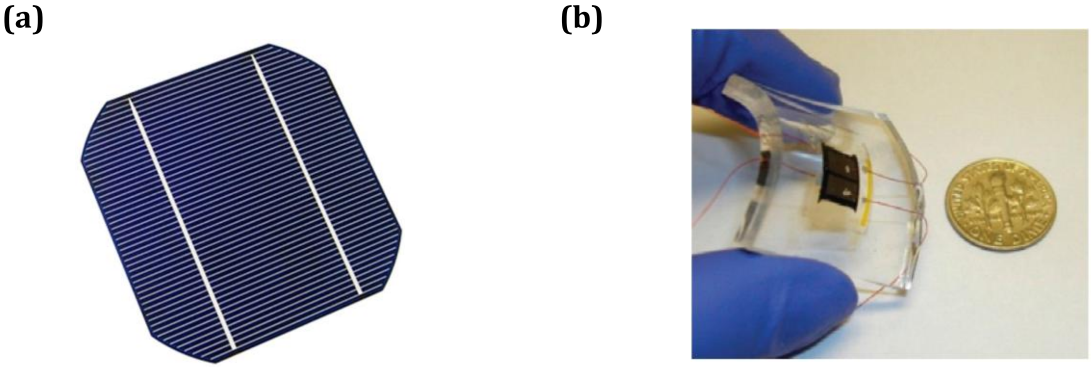

Figure 9. (a) Silicon based solar cell with efficiency up to 18% (www.cnbestsolar.88582.net) and (b) flexible CdS nanopillars solar cell embedded in PDMS (29).

Higher efficiency solar cells have been fabricated by introducing the multi-junction structures (30). The National Energy Laboratory recently certified that its solar cell can operate at 40.9% efficiency, a significantly higher efficiency than typical silicon solar cells (31).

The aim with multi-junction solar cells is to increase the efficiency of a solar cell by increasing the solar spectrum range that the device can absorb. This is done by adding more cells of different band gap to one cell stack and connecting them together so they operate as one. In this way one sub-cell absorbs a part of the solar spectrum letting other parts to pass to the next cell where again some part of this spectrum is absorbed and some passes to the next and therefore making use of a broader part of the solar spectra (Figure 10). Even though we gain efficient solar cells from this type of technology we once more lose flexibility and most probably the production cost of this type of solar cells will be high.

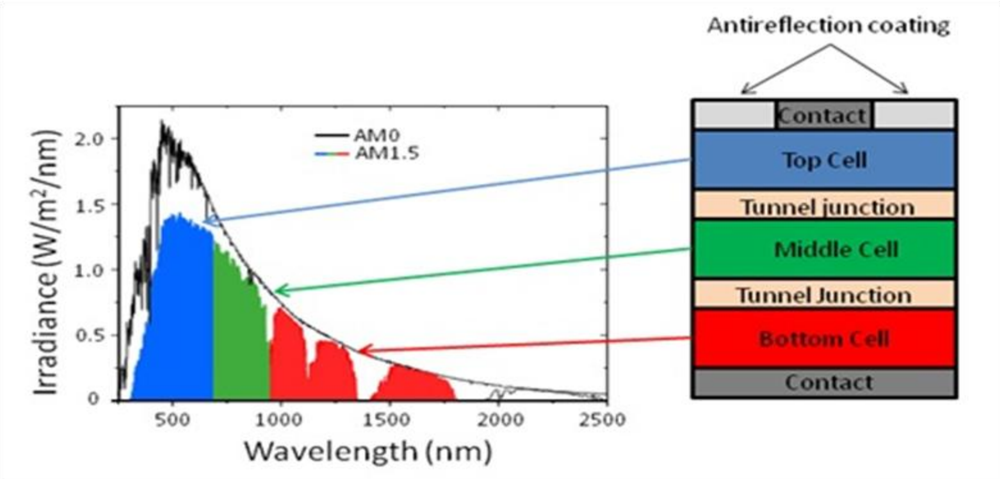

Figure 10. On the left hand side a graph of spectral irradiance vs. wavelength λ over the AM0 solar spectrum, together with the maximum electricity conversion efficiency for every junction as a function of the wavelength for AM1.5. On the right hand side a sketch showing a multi-junction solar cell pointing at which part of the spectrum each cell absorbs.

The above mentioned are only a small portion of the huge solar cell industry and the technologies available, but as it can be seen efficiency and flexibility are constantly alternating.

There has to be a type of solar cells that will have good efficiencies, offer flexibility, will allow fast prototyping of the solar cell modules, has low production cost in order for the solar modules to have an attractive sell price and the energy consumption during the production will be kept in minimum levels.

## 3.3 Organic solar cells

Organic solar cells are a rather novel technology, they research and developed increased from around the year 2000 until today with their efficiencies constantly rising. Organic solar cell technology though does not have efficiencies comparable to their counterpart crystalline silicon, around 5-9% efficiency as compared to 17-20% for silicon cells.

Konarka recently got certified for an organic solar cell, Figure 11 (a), that reaches 9% efficiency (32). Their solar cells are being produced with a method called roll-to-toll printing (Figure 11 (b)).

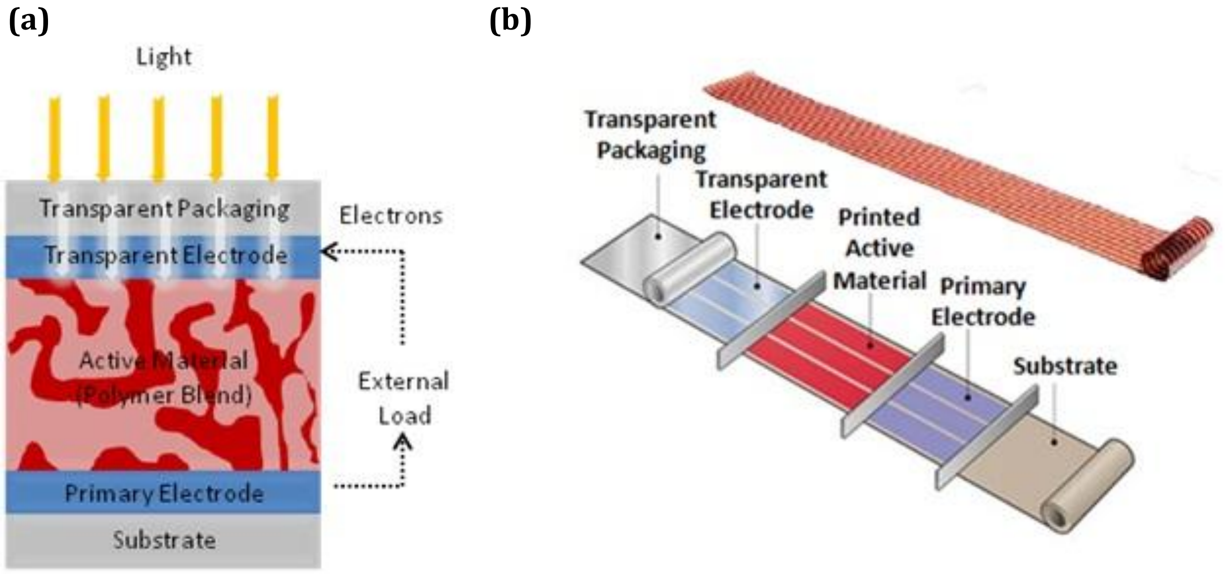

Figure 11. In (a) a sketch representing Konarkas bulk-heterojunction organic solar cell with the active material formed by a blend of the donor-acceptor materials. In (b) the roll-to-roll process showing the in-series production of the solar cell and right above it a produced solar cell sheet.

The roll-to-roll method is very similar the method that is used to print the newspapers, where instead of paper a big thin aluminum foil rolls through some rollers and the material needed to form the solar cell p-n interface is deposited like the ink in the inkjet printers we have in our homes. The active layers are deposited in series without interrupting the production. In this way they are able to produce rapidly big, lightweight, flexible solar panels in ambient environment and with relatively cheap production cost if we consider the equipment and the operational energy for it, after all we are talking about renewable energy. Additionally organic solar cells can be produced at low temperatures unlike crystalline silicon where high temperatures are required for doping the materials (33).

In general organic solar cells cannot compete with silicon, at least for now, but due to their flexibility they can open new fields of applications as powering small mobile devices such as MP3 players or mobile phones, or even they could be combined with electronic circuits to form some kind of self-sufficient power microsystem.

Already organic solar modules are being produced for outdoor applications in order to power houses, even solar bag panels have been made in order to charge up or power devices that require small power (34).

Konarka of course it is not the only company producing flexible organic solar panels among those, two others that produce high efficiency organic solar modules are, Mitsubishi Chemicals that holds the lead in flexible organic solar cell efficiency with 10% (35) and Solarmer Energy Inc. with efficiencies of the order of 8.5% (36).

Looking at the organic solar cells efficiencies one may wonder since they are low why we should be investigating further this kind of technology and not try to combine the existing ones with good efficiencies and flexibility. Table 1 shows some key differences that help us make a distinction between organic and inorganic solar cell technologies.

Table 1. Organic vs. Inorganic solar cells main specifications comparison.

| | Production cost | Production Energy | Efficiencies | Operation Lifetime | Flexibility |
|---|---|---|---|---|---|
| Inorganic | Low | Low | > 15% | ≈30years (37) | Limited |
| Organic | High | High | ≤ 10% | <<10years (38) | Yes |

Taken into consideration that organic solar cells have recently started to "blossom", the fact that within ten years approximately the efficiency of those cells has increased to 10% and that many funds are being spent on research and development in this area, we can state that the future for the organic solar cells look bright.

# Chapter 4
# Understanding Organic Solar Cells

## 4.1 Introduction

In order to understand why though the past ten years most research has focused on developing organic solar cells and they remain with low efficiencies we should look deeper in the solar cell structure where the things are a little bit different compared to inorganic.

The primary difference between organic compounds and inorganic compounds is that organic compounds always contain carbon while most inorganic compounds do not contain carbon. Also, all organic compounds contain carbon-hydrogen or C-H bonds (39). But there are more important differences that need our attention.

In an inorganic solar cell, when light is absorbed, weekly bound charge carriers (an electron and a hole) are generated that can be easily separated by the p-n junction within the cell. In an organic solar cell on the other hand incident light creates strongly Coulomb bound charge carriers pairs known as excitons.

Due to the strong binding energy excitons are harder to separate. In general the Coulomb binding energy between charges relies on the dielectric constant of the materials, high dielectric constant equals low Coulomb binding energy. Most organic materials have low dielectric constant compared to inorganic materials hence the Coulomb force is bigger (40).

Another significant difference is that silicon solar cells are primarily made of crystalline silicon, in which atoms are ordered (almost perfectly) well. This leads to the fact that the charges can travel rather fast in the material after they have been photogenerated.

Organic materials are usually amorphous leading in poor charge carrier mobility (41), of course this does not exclude the fact that crystalline organic materials exist. Hence one possibility of improving the charge carrier mobility would be to fabricate crystalline structured organic solar cells.

Generally speaking crystalline materials have periodic structures, the band model applies, and there is delocalization of electrons in the electron conduction band and holes in the valence band. This is the case with doped silicon. Amorphous materials have localized charges in the form of radical ions which move by hopping from molecular site to molecular site.

This process is intrinsically less efficient than in crystalline semiconductors, which is reflected in the lower mobility of charge carriers (Figure 12). A significant advantage of the organic materials is that they properties are rather easy to manipulate chemically and synthesize substances that allow the fine tuning of the absorption range and of the charge transport properties (42).

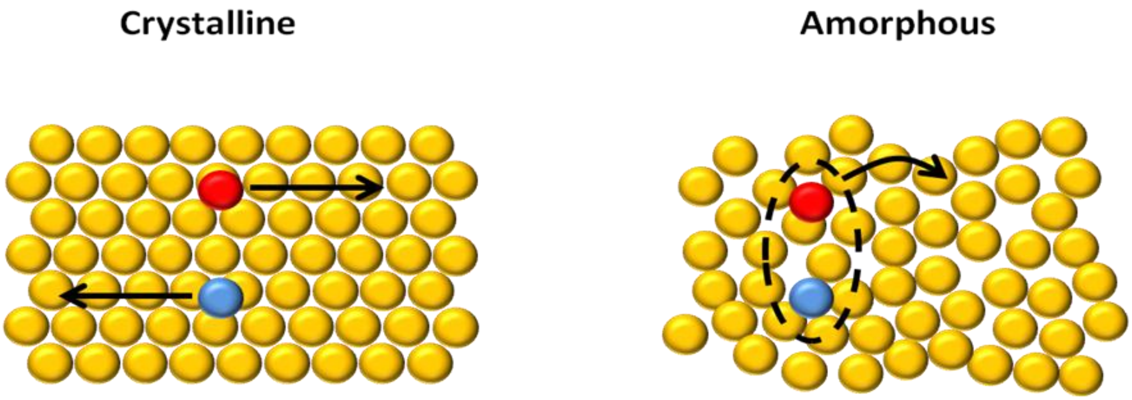

Figure 12. Atomic structure of crystalline vs. amorphous materials. The atomic structure affects the carrier mobility as well as the flexibility of the material. In crystalline material the electron-hole pair can be easily separated and it is easier to move in the material, the strongly bound electron-hole in amorphous organic material is harder to separate thus moves together through the material, a slower process that gives more time for the exciton to lose energy.

## 4.2 Operation principle of organic solar cell

Before going any further explaining organic solar cells we should make a small distinction here. In inorganic solar cells light is incident from the n-type material side, if the energy of the photon is high enough it will free an electron, which in turn leaves a hole behind. The electron and the hole are later split by the internal electric field.

In organic solar cells upon incident light the electron is transferred from a p-type hole conducting material onto the n-type conducting material, therefore the notation of donor (D) and acceptor (A) with respect to the electron transfer has been introduced (43).

We know from the above mentioned that when light strikes an organic solar cell an exciton is generated. This exciton has to be split into an electron and a hole, then the electron has to be guided to the external circuit in order to have current running through it. Excitons within organic solar cells move by dissociation Figure 13.

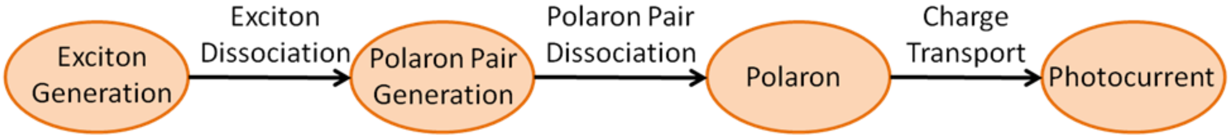

Figure 13. The sketch is illustrating the steps that a photogenerated exciton follows in an organic solar cell, from the generation of the exciton to the production of photocurrent.

When an exciton is generated it diffuses into the material in order to split, ideally it should reach the interface of the solar cell that is the area where the donor and acceptor material meet. At that interface the energy is higher than the exciton binding energy, so the exciton dissociates into an electron on the acceptor and a hole in the donor. Yet the electron-hole pair is still Coulomb bound, now called a polaron pair. If an exciton does not dissociate into a polaron pair then it can recombine and lost. This polaron pair has to dissociate further but in order to do so an electric field is needed. This is provided by the electrodes that are chosen to have different work functions. The field separates the polaron pair hence charges are transported through the external circuit giving rise to current (44).

## 4.3 The Donor/Acceptor interface

Above it was mentioned that the separation of charges is done at the interface where the two materials donor (D) and acceptor (A) meet. This reminds us in a way the operation of an inorganic solar cell and the separation of charges at the p-n junction, but here the physical process is different. Two terms that have to be clarified are the ionization energy and the electron affinity. The ionization energy is the minimum energy required to remove an electron from an atom or molecule, while the electron affinity is the opposite where instead of removing an electron we add one. Simply put the electron affinity describes the *likeliness* of an atom to accept an electron Figure 14.

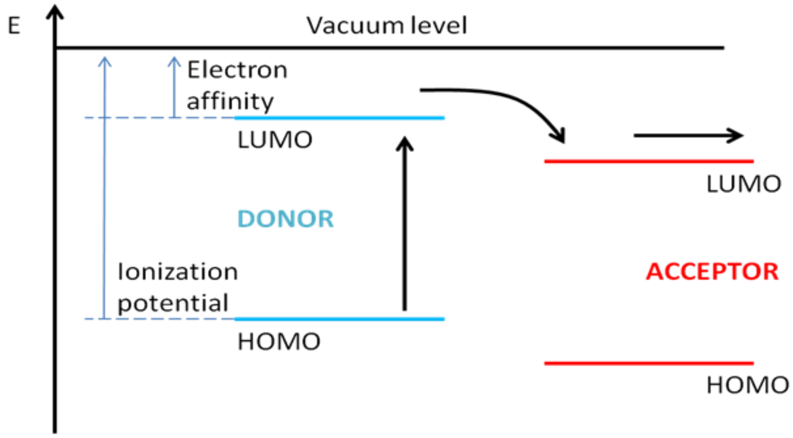

Figure 14. Energy levels in the donor and acceptor interface, with the arrows denoting the movement of an electron.

The ionization potential of a donor material and the electron affinity of an acceptor material form a potential difference that causes strong local electric fields which leads to dissociation of the electron-hole pairs (45).

In this concept the ionization level and the electron affinity of the donor should be lower than that of the acceptor otherwise it would not be able to give an electron and accordingly the electron affinity and ionization potential of the acceptor should be larger than the electron affinity of the donor otherwise the electron would recombine.

## 4.4 Organic solar cell architectures

The above mentioned case is applicable for heterojunction structures. The first organic solar cell was based on single layer structures. In this case a layer of organic material is sandwiched between two metal electrodes with different work functions.

The difference in work functions creates and electric field in the organic layer. Upon absorption of light from the organic layer excitons are formed that diffuse towards the contacts since the field is not enough to separate them. When an exciton reaches a contact where a depletion zone has been formed it may be broken up to offer separated charges, Figure 15. But because for most organic materials the exciton diffusion rates are small (≈10nm) only those excitons generated within this distance can contribute to the photocurrent (43), (46).

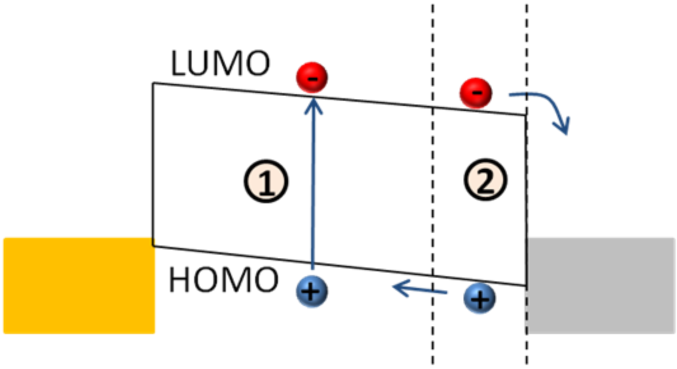

Figure 15. Schematic of the energy-band diagram for a single organic layer device sandwiched between two metal contacts with different work functions. The electric field created due to difference in work function of the contacts produces an electric field. The photogenerated excitons (1) can diffuse towards the contacts and dissociate only in a thin depletion layer (2). (Image after (43) and (46)).

The limitation here is that the absorption of incident light in organic materials relies on the thickness of the active layer, approximately 100nm (47), (48). This is much more than the 10nm diffusion length of the excitons, resulting in poor efficiency devices.

Most advances nowadays and improvements in organic solar cells operation and efficiency are due to the introduction of the heterojunction architecture. In this type of devices two organic materials with different properties are used in order to structure the device, again sandwiched between two electrodes with different work functions. The key difference between the previous single layer devices is that here exists an additional site where the exciton can be separated, this is the interface formed between the two materials.

In the bilayer heterojunction device Figure 16, an acceptor and a donor material form a planar interface in between them. It is at this interface where the separation of the charges occurs due to the differences in the ionization potential and the electron affinity of the adjacent materials. Upon absorption of a photon in the donor material, an electron is excited from the HOMO to the LUMO level of the material (Coulomb bonded).

If this happens close to the acceptor molecule then the internal electric field can separate the charges with the electron hopping to the acceptor, thus the electrons travel in the acceptor material and the holes travel in the donor material, lowering in this extent the probability of recombination.

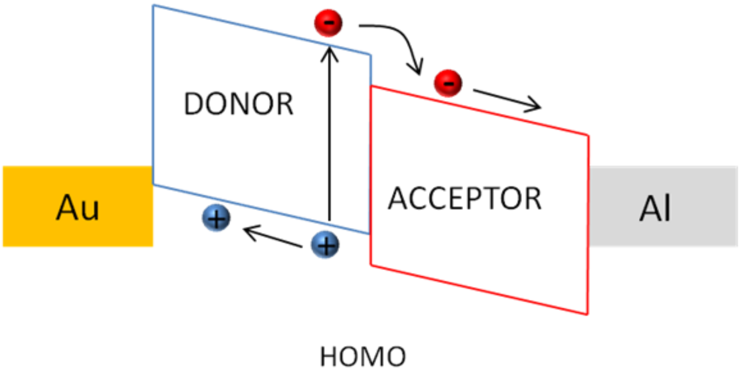

Figure 16. Schematic of a bilayer device. The donor contacts the higher work function material, while the acceptor the lower work function material. Photogenerated excitons can only be dissociated in a thin layer at the heterojunction and thus the device is exciton diffusion limited. (Image reproduced after (43)).

The bulk heterojunction solar cell structures are similar to the bilayer mentioned above. The essential difference is that in the bulk heterojunction the active organic layer sandwiched between the electrodes is actually a blend mix of the donor and the acceptor materials.

This blend of the donor and acceptor material has a significant advantage over the bilayer planar interface in the sense that the interfacial area within the cell over which the separation of charges can occur increases. In this way even excitons with small diffusion lengths are expected to separate and ideally all of the generated excitons within they lifetime.

A prerequisite for the bulk heterojunction is that through the blend, the donor material must connect with the anode and the acceptor with the cathode, which practically is hard to control, as those are the pathways for the electrons and holes to reach the contacts. Hence a disadvantage of the bulk heterojunction structure or a factor that has to be taken into consideration is the control of the morphology of the blend.

In Figure 17 we can see the representation of a BHJ solar cell. When light is absorbed it generates an exciton (green). The exciton has to diffuse towards an active layer (a) where it can dissociate to an polaron, then split into an electron and hole that will be guided towards the electrodes. If an exciton is generated and it does not reach an active layer it is lost via recombination, while for example if an electrons wonders around in the layer it can recombine with other mobile or trapped charges (c).

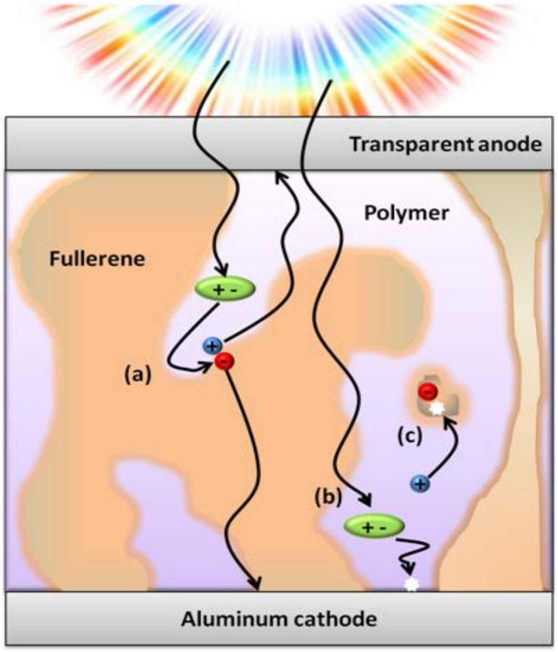

Figure 17. Bulk heterojunction organic solar cell. (a) Diffusion of the photogenerated exciton (green) and dissociation to polaron pair(red and blue), (b) Recombination of the photogenerated exciton and (c) Recombination of the generated carriers (blue) with mobile or trapped charges (red).

It can be summarized from the above that efficient dissociation of the photogenerated exciton occurs under strong electric field or at the donor-acceptor interfaces where the differences in the electron affinities and the ionization potential between the contacting materials are sufficiently large to overcome the exciton binding energy. Additionally in order to increase the exciton diffusion efficiency an interpenetrating network of the donor and acceptor material is needed, that will distribute spatially the donor-acceptor interface within the diffusion length of every exciton generation site.

## 4.5 Organic materials

The choice of donor/acceptor material in organic photovoltaics is an important merit. Candidates for photovoltaic applications include crystalline or polycrystalline films of small molecules (molecules of molecular weight of a few 100), amorphous films of small molecules prepared by vacuum deposition or solution processing, films of conjugated polymers or oligomers processed from solution, and combinations of any of these either with organic solids or with inorganic materials (46).

The first thin film organic solar cells were based on small molecules deposited by vacuum sublimation, but this single layer devices offered low efficiencies. Conjugated polymers have similar electrical properties as the small molecules, their physical properties tend to make them easier to process and they can be deposited by spin coating, yet efficiencies are low (49).

In order to increase the efficiency the tandem structures were used. Introducing a two layer device structure Tang, in 1985, deposited a layer of copper phthalicyanine (CuPc) on an indium tin oxide (ITO) coated glass substrate. On top of CuPc a second organic layer of perylene tetracarboxylic derivative (PV), both layers were deposited by vacuum evaporation and finally an opaque Ag layer was evaporated on top of the photovoltaic layer, the efficiency of the cell was no bigger than 1% (50).

The discovery of photo induced charge transfer from a conjugated polymer to fullerene-$C_{60}$ (51), followed by the introduction of the bulk heterojunction concept (52), led this material combination to be extensively studied for organic solar cell modules opening the way to higher power conversion efficiencies (5%) for organic photovoltaics (53), (5).

Fullerene-$C_{60}$ and its derivatives (Figure 18) are the most commonly used acceptor material in the organic solar cell industry and research. Fullerene-$C_{60}$ is vacuum deposited while its derivatives for example [6,6]-phenyl-C61-butyric acid methyl ester (PCBM) can be solution processed.

This acceptor material has been selected as an acceptor material for this research as it shows good electron conductivity, uniquely efficient exciton dissociation in combination with a wide range of donor materials (54), (55) and increase in solar cell efficiency (56) when compared to other materials in the same device architecture. For further insight regarding properties and applications of fullerenes the reader is advised to review (57).

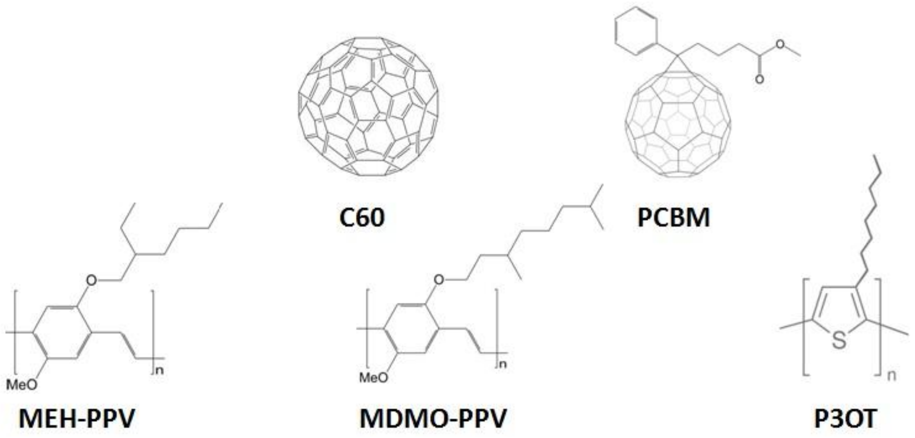

Figure 18. The structures of fullerene materials and the structures conjugated polymers commonly used in organic photovoltaics. (Image after (84))

Among many donor materials a-sexithiophene or α-6T (Figure 19), has been proven to be an attractive candidate due to its high hole mobility (58). The investigation of the properties of α-6T showed low exciton binding energy an important finding as the strong binding energy that generally characterizes the organic solar cell is considered a disadvantage (59).

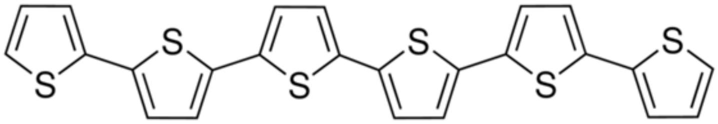

Figure 19. The molecular structure of a-sexithiophene.

In addition to the high mobility α-6T grown via evaporation shows crystalline structures, offering in this way a clearer path for the generated charges (60).

Many groups have been focusing on the development of solar cells based on oligothiophene:fullerene combination, most of them focusing on the bulk heterojunction structuring (6), (4), (61). It is referred for this bulk heterojunction solar cells that the efficiency is lower than the polymer:fullerene based bulk heterojunction solar cells due to the fact of the better blend morphology that the later present.

The goal of this research is to investigate a better controlled way over the morphology of the $\alpha$-6T:$C_{60}$ blend and combine the advantages of these donor/acceptor materials as mentioned before. To do so we wish to deposit $\alpha$-6T via vacuum evaporation on gold covered glass substrates at different substrate temperatures and monitor the different structural growth behavior that the material exhibits.

It has been shown by L. Kankate et al., in 2009 (62), that $\alpha$-6T can be grown on muscovite mica by vacuum evaporation from clusters to fiber like structures by annealing the sample holder temperature. Even though thin films of $\alpha$-6T have been grown on different materials and substrates, like silicon dioxide (63), titanium dioxide (64), gold (65), quartz, sapphire, glass (59) but concrete reports on the growth parameters and structuring of $\alpha$-6T on Au and/or implementation of this structuring for solar cell are still unknown until today.

After we have observed the growth of $\alpha$-6T on Au we wish to implement these structures to a solar cell. The final device structure that we aim to accomplish is shown in Figure 20 (a). In this type of device a glass substrate is be covered by Au, followed by the deposition via molecular beam epitaxy (MBE) in high vacuum of $\alpha$-6T, which will be covered evaporation of a layer of $C_{60}$ without interrupting the vacuum. The device will be covered by deposition of Al layer that will create the final contact.

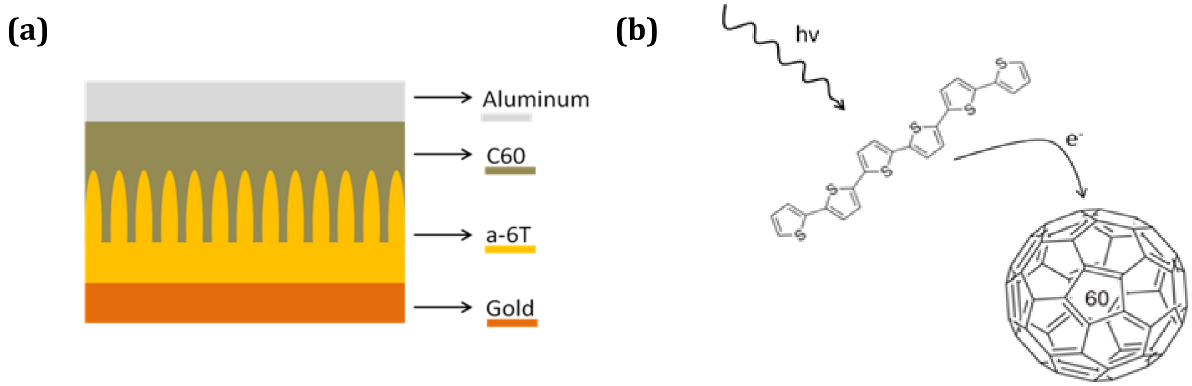

Figure 20. A sketch illustrating the cross-section of the ideal structure of the organic solar cell that is being investigated in this research in (a) and illustration of the photoinduced charge transfer in from the donor $\alpha$-6T to the acceptor C60 in (b).

# Chapter 5
# Experimental

## 5.1 Introduction

It was mentioned earlier that the first milestone of the research aims to investigate the growth of the donor material (α-6T). This will be done by organic molecular beam deposition (OMBD) of the material under controlled deposition conditions while varying the sample holder temperature.

The second milestone is to implement the findings for the fabrication of a solar cell structure incorporating the acceptor material ($C_{60}$), deposited also via OMBD. The two materials will be deposited in turns without breaking the vacuum conditions and thus avoiding any contaminants incorporating with the sample.

In this chapter the processes and steps that have been followed in this research will be described. These include sample preparation, the gold electrode deposition (anode), aluminum electrode deposition (cathode), organic material deposition (α-6T and C60) as well as the obstacles that were encountered during the research. In between there will be a brief theoretical background on the equipment that was used for the conduction of the experiments.

## 5.2 Sample preparation

The substrate that was selected for the experiments was a BK-7, 500μm thickness, double side polished, glass wafer purchased from University Wafer (www.universitywafer.com). This wafer has a very smooth surface, compared for example to glass slides, allowing the deposition of uniform thin films on it. Smooth surface is a requirement as anomalies on the substrate may result in non-flat thin film of the later deposited metal.

The glass wafers were cleaned in acetone and sonication for 20 minutes then rinsed with acetone and isopropanol, then blown dry.

The glass wafers were then diced into 25nm x 25mm squares using a dicing saw (DISCO DAD-2H/5). After dicing and prior to any material deposition the square substrates were again cleaned with the same process mentioned before.

## 5.3 Metal deposition

Thin film deposition of metallic, insulating, conductive or dielectric materials plays an important role in the manufacturing, production and research of various devices nowadays. Generally speaking thin film deposition techniques can be separated into two major categories: Physical deposition processes and chemical deposition processes.

In the chemical deposition process of thin films precursors are introduced into the chamber to react and form the thin film. This can be done either in a liquid phase where the material to be deposited is applied in a liquid/solution form (spin coating) on the substrate and then treated, for example thermally in order to crystallize the deposited film or in a gas phase where the gas precursors react with the substrate to form the thin film.

On the other hand, the physical deposition process of thin films uses mechanical, electromechanical or thermodynamic means to form the thin film. In this type of processes usually the material, such as Al, Au, Ti ect., is hit by a source (plasma, laser beam, electron beam ect.) and the material molecules travel to the surface where they are deposited forming a thin film.

All the techniques have their advantages and disadvantages, additionally not all the materials can be deposited through only one technique. For further information regarding thin film deposition techniques, properties and equipment the reader is advised to review Chapter 9 in (66).

In the present research in order to investigate the behavior of α-6T at different substrate temperatures a thin Au film (20nm) was deposited on the glass square substrates via electron beam evaporation using a Cryofox Explorer 600LT at 0.5 Å/s in order to obtain a uniform film. Later this Au layer will serve as the anode for the solar cell structures.

E-beam physical vapor deposition is one of the many techniques available for deposition of thin films. In the e-beam physical deposition process (Figure 21) a small ingot of material is placed on a water cooled hearth. Electrons emitted from a heated wire (thermionic filament) are guided as a beam with the help of magnetic fields onto the material surface. When the electron beam hits the surface the material is heated up and evaporates, the material in vapor form now arrives at the substrate where it forms a thin film. The whole assembly resides in high vacuum as well as the evaporation process takes place under high vacuum conditions ($10^{-5}$ Torr). The thickness is monitored by a quartz microbalance and the deposition rate is regulated by the beam intensity.

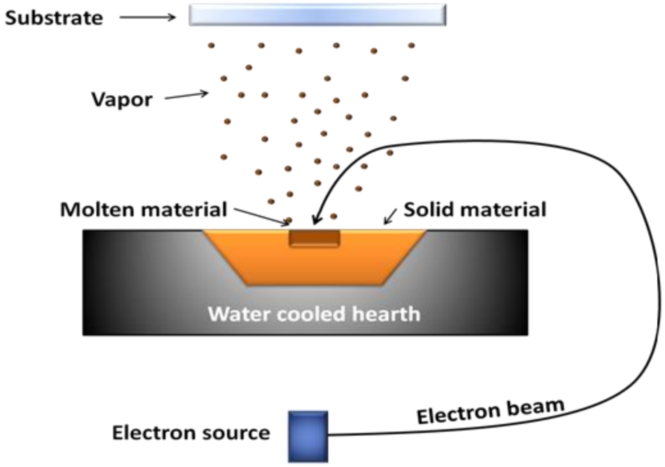

Figure 21. Illustration of an electron-beam deposition system. The electron source produces and accelerates the electrons where electric fields deflect and guide the electron beam onto the material. The point that the beam hits the material is evaporated, the vapor material travels through the vacuum onto the substrate.

In order to create the cathode in the solar cell structures 100nm of aluminum (Al) were deposited via thermal evaporation using an Edwards R500 electron beam evaporator with thermal evaporation capabilities.

Thermal evaporation (Figure 22) is one more technique that belongs to the physical deposition processes of thin films. The material usually is placed in some type of evaporation source (crucible, filaments, box sources, ect.) where it is heated under high vacuum conditions until evaporation of the material occurs. The material vapor condenses on the form of thin film on the cold substrate.

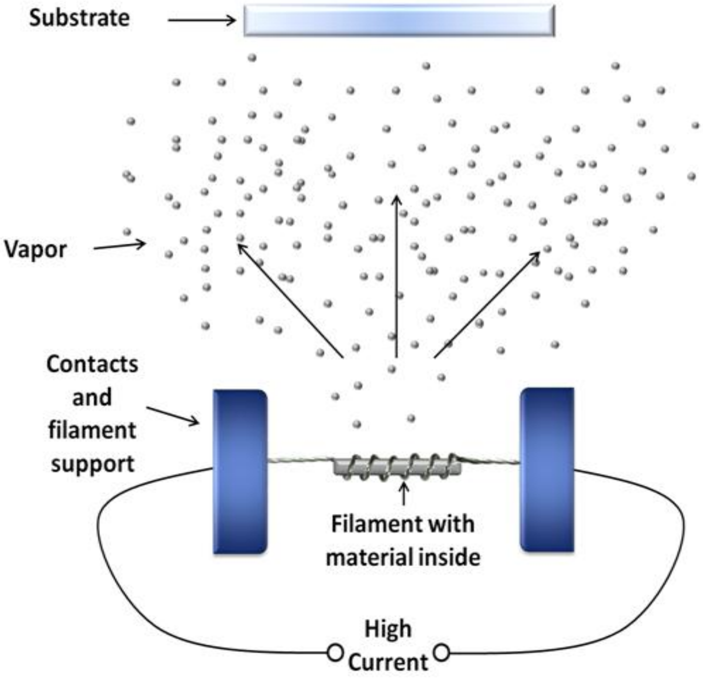

Figure 22. Illustration of the evaporation deposition process with the use of a filament. High current is applied to the filament where the material is placed, the filament is heated melting the material which in vapor form deposits on the surrounding areas as well as on the substrate.

In the present case a piece of a thin aluminum wire was used that was cut into appropriate length. The type of the aluminum wire used was 99.99% pure, with diameter of 1.00mm (www.lesker.com). The Al wire piece was placed into a filament through which high current is passing causing the filament to heat up and melt the Al wire. The filament used was an E420 type tungsten filament, 40 Amp, with diameter of 1mm and length of 50mm (www.plano-em.de). The material was deposited through homemade Al masks in order obtain four solar cell structures in a single 25mm x 25mm sample.

Due to the existing setup the thickness of the material could not be monitored by a quartz microbalance therefore a rough approximation was conducted of the desired thickness.

Since the Al deposition is done from a filament it was assumed that the deposition is done in a sphere like direction. The evaporation source, considered a point source, was placed in the middle of the sphere.

The volume of a spherical shell is given by:

$$V_S = 4\pi r^2 h \tag{3}$$

Where r is the radius from the center and h is the thickness of the shell.

The volume of a cylinder, in our case the Al wire, is given by:

$$V_C = \pi \frac{d^2}{4} L \tag{4}$$

Where d is the diameter and L is the length of the cylinder. Assuming that the target is directly above the source and neglecting any angle under which the deposition can occur we do the hypothesis that when the material with volume $V_C$ will evaporate it will form a film with volume $V_S$, hence (3) equals (4). Knowing the desired thickness (100nm), the diameter of the Al wire (1mm) and an approximate distance of the Al wire to the substrate (140mm) it was possible to derive an approximate length of Al wire of 30mm. AFM thickness measurements of the deposited Al film, shown in Figure 23, present a film thickness of 120nm which is in a close approximation with the calculations.

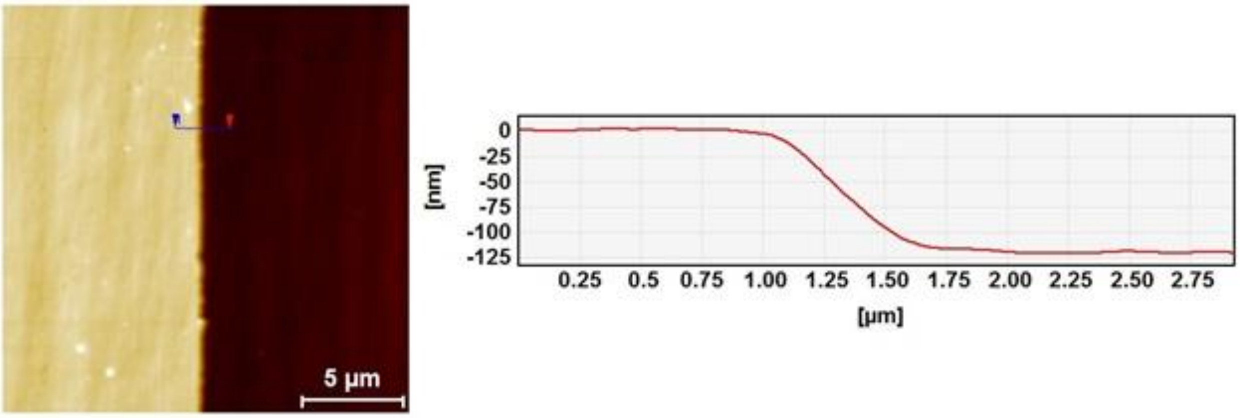

Figure 23. An AFM image with a marked line indicating the measured area. The measurement is shown in the graph with the thickness of the Al film being approximately 120nm.

It is acknowledged that this is a very rough approximation that does not take into account the angle under which the deposition can occur, as well as more parameters that can be crucial for a homogeneous deposition of a thin film. This process requires better optimization in order to achieve a better result but for these experiments a compromise has been made with the current results, as it was deducted from the AFM results that 100μm thickness can be achieved using 25mm Al wire length.

The reason why Au is deposited with electron-beam evaporation and Al is deposited with thermal evaporation lies in the fact that the organic layer can be damaged during the electron-beam deposition process. This has been discussed by Yamada et al., in 2011, where it was shown that damage to organic layers is mostly caused by the X-rays emitted from a target bombarded with accelerated electrons and in a lesser extent by electrons reflected at the surface (67).

## 5.4 Organic material deposition

Non soluble organic materials are being deposited mainly with the use of organic molecular beam deposition (OMBD) technique, which is one more form of physical deposition process. The deposition takes place usually under high or ultrahigh vacuum conditions.

The material in the form of powder is placed inside an effusion cell, also known as Knudsen cell, where it is heated above its sublimation temperature and evaporated onto the substrate. Typically a Knudsen cell is a small crucible with a cap on top of it, heated by resistive heating (i.e. thermocoax cables). The cap on the crucible has a small hole diameter from which the molecules escape with a very small and controlled rate, this is done by controlling the heat delivered to the cell. For convenience the crucible/cap assembly will be referred to as oven.

The deposition rate has range typically from 0.001 to 100 Å/s and it is monitored by a quartz microbalance crystal placed in close proximity to the substrate. The entire setup in enclosed in a chamber in order to allow fast vacuum pumping.

When appropriate vacuum conditions are met ($10^{-7}$ - $10^{-9}$ Torr) and the material has reached appropriate deposition temperatures the produced molecular beam that is ejected from the crucible arrives onto the substrate and a layer starts to form.

Crystal and thin film growth can follow one of the classical growth modes, i.e. Frank-van-der-Merwe (FV) which is a layer-by-layer processes where a new layer is nucleated only after completion of the layer below, Vollmer-weber (VW) where island growth starts from the first monolayer, and the Stranski-Krastonov (SK) growth mode which lies in between of the two mentioned before. In the SK mode the first layer is atomically smooth (FV) until a certain thickness known as critical thickness, when this thickness is reached phase transition to islands takes place (68), (69).

Growth of organic films via OMBD is dependent on many paragons. The type of substrate can influence the orientation of the film as the interactions of molecule-molecule or molecule-substrate at surfaces can be different. The deposition conditions such as substrate temperature, deposition rate influence strongly the growth kinetics.

For example it has been shown by Kankate et al., in 2008, that para-hexaphenylene (p-6P) organic material can grow from clusters to fiber like structures on muscovite mica by tuning deposition conditions such as the substrates temperature and/or the materials thickness. It is mentioned there that deposition of p-6P on mica at low temperatures the surface is covered by a uniform film while by increasing the temperature fiber growth starts. The clusters follow a SK type growth mode and fibers are formed by agglomeration. This is dependent on the thickness of the material and the temperature, as for a thickness of 0.2nm clusters are distributed over the mica surface even at elevated temperatures (337K to 438K), while for a thickness of 0.7nm the clusters at low temperatures (337K) start to form fiber structures with increase of the substrates temperature (70).

A similar behavior and kinetic dependence has been reported for growth of α-6T fibers on mica by Bazler F., Chapter 3 in (9) and by Kankate et al. in (62). Deposition of α-6T on mica substrate via OMBD at room temperature results in closely packed small fibers and by increasing the substrates temperature the number density of the fibers decreases while their length increases. Hence it can be deducted that α-6T shows a similar growth behavior to p-6P following the SK growth model composed of three steps: (1) the incident molecules form a wetting layer, (2) the nucleation and growth of clusters up to a critical number density or up to a critical cluster size, and (3) the assembly of structures from single clusters.

Moreover deposition on different substrates leads to different behavior of the material, due to different surface energies and mobility of the molecules. For instance the deposition of p-6P on mica results in the growth of mutually parallel nanofibers with directions dependent on the crystalline directions of the substrate, while p-6P on thick Au surfaces (approximately 20nm) leads to randomly oriented nanofibers forming a mesh-like structure (10), hence structuring of the surface is implemented in order to manipulate the growth direction (71).

Deposition of α-6T on mica leads to the formation of needle like structures that follow three preferred orientations, while the strong fluorescence of the structures indicates molecules lying on the surface (62). In addition to that it has been demonstrated that α-6T deposited on Au has its molecules lying on the surface [ (72) and references within], where in comparison to α-6T on oxides the molecules tend to stand perpendicular to the surface (64).

For more information related to crystal growth, OMBD and the relative processes and steps the reader can review (9), (73).

### 5.4.1 The OMBD setup

In order to conduct the experiments a preexisting OMBD setup was used, shown in (Figure 24). The ovens within the chamber were connected with the external environment using feedthroughs (1), each oven had two external connections one was for supplying power to the oven and one for measuring the temperature of the oven using a K-type thermocouple. The oven area (2) is where the homemade ovens within the chamber reside in approximate distance of 150mm from the sample holder. Typical oven-sample holder distance for commercial ovens is approximately 100-150 mm.

Additional feedtroughs (3) provided the necessary connections for heating the sample holder and measuring its temperature, as well as operating the shutter (open/close).This is also the part of the chamber that could be opened in order to load the sample inside the chamber. The main chamber area (4) is where the sample holder and the quartz microbalance crystal reside. The water cooled quartz microbalance is used in order to monitor the deposition rate and the thickness of the deposited material. One last feedthrough (5) provided the external connections of the crystal to the thickness monitor.

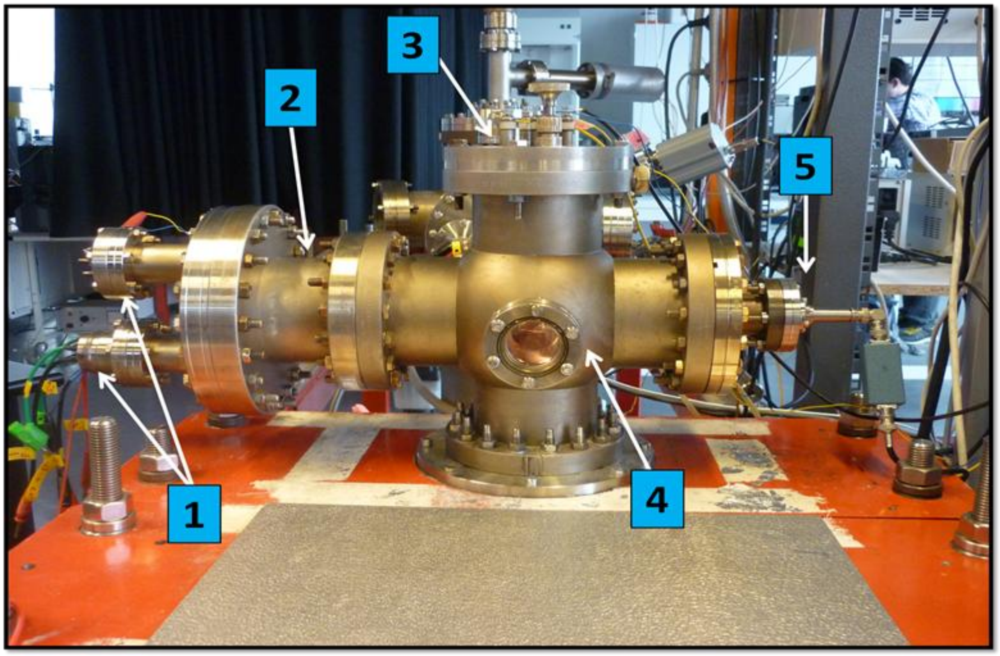

Figure 24. OMBD setup used for the conduction of the experiments. (1) Feedthroughs to supply power to the thermocoax in order to heat the ovens and to measure the temperature at the ovens, (2) Area where the ovens exist within the chamber, (3) Feedthroughs to supply power to the thermocoax of the sample holder in order to load in the sample, heat the sample holder, to measure the temperature of the holder and to open/close the shutter, (4) Main chamber area where the sample holder, shutter and the quartz crystal reside and (5) Feedthrough for the connection of the microbalance with the thickness monitor.

Supply to each of the ovens was provided by a Delta Elekrtonika ES 075-2 power supply by controlling the current (www.delta-elektronika.nl), while the supply to the sample holder was provided by a Maxireg 761 power supply. The temperature of the sample holder was set on and automatically regulated by an Altec AL808e digital temperature controller (www.altec.cc). The temperature was typically measured with multimeters. The deposition rate and thickness of the deposited material were monitored with a Maxtec Inc. TM-350 thickness monitor (www.pascaltechnologies.com).

The oven temperatures as well as the deposition rate and thickness were also being monitored by a Labview program provided by PhD student Michal Radziwon in order to hold an archive with all the deposition conditions. Appropriate vacuum conditions were achieved using an Edwards 12 rotary vane pump for primary vacuum pumping (www.edwardsvacuum.com) and a Pfeiffer TMU 261 turbo pump (www.pfeiffer-balzers.com) for higher vacuum pumping. The vacuum was measured using an ion gauge and it was monitored using a Varian Multi-Gauge controller. The whole assembly with the appropriate connections to the equipment is illustrated in Appendix 2.

An inside look of the OMBD setup (Figure 25) will give a better understanding of the processes that take place in order to deposit organic material on a sample. An oven (1) is filled with the desired organic material. The oven is winded with a thermocoax cable in order to provide resistive heating. Resistive heating is the effect when electric current flows through a conductive material that has some resistance it creates heat (74). Therefore current supply to the thermocoax leads to heat of the wire which in turn heats the oven, thermocoax resistance in the range 20-24 Ω supplied sufficient heat.

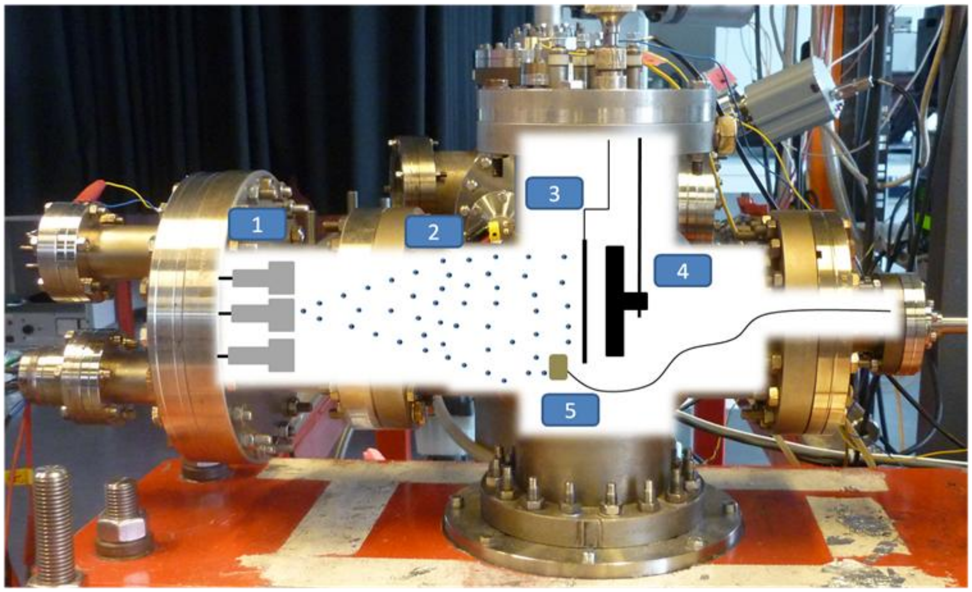

Figure 25. Representation of the internal parts of the OMBD setup. The material is placed in the ovens (1), heating the ovens to the temperature at which the material turns into gas lets the material to escape from a small orifice at the oven which in gas form now (2) moves towards the substrate. A shutter (3) placed in front of the substrate (4) blocks the beam until desired deposition rate is reached. Deposition rate and thickness are monitored by the crystal (5) placed below the substrate.

Due to high vacuum conditions the material transition phase is from solid to vapour without the intermediate liquid phase.

It should be noted that the vapour phase of each material is different therefore the proper oven temperature has to be determined experimentally by slowly heating the oven until deposition rate is evident at the deposition monitor.

The material particles (2) travel under high vacuum towards the substrate. In general molecular flow is achieved under high or ultrahigh vacuum conditions, because in this regimes molecules flow without any interference. Molecular flow is present where the mean free path of the particle is very much larger than the diameter of the pipe (75).

A shutter (3) that can be operated externally blocks the material flow to reach the substrate, in this way the deposition of material on the sample can start only when the shutter is open. The sample is placed on the sample holder (4). When the shutter is open material deposition on the sample starts.

The deposition rate and the thickness of the material are being monitored with the use of the water cooled crystal that is placed below the sample holder (5).

The initial OMBD setup contained two ovens one for deposition of α-6T and one for deposition of $C_{60}$. During the conduction of the first experiments, investigation of the morphology of α-6T on Au glass covered samples, some irregularities occurred. For unknown reason the system was short circuit leading to faulty deposition conditions. In order to repair this issue new ovens with new connections were installed, adding supplementary a third oven.

The final oven setup is illustrated in Figure 26 (a). The ovens were screwed onto a rod together with a plate that was designed (Appendix 3) in order to attach the connections of the thermocoax in a stable manner.

Through the inside of the rod a hole was created to pass the thermocouple that would measure the temperature of the oven. This gave a more accurate measurement of the oven temperature as it was in direct contact with the oven compared to previously where the thermocouple was attached on the thermocoax. The third oven was used for the deposition of bathocuproine (BCP) that would serve as a buffer layer between $C_{60}$ and Al as it will be discussed later.

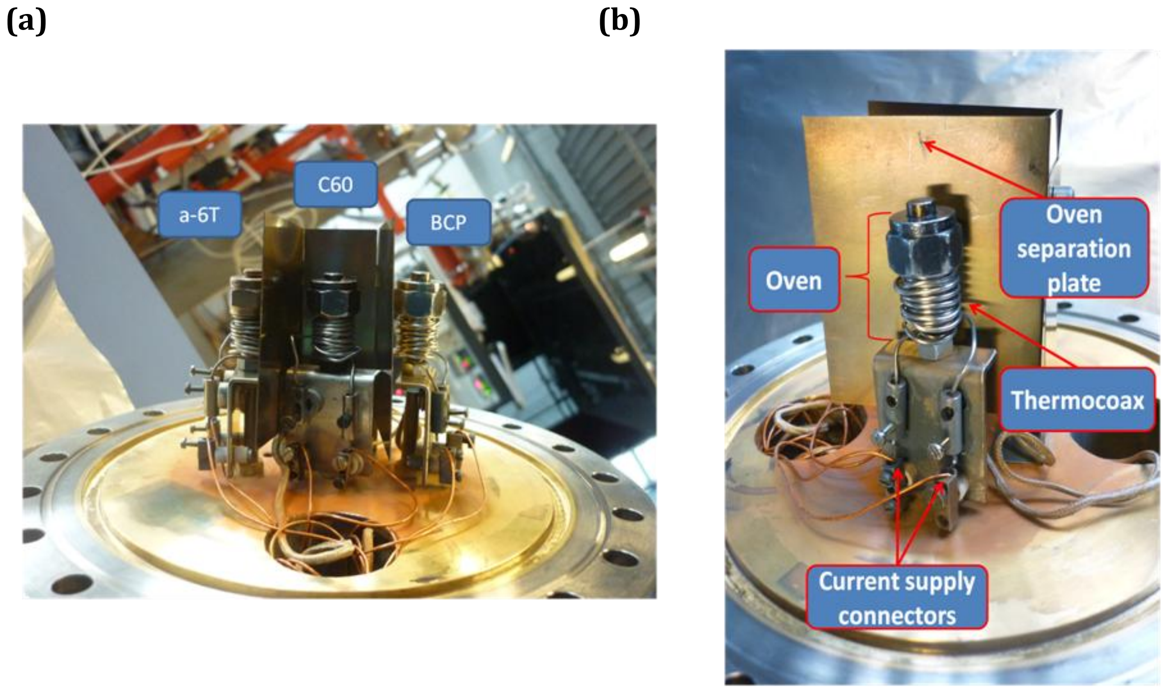

Figure 26. New oven setup for the OMBD system. In (a) the three new ovens for deposition of α-6T, C60 and BCP materials and in (b) a closer look of one oven explaining the main parts, the thermocoax is wrapped around the main body of the oven while a cap on top, with a small diameter hole, allows easy access to fill the oven.

A separation plate was placed between the ovens, in this way when one material was evaporated the beam would not deposit on the nearby oven avoiding thus cross contamination of the ovens.

Even though the experiments were able to continue with the new setup, some minor problems, design related, were accompanying it. Because of the limitation of space in the chamber and the ovens being relatively squeezed in a small area the screws on the connectors were in touch with the main body of the chamber causing short circuit and thus obtaining peculiar deposition rates.

Another problem that was resolved was that the deposition rate was rather small with this setup. This was due to the fact the distance between the ovens and the sample holder was big and the deposition of the material was ending before it reached the substrate.

This problem was related to the new ovens as Knudsen cell design related issues were not taken into consideration. Solution to this came by removing a part of the chamber, hence reducing the distance oven/sample. This is the distance we mentioned earlier (150mm).

Figure 27 proves the earlier said, that the material was not reaching the sample holder and the deposition was ending right before the microbalance.

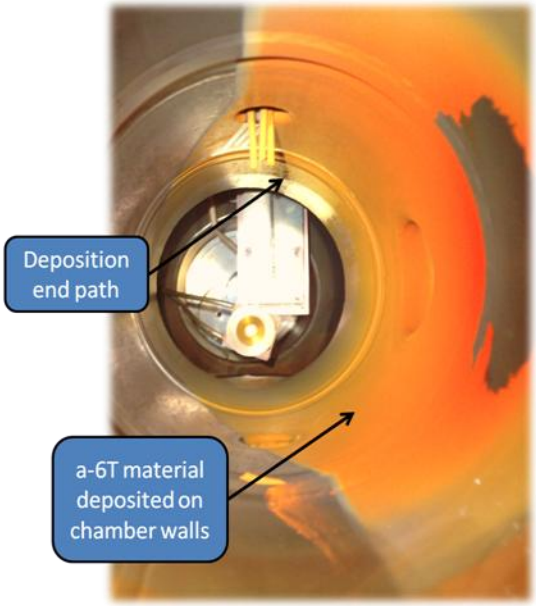

Figure 27. The inside of the OMBD chamber, a view from the oven part side. It is evident that the material mainly deposits on the walls of the chamber and it stops before it reaches the sample holder, denoted on the image as the deposition end path.

One important key feature in the research is the sample holder temperature. The temperature must be evenly distributed all over the sample holder in order to heat in a homogeneous way the sample that is placed on it. The temperature distribution is crucial as it affects the growth of the material on the sample.

The sample holder in the OMBD setup consisted of two copper plates sandwiched together with the thermocoax placed in the middle, bent in a zigzag manner. Current supply to the thermocoax would produce heat which would be distributed through the copper plate to the sample.

Figure 28 illustrates the sample holder assembly. The problem here was that due to the design of the sample holder the temperature was not homogeneously distributed over the top plate. This was because the thermocoax between the top plate and the bottom plate was not in absolute contact with the plates in all its areas.

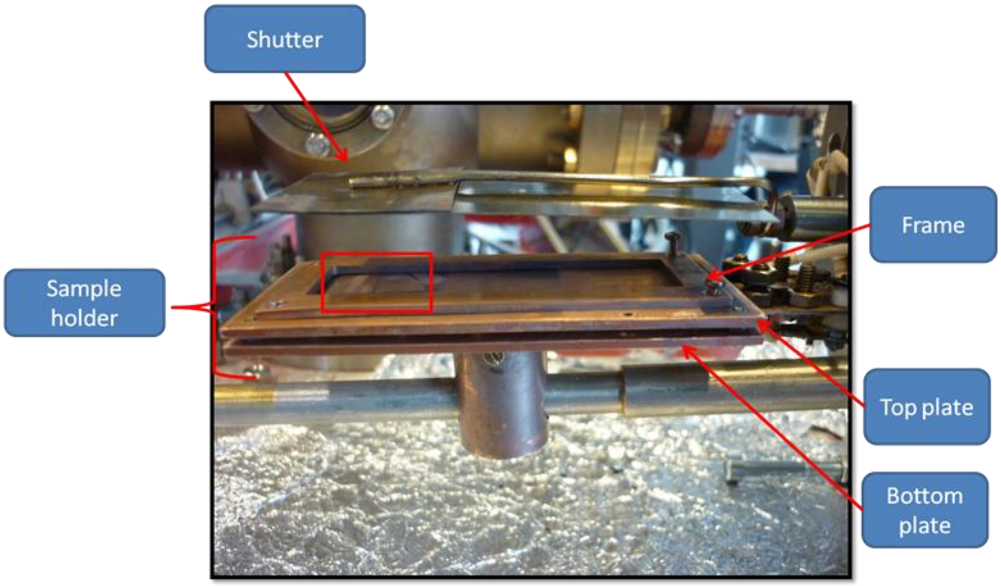

Figure 28. Image of the sample holder in the OMBD setup. The shutter is used to block the undesired beam hitting the sample holder right below it. The red square in the image designates the area that the samples were placed and attached by the frame. The thermocoax is placed between the top plate and the bottom plate.

Additionally the copper plate due to its thermal expansion coefficient and small thickness was bending after extensive use, an extra factor lowering the homogenous temperature distribution. Therefore every time that this bending phenomena was observed the plates should be straighten and cleaned with acetone in order to maintain contamination in minimum.

Even though these obstacles were kept in minimum and some eliminated, temperature distribution remains an issue for inserting more than one sample for deposition and future improvements on the design of the sample holder should be kept in mind.

In order to avoid errors in the measurements of the experiments due to errors in thermal distribution the samples at all cases were placed at the area denoted with a red square in Figure 28, as the thermocoax that measured the sample holders temperature was placed below that point. It should be noted that before every material deposition the sample holder was heated for minimum one hour, this would assure that the desired temperature would be distributed evenly over the sample.

A process recipe describing the parameters and the processes that were followed for sample preparation, the deposition of the metal electrodes, organic material depositions can be found in Appendix 4.

# Chapter 6
# Results and Discussion

## 6.1 Process sequence

Once the glass samples were prepared and the 20nm Au layer had been deposited, the samples were directly placed in the OMBD chamber in order to deposit α-6T material. It is worth to mention that the samples were prepared every time right before deposition of the organic material in order to avoid any contaminants on the samples. It was observed that for Au covered samples left for day's contaminants were residing on the sample and this could affect the deposition and the growth of the material.

Each of the samples was characterized with fluorescence microscopy using a epifluorescence Nikon Eclipse ME600 ($\lambda_{exc}$=365nm) in order to obtain fluorescent images, while using the same setup with the attached Optics Fibre-Spectrometer the emission spectra of the samples was observed. Details on the structures were observed with atomic force microscopy (AFM) using a Veeco Dimension 3100.

In order to conduct each experiment the temperature, at which the α-6T material would start to deposit at a stable deposition rate, had to be determined. This may be different from setup to setup as the ovens and the way the ovens are heated may differ. For this study it was found that for a steady deposition rate of 0.1 Å/s the oven temperature should be 310˚C for α-6T, 350˚C for $C_{60}$ and 240˚C for BCP. Increasing the supply to the oven, leads to an increase of the ovens temperature, this in turn leads to increase in the deposition rate.

Prior to deposition each material was outgassed, which is a necessary process in order to purify the material. Purification is done by heating the oven in lower temperatures than the deposition temperature of the material. Contaminants within the material tend to evaporate at lower temperatures than the material and they can be pumped out of the chamber. If the material is not purified then the material deposited on the surface can either be fully contaminated resulting in abnormal structures or create defects on the sample.

After purification of α-6T at least one sample was prepared in order to inspect the samples for contaminants if the sample was clear the experiments could continue further otherwise the material had to be outgassed again.

Within the chamber without application of any external heating the temperature was approximately 30˚C, this will be denoted as the room temperature throughout the report. The first deposition of α-6T was done at this temperature. We would like to define here that the term "cluster" will be used for small structures that have random dimensions while the term "fiber" will be used for better defined long structures.

In the following data analysis from the AFM scans for samples made from room temperature to 100˚C small scanned areas will be used in order to reveal the features of the structures such as height distribution and roughness, while for bigger structures, growth temperature above 100˚C, larger scanned areas are required.

## 6.2 Growth of α-6T on Au

Figure 29 (a) shows the fluorescent microscopy image of α-6T deposited at substrate temperature $T_S$=30˚C, the black spots on the image are defects from the microscope are should not be taken into consideration. It seems from the fluorescence images that a film of α-6T is formed on the sample, but the AFM shows us otherwise, Figure 29 (b).

It was observed that cluster like structures with different dimensions are present on the sample. For this rather low temperature it was expected that the material would form a thin film instead of cluster structures.

The average height of the structures was 29.1nm, with a maximum of 86.19nm, while the root-mean-square roughness was 12.3nm denoting that these densely packed clusters form a rather rough surface. From the height distribution graph in Figure 29 (c) we can observe that there are two peaks which were fitted with two Gaussians.

The first fit has the center at 13.89nm ±0.124nm and the second has the center at 30.17 ±0.247nm. It is assumed that this is due to the fact that there can be two different cluster structures, for example small circular clusters indicated with the first fit while longer and bigger clusters can be indicated with the second fit.

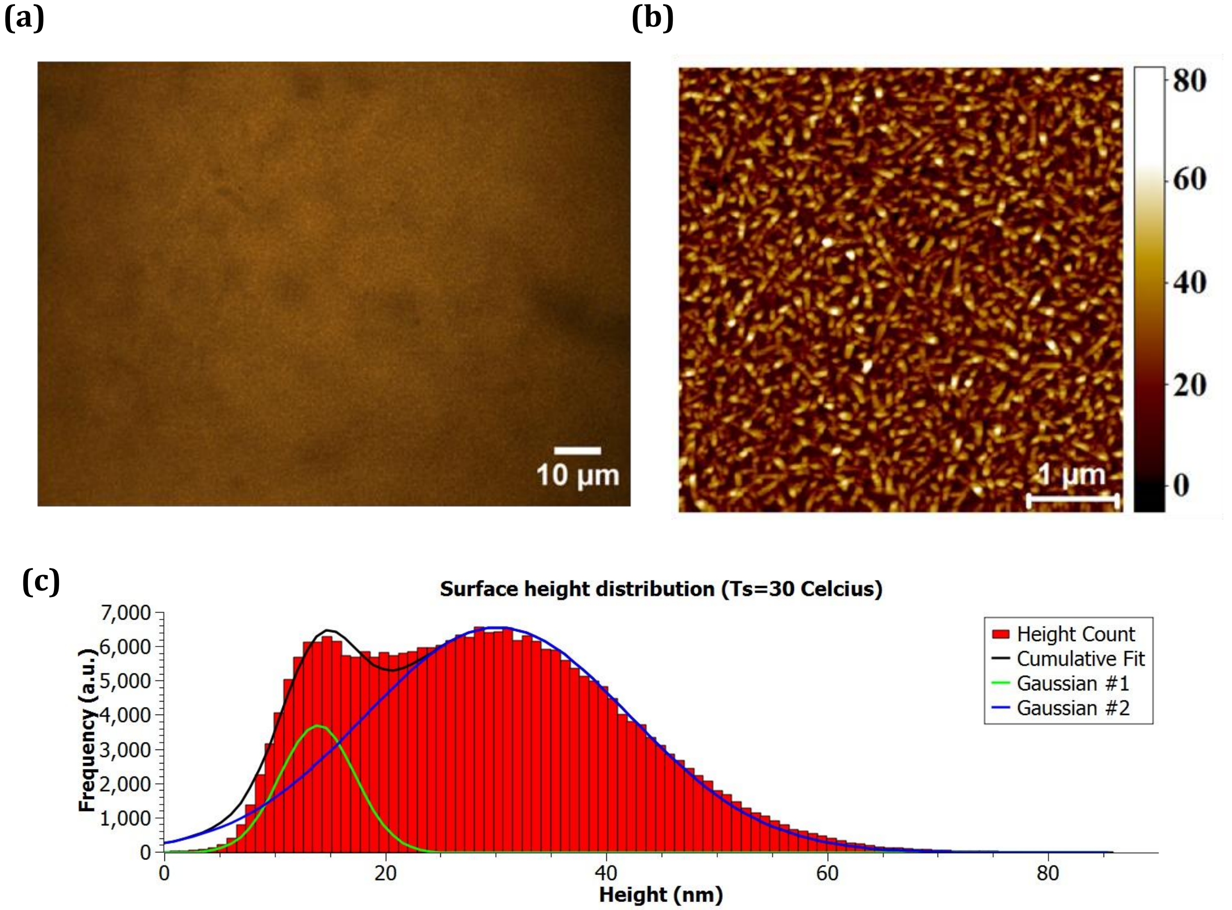

Figure 29. (a) Fluorescent microscopy image from a sample created room temperature, (b) 5µm x 5µm AFM scan of the sample showing the cluster like structures on the sample with the equivalent height scale on the right side and (c) Cluster height distribution from a 5µm x 5µm scanned area on the sample.

From the analysis of the samples at this temperature it can be considered that the α-6T material might not cover the whole Au covered sample leaving behind some holes. This can be troubling for solar cell structures as it leaves a window for the overlayers to contact the anode.

Fluorescence images of α-6T at $T_S$=50˚C, Figure 30(a), show no evident differences from the fluorescence images at $T_S$=30˚C. The AFM scan of an 5μm x 5μm area on the sample at $T_S$=50˚C shows the presence cluster structures on the surface, Figure 30 (b).

By looking at the height distribution graph Figure 30 (c) it can be seen that again there can be present clusters with two different structures. The difference in this case is that the first peak is smaller compared to the second one (from left to right). It can be assumed from this that the clusters tend to obtain more defined structures. By a very rough approximation it was found that within a 2μm X 2μm area 284 clusters are present.

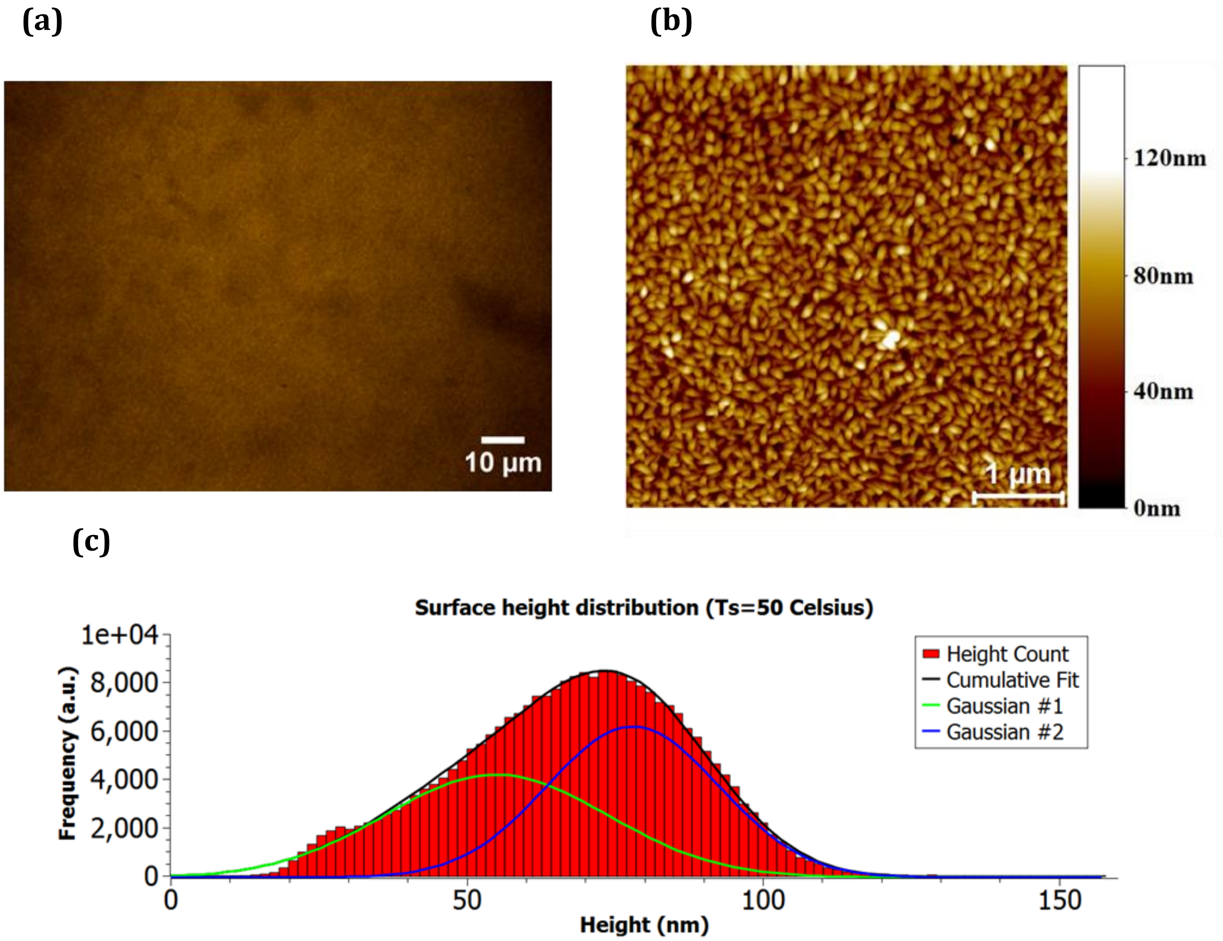

Figure 30. (a) Fluorescent microscopy image from a sample created 50˚C, (b) 5μm x 5μm AFM scan of the sample showing the cluster like structures on the sample with the equivalent height scale on the right side and (c) Cluster height distribution for a 5μm x 5μm sample, with a Gaussian fit indicating most probable height of 69.42nm ±0.28nm.

Surface roughness measurements of the sample gave a root-mean-square roughness of 19.24nm, with maximum cluster height of 158nm and an average cluster height of 68nm. The fiber width has an approximate average value of 0.30nm. From the height distribution in Figure 30 (c) the first Gaussian fit has center at 55nm ±6.045nm, while the second Gaussian has center at 78.1nm ±1.52nm.

For deposition of α-6T at substrate temperature of 100˚C, the α-6T molecules seem to diffuse on the surface to form fiber like structures with different lengths as seen in the fluorescence image in Figure 31 (a), while clusters structures are still present on the surface (Figure 31 (b)). The root-mean-square roughness of the surface was 70nm, the fibers had average height of 144nm with maximum ≈339nm, while the length is in the range of a few microns (≤2μm).

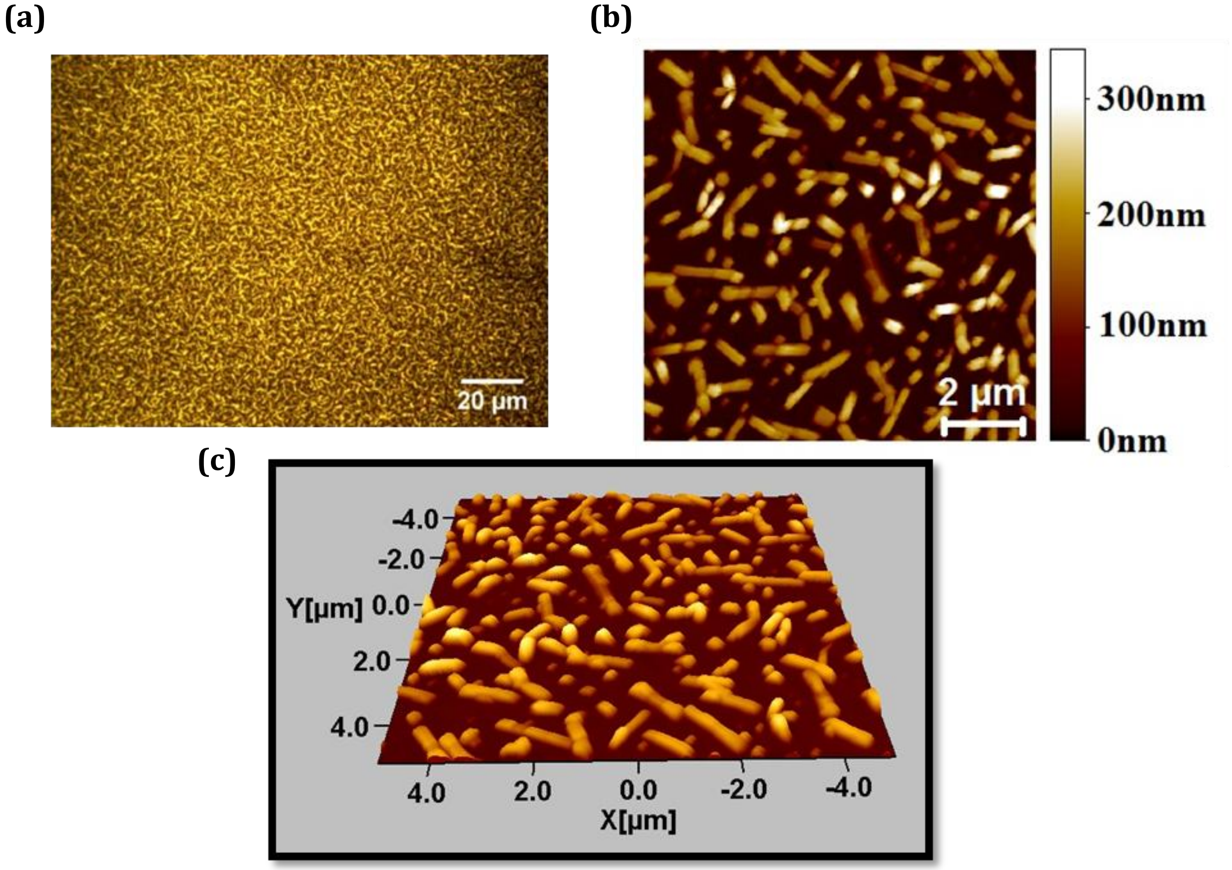

Figure 31. Analysis of a sample made at 100˚C substrate temperature. (a) Fluorescent microscopy image showing small length fibers, (b) AFM scan of a 10μm x 10μm area of the sample and the 3D view of it (c).

An interesting observation for the samples made at $T_S$=100˚C is the way the fibers are formed. It seems while scanning with the AFM tip that a double tip phenomena is present. Scanning other samples at the same temperature as well as scanning a reference sample with predefined structures and sizes it was concluded that this is the way that the fibers grow at that temperature.

It can be seen in Figure 32 (a) and (b), that when the fiber is formed is accompanied with additional hill like structures on the side, the graph in (c) shows the cross section of a fiber, marked with the blue line in (a). The width of this fiber at that point was ≈300nm which differs from fiber to fiber as well as across the length of the fiber structure.

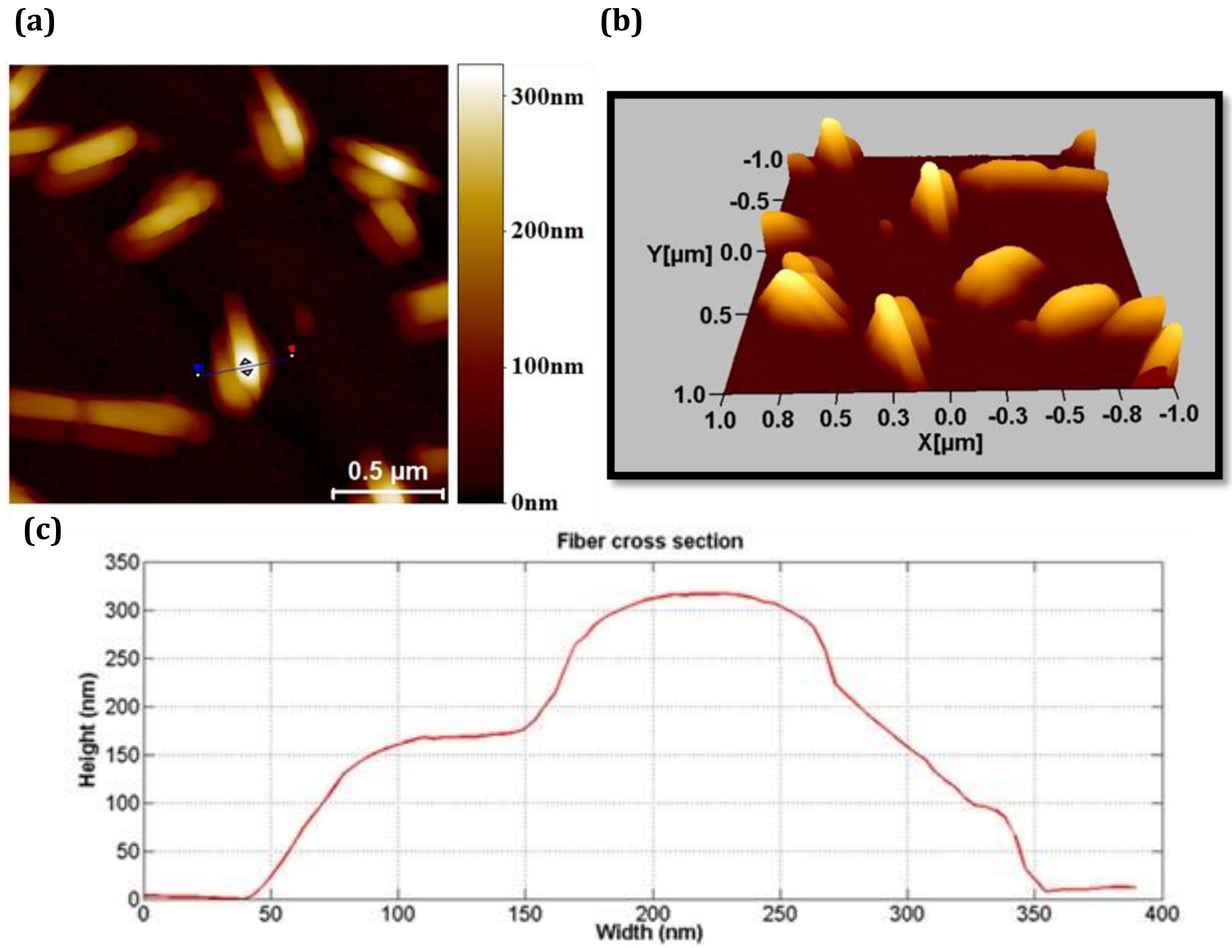

Figure 32. AFM scan of a 2µm X 2µm area of a sample made at $T_S$=100˚C in (a), the equivalent 3D view of (a) showing the hills on the side of the fiber and in (c) the cross section of a fiber, denoted with a line in (a), width=300nm, height=320nm.

The fluorescence and AFM image, in Figure 33 (a) and (b) accordingly, for α-6T samples deposited at substrate temperature $T_S$=150˚C show well formed fibers in comparison to the previous lower temperatures. The fibers have a well defined structure without any additional hill structures on the sides, while it can be seen that the fibers are accompanied by additional fibers attached like branches, some are indicated with red circles in Figure 33 (a) and (b). This growth effect of the fibers makes it difficult to determine exact fiber length. The average length of the fibers is 2.78μm with a maximum close to 7.64μm. The length measurements have been done by measuring also the branches of the fibers as individual fibers. The length measurements should be taken as an approximation aas the fibers do not grow straight but they form angles along the fiber length instead..

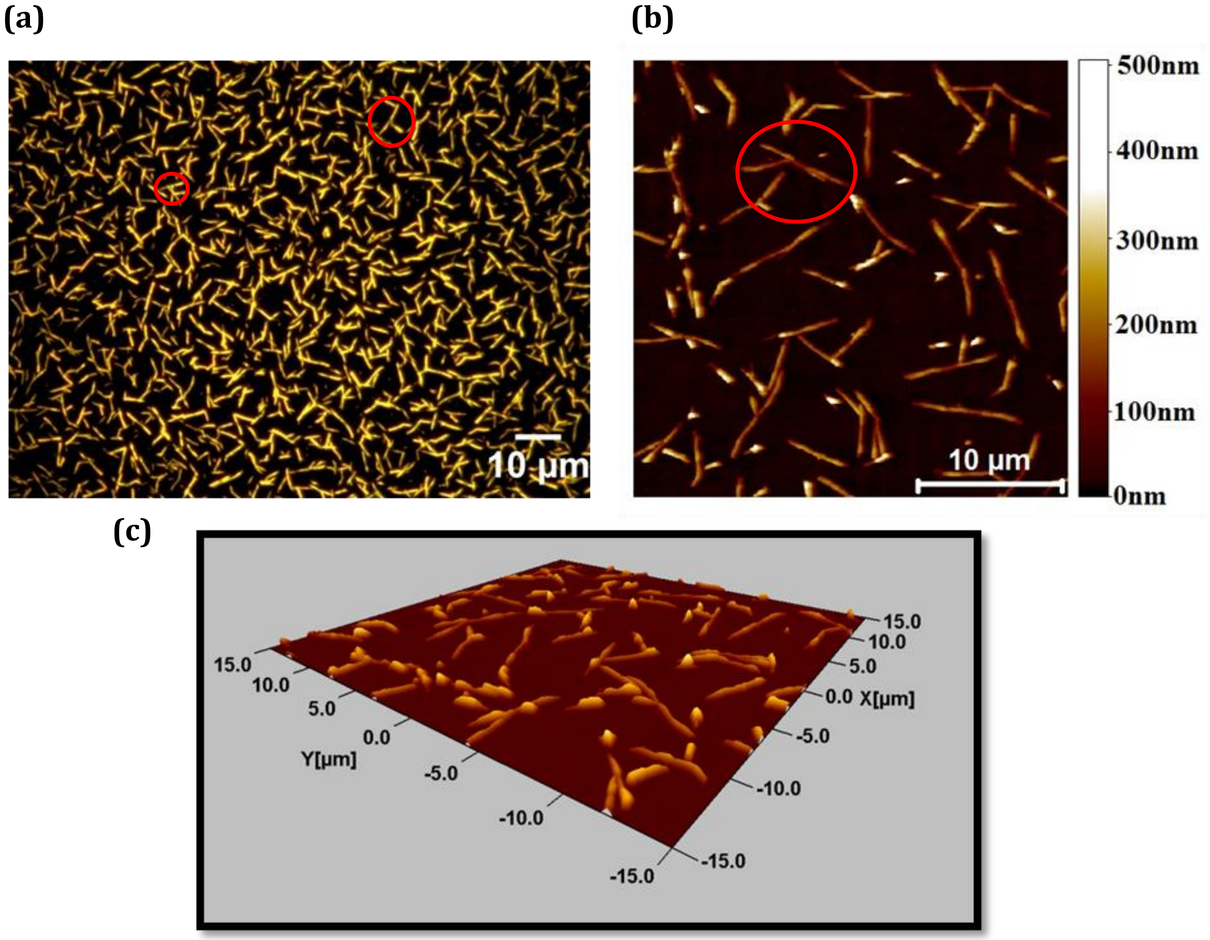

Figure 33. Fluorescence microscopy image of α-6T sample on Au at $T_S$=150˚C in (a), 30μm x 30μm AFM scan of the same sample with the height scale bar on the side in (b) and a 3D representation of the AFM scan showing the "mountain" structure of the fibers in (c).

The average height of the fibers was 123nm with a maximum value of 505nm, while the average width of the fibers was 0.40μm. It seems that the fibers do not form completely flat structures with definite height and width but with some type of a mountain like form with hills and valleys along fiber length. This is similar to the case of p-6P nanofibers grown on Au shown in (10). There the surface roughness and the interface energy influence the growth of the organic nanoaggregates. It was demonstrated there that for thin Au layers the nanofibers grown are either flat or rounded, whereas for thick Au layer (>8nm) facets along the long needle axis appear.

By increasing further the substrates temperature longer fibers appear. At $T_S$=170˚C, the α-6T fibers have an average height of 275.2nm and average width of 1μm. The fibers as it can be seen in Figure 34, fluorescence microscope image in (a) and 30μm x 30μm AFM scanned area in (b), form long curved structures accompanied again from branches.

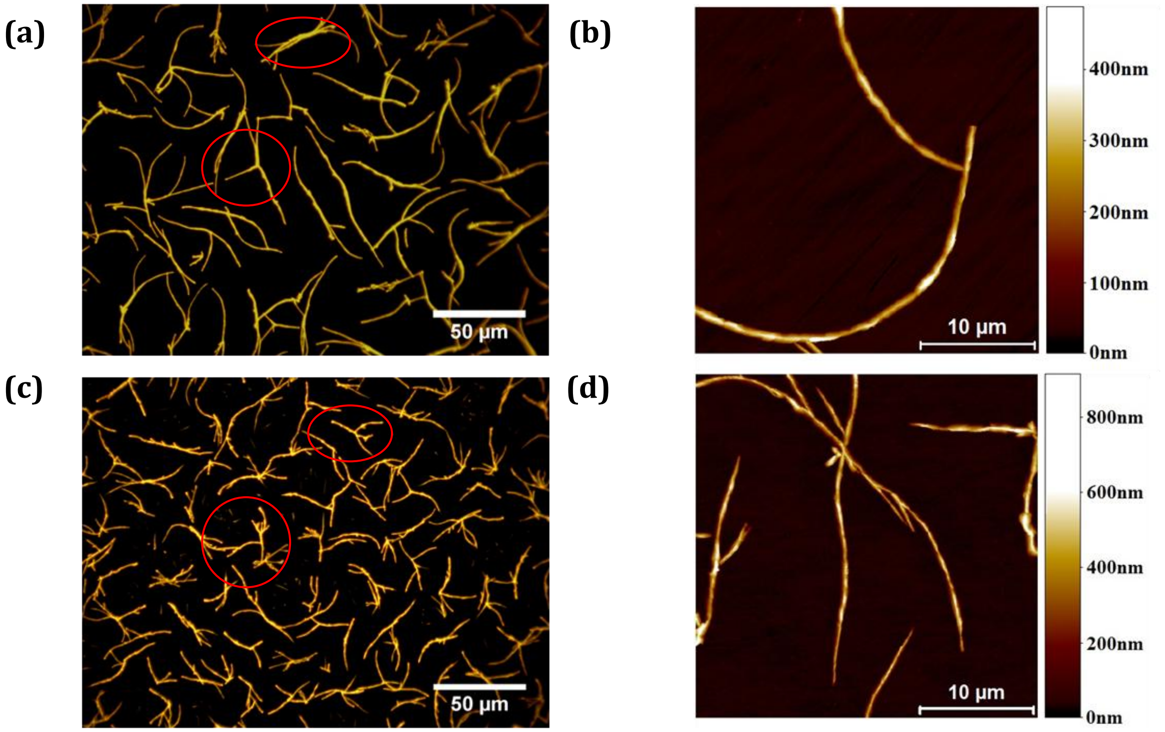

Figure 34. (a) Fluorescent microscopy image of α-6T on Au at 170˚C showing random growth of long fibers accompanied with branched fibers and (b) an AFM scan of the same sample showing a part of a long fiber with a branched fiber attached to it. At 175˚C long fibers are accompanied by smaller branched fibers in different areas shown in the fluorescent microscopy image (c) and the AFM scan shows that the height of the structures increases but the width decreases compared to the previous temperature (d).

In this case due to the structure of the fibers is harder to define fiber length. If we look at the red circled areas it is not clear if the branches that are formed overlap the longer fibers and they continue to grow forming branches or if they start to form from the "crossroad" that they are observed to form branches.

These long fibers continue to grow further as the temperature is increased to 175˚C. The difference at this temperature is that branches with smaller fibers attached exist among the long fibers (see red circled areas in Figure 34 (c)) giving the feeling that the long fibers brake, this can be observed in Figure 34 (c) where long fibers are accompanied with smaller fibers forming branches in different places. In this case the structures were higher than in the previous temperature, average height 440.6nm, while the thickness, measured from the AFM scan, of the structures was reduced, average width 0.36μm.

Further increase in temperature, $T_S$=180˚C, did not give rise to any fibers, hence it can be stated the fiber growth stops for substrate temperature range 175˚C-180˚C. This type of growth behavior where growth stops above a certain temperature has been observed for p-6P on mica where the fiber growth stops at 207˚C (70) and similar case is for p-6P on Au surface (76).

The above data for α-6T growth at different substrate temperatures are summarized in Table 2.

Table 2. Growth parameters of α-6T at different substrate temperatures.

| Substrate Temperature | RMS Roughness | Average height | Average Length | Average Width |
|---|---|---|---|---|
| **30˚C** | 12.3nm | 29.1nm | N/A | N/A |
| **50˚C** | 19.2nm | 68nm | N/A | N/A |
| **100˚C** | 70nm | 144nm | ≤2μm (aprox.) | 0.3μm |
| **150˚C** | 55nm | 123nm | 2.78μm | 0.40μm |
| **170˚C** | N/A | 275.2nm | N/A | 1μm |
| **175˚C** | N/A | 440.6nm | N/A | 0.36μm |

It is worth to point here the importance of temperature homogeneity over the whole sample. It was shown in a previous chapter that the sample is placed on the sample holder on a specific area, while all the measurements are conducted by looking in the center of the square sample. At $T_S$=180˚C while moving away from the center of the sample, as shown in Figure 35, structures start to appear. The hot center of the substrate is denoted with the red dot in the sketch and the arrow points the direction towards the cold edge of the sample, accordingly the same direction is followed for the fluorescence images looking for left to right. The dark area on the left denotes the hot surface, while moving away from the center towards the colder edge α-6T structures appear.

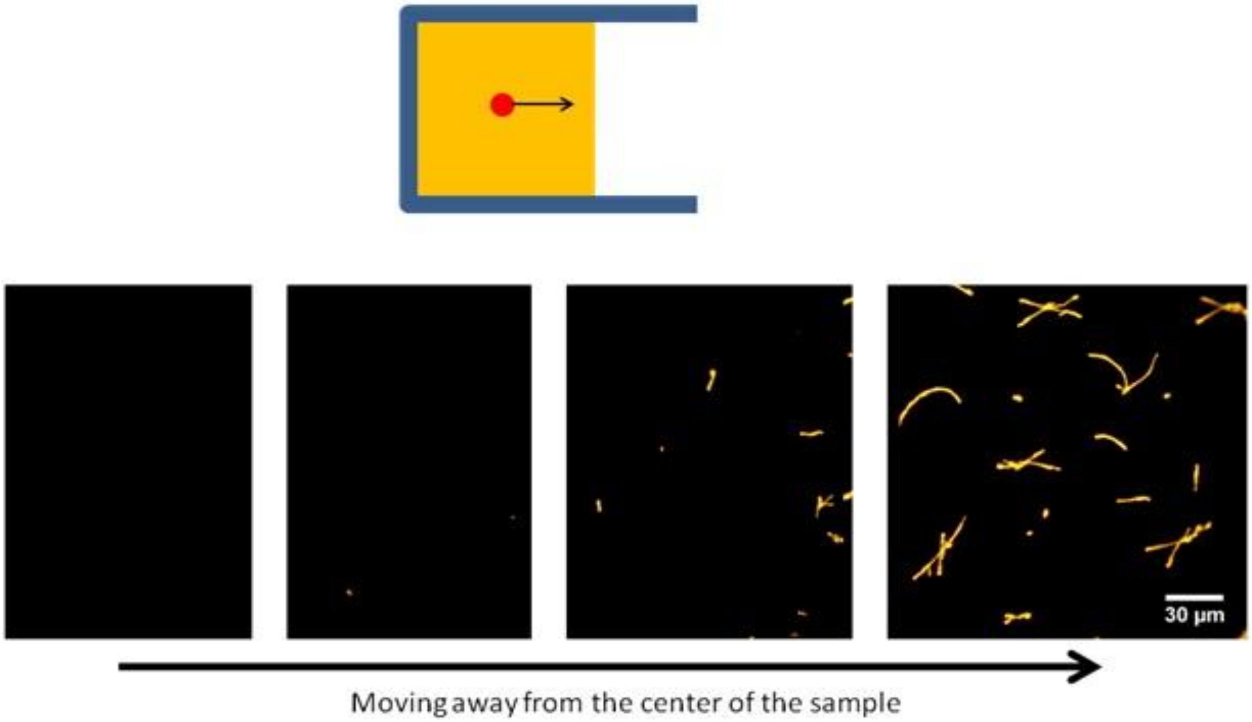

Figure 35. The sketch on the top shows the 25μm x 25μm sample (yellow) under the frame (blue) and the center that is used for the measurements. The arrows indicate the direction at which the above fluorescence images were obtained.

The inhomogeneous temperature distribution over the sample area can be accounted for this effect. This proves also the fact that designing a sample holder must assure that the temperature is distributed the same over the whole sample holder area in order to be able to obtain more samples at the same time instead of only one as it was in this case.

In Figure 36 two fluorescence images are shown, of α-6T material deposited on Au that was not purified properly. In (a) an interesting feature can be observed, the α-6T material deposited at room temperature forms small fibers that are fluorescing green, this is probably because of the composition of the specific deposited material including the contaminants or it could be a thiophene derivative, hard to determine as detail knowledge of the chemical composition of these fibers is required. Partially purified α-6T material shown in the fluorescence image in (b) indicates that contaminants tend to create holes on the deposited film. From this it can be said that purification of the material is essential on the growth process as well as the outcome.

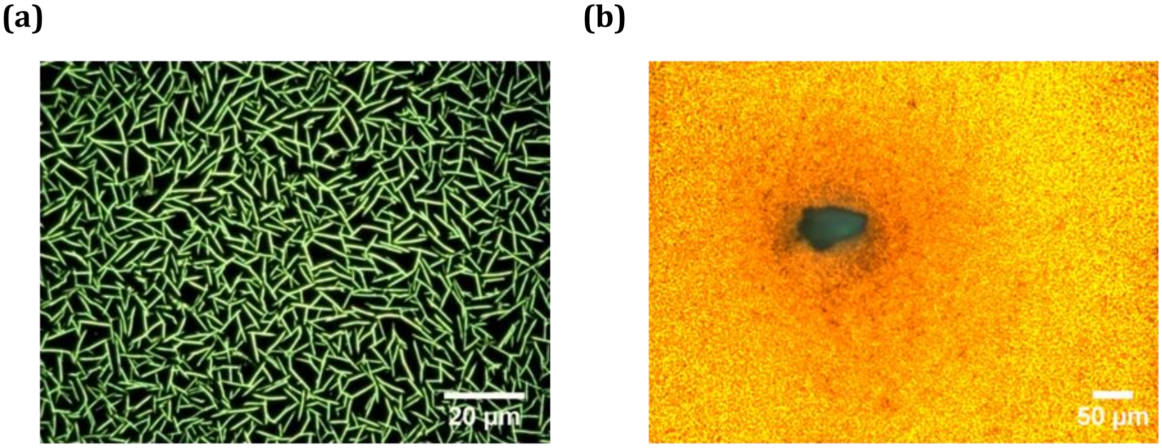

Figure 36. Contamination of α-6T material. In (a) α-6T probably mixed with contaminant compound forms fibers at room temperature and in (b) α-6T material (yellow) deposited around a contaminant (green) creating a hole.

Furthermore the different structural behavior of α-6T grown at different substrate temperatures reveals the dependency to the growth conditions (here at the substrates temperature) which is in agreement with what has been observed for vacuum evaporated α-6T (77) on Si where the dependency on the growth substrate temperature and deposition rate has been shown.

In order to check the crystallinity of the structures a sample made at TS=170˚C was observed under different polarization directions. Figure 37 shows polarized fluorescence microscopy images of α-6T nanofibers grown on 20nm Au at Ts=170˚C. The fibers are illuminated by unpolarized light under normal incidence and imaged through a polarizer.

The polarizer directions are marked with arrows on the images. It can be seen that the fiber fluorescence is dependent on the polarizer direction. The fluorescence is intense when the polarizer direction is approximately perpendicular to the nanofibers as seen for the red circled fiber in Figure 37 (a). Whereas when the polarizer direction is approximately parallel to the nanofibers as seen for the red circled fiber in Figure 37 (b) there is almost no fluorescence. The same behavior has been observed for p-6P on Au where the long axes of the molecules are mutually parallel to each other and perpendicular to the long nanofibers axes, which gives rise to polarized fluorescence since the dipole moment of the optical transition is aligned along the long molecular axes (71). The same theory can be adopted in the case of α-6T on Au, hence our observation can indicate that the nanofibers consist of mutually parallel molecules.

The fact that the nanofibers fluorescence lightly in the case of the transition dipole moment being perpendicular to the long molecular axes could be the indication of molecular orientation under different angles.

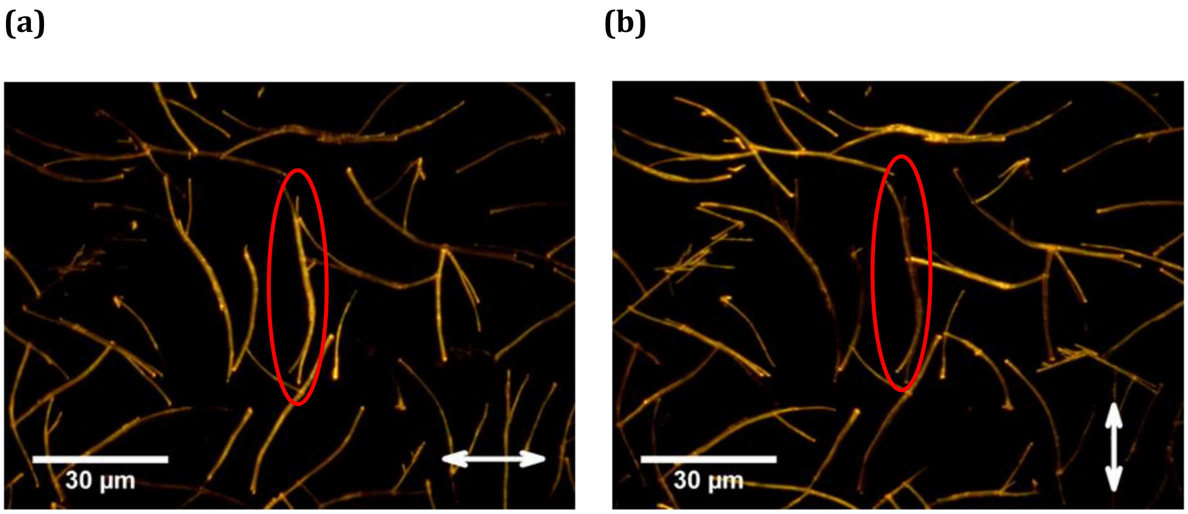

Figure 37. Fluorescence microscopy images of yellow emitting fibers grown at $T_S$=170˚C. The fibers are observed with a polarizer with polarization direction parallel (a) and perpendicular (b) as indicated by the arrows.

It was mentioned in Chapter 5 that changes involved the oven design, addition of one extra oven and the decrease in the oven/substrate distance.

It must be mentioned here that the above measurements were conducted using the old setup and that after the applied changes in the setup changes were observed also for the structural growth of α-6T.The key difference occurred at deposition of α-6T at room temperature ($T_S$=30˚C) where instead of nanostructures a rather thin film of α-6T is obtained at this temperature (Figure 38). The changes made in the setup can be accounted for this big difference, the deposition pressure has changed with the old setup the deposition of α-6T occurred usually at $10^{-7}$ Torr while with the new setup deposition pressure is usually $10^{-8}$ Torr. It could be also the case that the profile of the beam might have changed by decreasing the distance from the oven to the sample holder, since deposition occurs at the same deposition rate and under the same conditions.

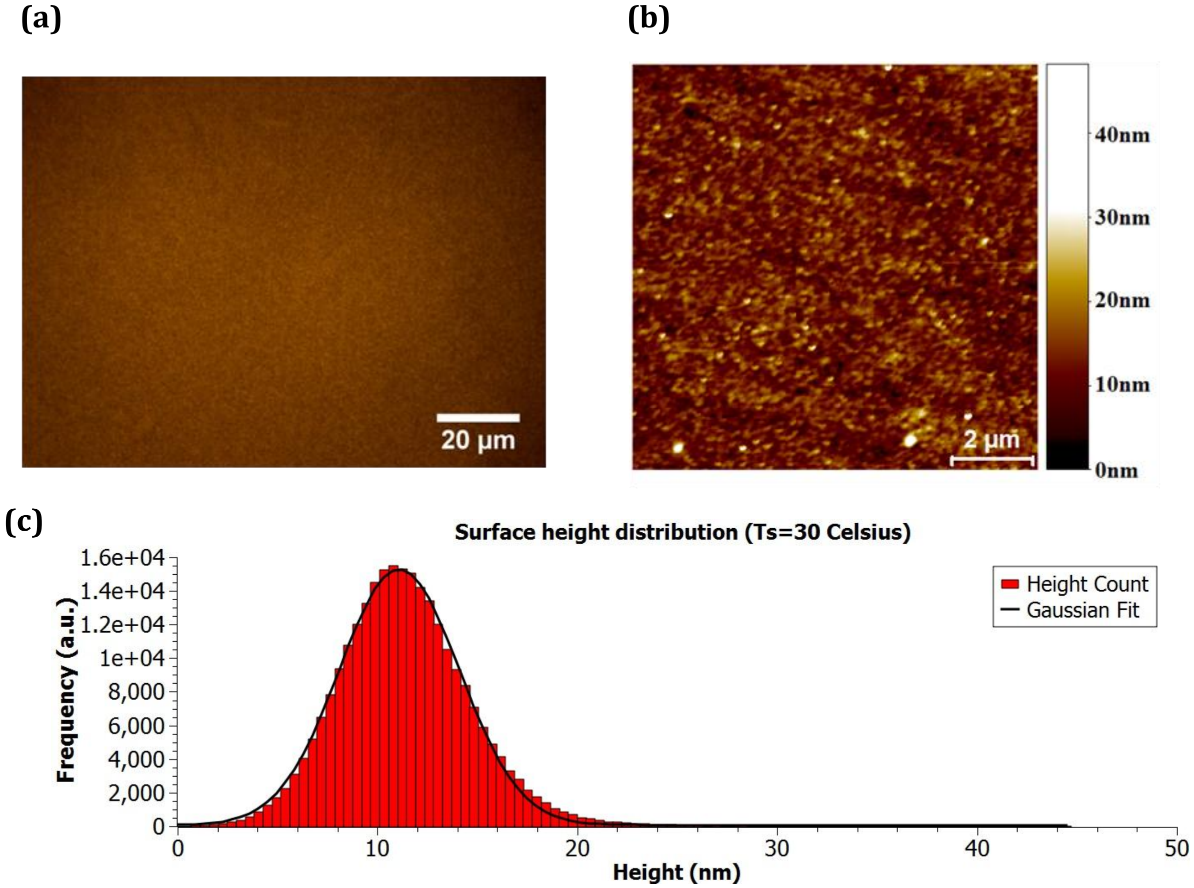

Figure 38. Fluorescent microscopy image of an α-6T on Au sample at $T_S$=30˚C made using the new OMBD setup in (a), while in (b) we can see a 10μm x 10μm AFM scan of the center of the sample that shows a film instead of structures observed with the previous OMDB setup. In (c) is shown a graph of the surface height distribution from a 10μm x 10μm area, the fit has center at 11.09nm.

For the rest deposition temperatures the structures were approximately the same in features and sizes with very small deviations from the above mentioned. Thus the temperature dependant behavior in the higher temperatures will not be analyzed further since in this case a compliance can be made with the results, and additionally the changes in the room temperature deposition are mostly favored and greatly accepted.

The new fluorescence image obtained for α-6T deposition at $T_S$=30°C is shown in Figure 38 (a) dictating a uniform thin film. Analysis of the AFM scan (Figure 38 (b)) showed that the root-mean-square roughness for this sample now is 3.52nm, whereas the surface roughness graph shown in Figure 38 (c) was fitted with a Gaussian fit that shows center at 11.09nm ±0.01nm. This new data analysis shows us that a thin film is formed over the sample with the new OMBD setup at $T_S$=30°C, where in comparison to the previous setup we saw that different structures are present at room temperature with different height distributions and roughness.

In Table 3 some of the parameters for comparison of the old samples with the new samples have been summarized, so it is possible compare the structural height growth of α-6T done with the old OMBD setup against the new. It can be observed that from the percentage difference in the measurements the highest deviation, of the order of above 50%, appears for the samples made at room temperature.

From the comparison in Table 3 we can observe that the height of the structures increases gradually from room temperature until 170°C. This data can be used in order to determine the structures that will be favored for solar cell fabrication as structuring of the organic layer in solar cells has been troubling even the fabrication of BHJ devices where control over the films morphology is required (52), (5), (4), (78).

Different heights can result in different type of solar cells. α-6T at room temperature with a $C_{60}$ layer deposited on top of it could give us a bilayer device while rougher structures like the fiber formation at $T_S$=100°C combined with a thin layer of α-6T to cover the Au surface followed by deposition of $C_{60}$ layer could result in a perfectly structured solar cell overcoming the disadvantage of structuring in bulk-heterojunction solar cells.

Table 3. Comparison of samples at $T_S$=30˚C (5μm x 5μm), $T_S$=100˚C (10μm x 10μm AFM scan) and 170˚C (30μm x 30μm AFM scan) obtained with the old setup against the samples at the same substrate temperatures obtained with the new setup.

| Substrate Temperature | Parameter | Old Samples | New Samples | Percent Difference |
|---|---|---|---|---|
| **30˚C** | RMS Roughness | 12.3nm | 3.48nm | 75.6% |
| | Average Height | 19.2nm | 12.03nm | 64.3% |
| **100˚C** | RMS Roughness | 73.82nm | 84.80nm | 13.9% |
| | Average Height | 64.24nm | 72.81nm | 12.5% |
| | Average Width | 0.30μm | 0.35μm | 15.4% |
| | Approximate Length | ≤2μm | ≤5μm | 85% |
| **170˚C** | RMS roughness | 63.86nm | 64.32nm | 0.7% |
| | Average Height | 184.13nm | 176.967nm | 3.9% |
| | Average Width | 1μm | 0.68μm | 38% |

The photoluminescence spectrum of α-6T in (79) was used as reference to compare our findings. A general comparison between a spectra obtained of a new sample made at $T_S$=30˚C with the reference (79) is shown in Figure 39.

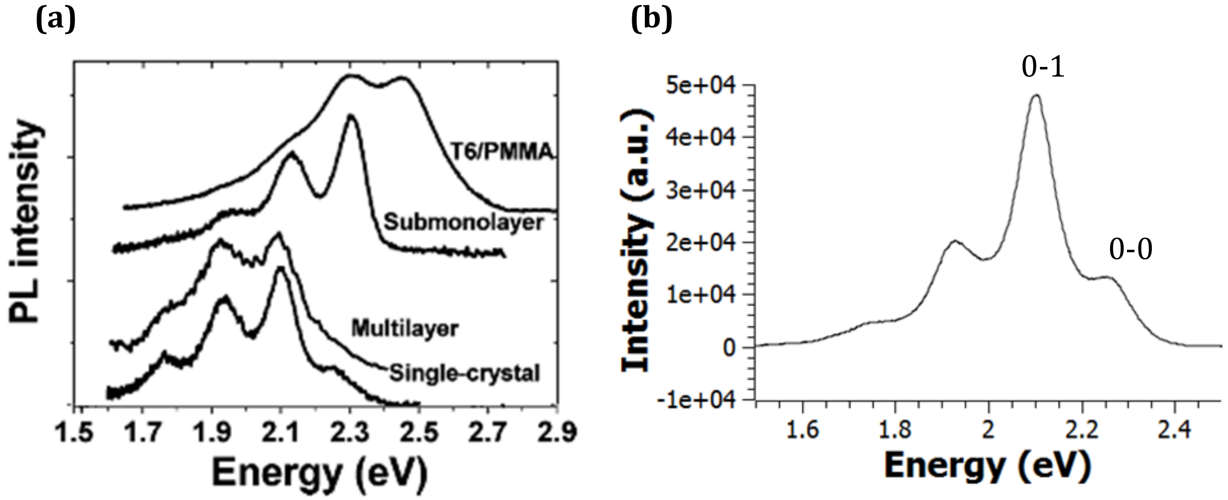

Figure 39. (a) Room-temperature PL spectra of T6/PMMA, submonolayer film, multilayer film, and single crystal from (79), and in (b) spectra obtained for α-6T grown on 20nm Au at room temperature.

In (a) is shown the reference photoluminescence spectra of T6/PMMA, submonolayer film, multilayer film and single crystal obtained for α-6T grown at room temperature on silicon dioxide (image from (79)). In (b) we show the spectra obtained with the new OMDB setup for α-6T grown at room temperature $T_S$=30˚C.

By a first approximation it can be observed that the spectrum in (b) is similar in shape with the spectra for the single α-6T crystal in (a). Additionally in the reference is mentioned that the 0-0 transition for the single crystal lies at 2.26eV which is in agreement with our case where the peak center lies at 2.25eV, while the 0-1 transition presents the highest photoluminescence (peak at 2.11eV). The relevance of our findings to the reference is evident also with the other peaks at 1.95eV and at 1.72eV but the author of the reference (79) does not match peaks at values to particular transitions.

In Figure 40 (a) we show the normalized original spectra obtained for samples grown with the old OMDB setup, while in (b) we show the cumulative spectra obtained from the Gaussian fits conducted on the peaks in (a). Accordingly we show the same in (c) and (d) for samples obtained with the new OMBD setup. The fits have been conducted in order to obtain the center peak values of the spectra that are summarized in Table 4.

Moreover the peaks from the spectra in Figure 40 show shifts in intensity and in slightly in wavelength. These shifts can be related to defects in the structure or different packing of the molecules. Moreover the spectra obtained from samples made with both setups look almost identical if we deduct the shifts.

It is assumed that the differences in intensities between samples at different substrate temperatures generally were due to the amount of light gathered for the measurement. We did not conduct any further analysis of the spectra as our concern was mainly to obtain α-6T structures and make sure that these structures are from α-6T by looking at the spectrum and comparing it to work that already has been done. Further investigation on why the spectrum is as it is with the shifts is left for future work.

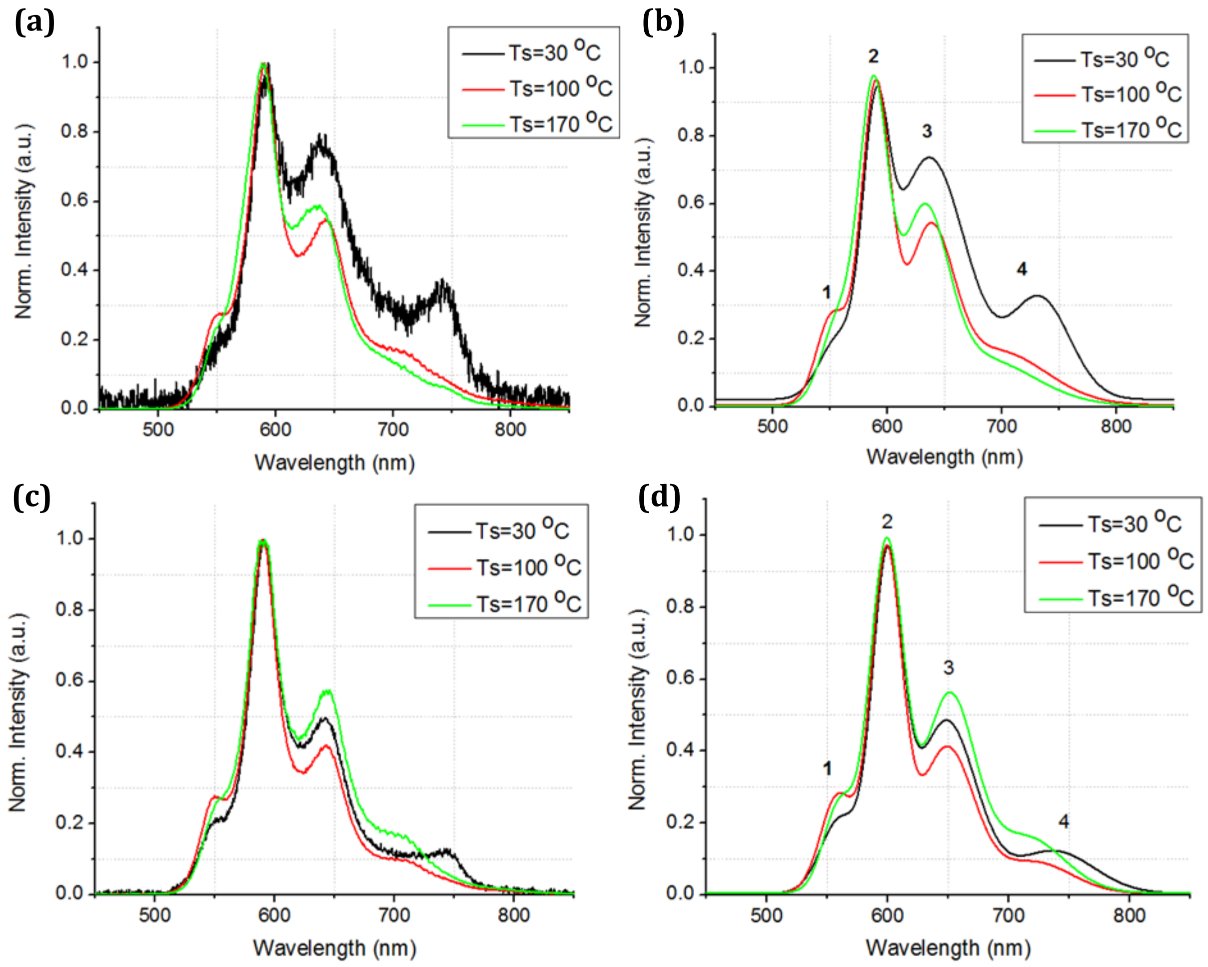

Figure 40. Emission intensity spectra normalized obtained from α-6T samples at $T_S$=30˚C, $T_S$=100˚C and $T_S$=170˚C from the old OMBD setup (a) and the new setup (c). Gaussian fits for each spectra resulted in a cumulative fit that is shown in (b) for the old setup and in (d) for the new setup. The numbering denotes the Gaussian fits that were calculated in order to derive the centers.

Table 4. Center values obtained from the Gaussian fits conducted for each peak in every spectra at Ts=30 different temperatures.

| | Gaussian Fit | Ts=30 | Ts=100 | Ts=170 |
|---|---|---|---|---|
| **Old OMBD** | 1 | 555.4 ±1.6 | 551.7 ±0.2 | 557.4 ±0.5 |
| | 2 | 589.2 ±0.3 | 589.5 ±0.1 | 587.5 ±0.1 |
| | 3 | 636.3 ±0.5 | 636.6 ±0.1 | 631.4 ±0.1 |
| | 4 | 732.7 ±0.6 | 694.5 ±1.6 | 680.2 ±2.5 |
| **New OMDB** | 1 | 553.7 ±0.3 | 551.9 ±0.2 | 553.2 ±0.2 |
| | 2 | 590.4 ±0.1 | 589.7 ±0.1 | 589.8 ±0.1 |
| | 3 | 636.8 ±0.2 | 637.2 ±0.2 | 638.9 ±0.2 |
| | 4 | 722.2 ±0.6 | 706.3 ±1.1 | 699.3 ±1 |

## 6.2 Solar Cell structures

As it has been continuously mentioned, the above findings are to be implemented into a solar cell structure. In the ideal case scenario the organic nanofibers would be used as starting material where 20nm of α-6T would be deposited at an elevated temperature.

But because of the fiber structure there would exist an exposed gold layer that could come into contact with the $C_{60}$ forming a short circuit, this would make the device useless. Hence in order to cover the Au exposed parts additional 20nm of α-6T deposited at room temperature would provide the necessary cover.

In order to get to the ideal case it was decided to start by making a simple bilayer organic solar cell in order to inspect first that a solar cell structure with the selected materials would show photovoltaic effect.

To do this a bilayer structure from (4) is going to be used as a reference, where it has been shown by Sakai et al. that in a 1:1 ratio of α-6T:$C_{60}$ organic layer deposited on a substrate, photovoltaic effect is observable with efficiency of the order of 0.75%, with the organic layer having a total thickness of 50nm. To make the solar cell structure in (4) they have used as a substrate a glass covered with 150nm ITO film on which they spin coated 30nm PEDOT:PSS. Then they deposited the active layer consisting of α-6T and $C_{60}$ through sequential vacuum evaporation. On top of the $C_{60}$ they deposited 6nm BCP followed by 100nm thick Ag:Mg film that was used as a cathode.

The first solar structure that was made, for this research, is shown in Figure 41 (a). The difference with the reference solar cell structure is the lack of poly [3,4-ethylenedioxythiophene]-poly [styrenesulfonate] (PEDOT:PSS) layer as well as BCP layer, whereas instead of ITO, Au covered glass was used and Al cathode instead of Ag:Mg.

PEDOT:PSS is generally used on ITO substrates as a buffer layer. Namely PEDOT:PSS smoothes the ITO surface imperfections, it reduces significantly the surface roughness, modifies the work function of the ITO and serves as an electron blocking layer collecting holes more efficiently (80). But evaporation of 6T molecules on PEDOT:PSS leads to molecular orientation perpendicular to the substrate, which lowers the carrier mobility (81) and is generally not favored in organic solar cells as the charge transfer is done through the π-π bonding formed when molecules reside parallel to each other.

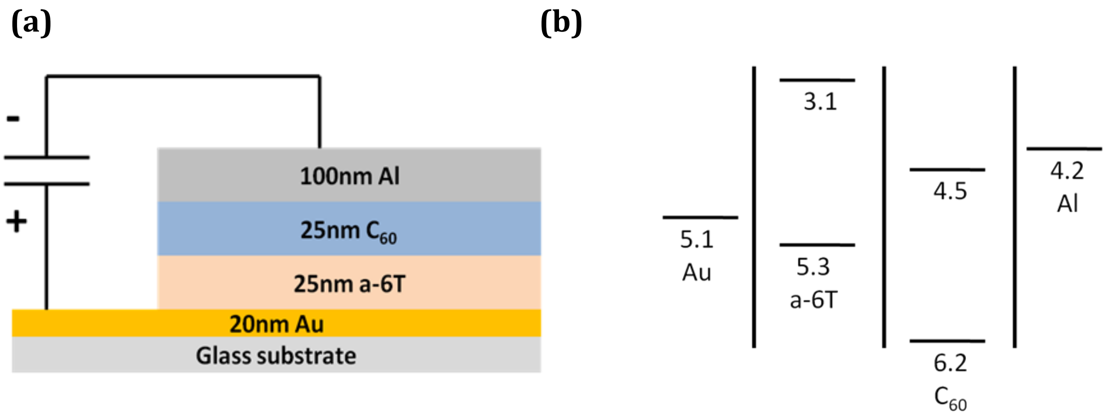

Figure 41. (a) Schematic device structure of 6T/C60 bilayer heterojunction structure, and (b) diagram showing energy levels of the α-6T/C60 bilayer structure under flat band conditions. (Energy levels after (4), (85), (65)).

This type of structure did not show any solar cell behavior as short circuit conditions were observed. This could be the probability of Al diffusing into the organic layer during thermal evaporation, hence either destroying the structure or making contact somehow with the Au layer, therefore just for precaution a thin layer of BCP was deposited on tope the $C_{60}$ layer.

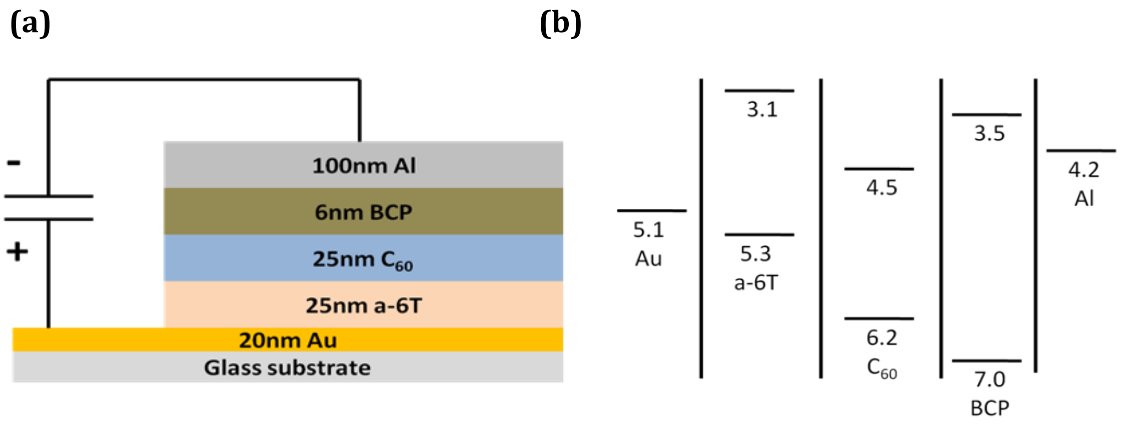

Figure 42. (a) Schematic device structure of 6T/C60/BCP heterojunction structure, and (b) diagram showing energy levels of the α-6T/C60/BCP structure under flat band conditions. (Energy levels after (4), (85), (65)).

The BCP layer had a thickness of 6nm again according to the reference paper and the structure was as shown in Figure 42.

The addition of BCP layer in a bilayer device solar cell structure has been proven of importance. It can serve as a protective film during thermal evaporation of Al contact and therefore preventing the Al of diffusing into the organic layer, and additionally it enhances the efficient electron transport from $C_{60}$ to the Al electrode (82),

Pure ohmic behavior was again observed in this type of structure. Even in the case of increasing the organic total layer from 50nm to 100nm the device was still acting as a pure resistance. The probability of the buffer layer of not being thick enough was also investigated by increasing the thickness up to 17nm (82).

The investigation of finding a solution turned towards the probability of Al electrode making contact with the Au layer through defects in between of the Au electrode and the organic interface. The gold covered glass samples were characterized directly after Au deposition with AFM, as well as under the microscope before loading them into the OMBD chamber Figure 43.

In Figure 43 (a) an AFM image of a sample directly after Au deposition (20nm) in the cleanroom is shown, where is can be observed that some type of grain is present.

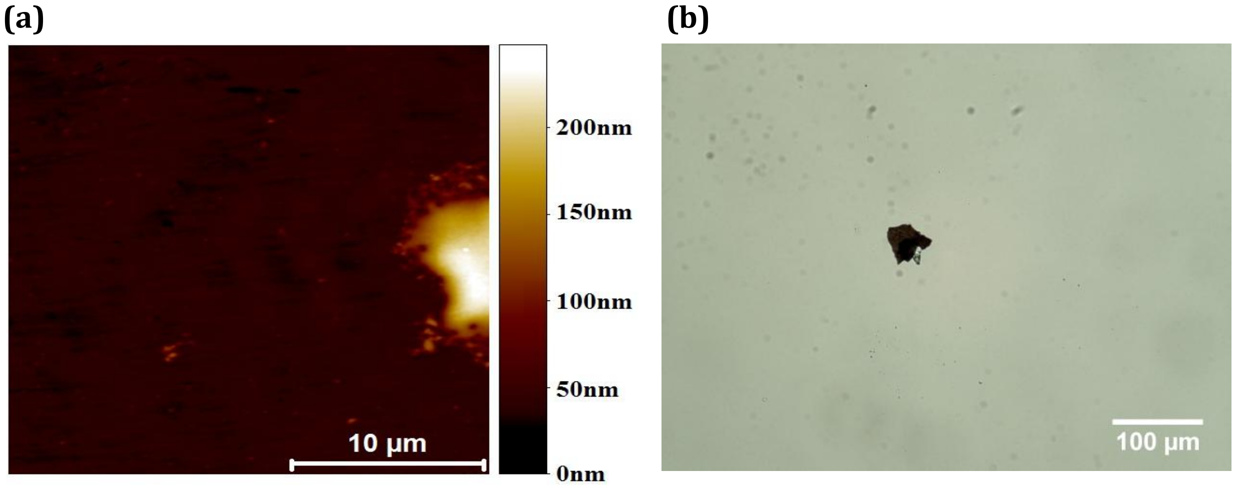

Figure 43. (a) AFM image of 20nm Au deposited on glass substrate directly after deposition indicating a defect on the film, width≈6µm and height≈186nm, and (b) a microscopy image showing contaminates residing on the Au covered glass substrate.

In Figure 43 (b) a microscope image of an Au sample shows that that dust particles reside on the surface.

Dust particles were observable even after cleaning the samples with acetone and sonication. For the AFM sample it can be assumed that because of the flatness and the small size of the defect (height≈186nm, width≈6μm), deposition of α-6T could cover it without leaving some area exposed. On the other hand the dust particle residing on the surface, seen in the microscope image, could result in a contaminated sample after α-6T deposition. This requires further investigation, but it can be stated here that contamination is an issue that needs to be resolved in order to obtain clean samples.

In order to investigate if the organic material that was used for deposition present any type of photovoltaic effect a solar cell structure was fabricated according to the reference paper (4).

To do so an ITO glass substrate from (Sigma Aldrich, surface resistivity=30-60Ω/sq) was used. A part of ITO was etched in order to create the Al contacts later. The reason for that is that in general in a solar cell structure one has a metal anode, the organic layer and a metal cathode. Those two metal electrodes except of their function in the solar cell structure they are also used in order to contact the solar cells with any type of testing station.

If the Al cathode in our case lies directly above the organic interface any metallic contact to it could damage the underlying layer and create shorts when testing , hence by depositing the Al layer on the glass one avoids damaging the structure. And since we do not want to deposit the Al on the Au layer the etching of an ITO covered area is necessary.

The etching was done using a small amount of Zinc powder (Merck K16748689) mixed with distilled water, and soaking the exposed part of the sample in mixture. Pouring HCl in this mix creates a chemical reaction that etches the exposed ITO part.

The samples were then taken to the cleanroom where they were cleaned following the clean processes mentioned in Chapter 5. PEDOT:PSS (Heraeus Clevios™) was deposited on the ITO film by spin coating (3000rpm for 120s) and baking (135˚C for 15min), the reported thickness for these parameters is 30nm. The parameters are according to (4).

The organic active layer was deposited via sequential deposition of the organic materials consisting of 25nm α-6T at 0.4Å/s, followed by 25nm $C_{60}$ at 0.4Å/s.

Deposition rates have been arbitrary chosen as they are not reported in (4). On top of the $C_{60}$ film a layer of BCP was deposited, with thickness of 6nm at 0.1Å/s, followed by 100nm Al film as the cathode instead of Ag:Mg. The final structure is shown in Figure 44.

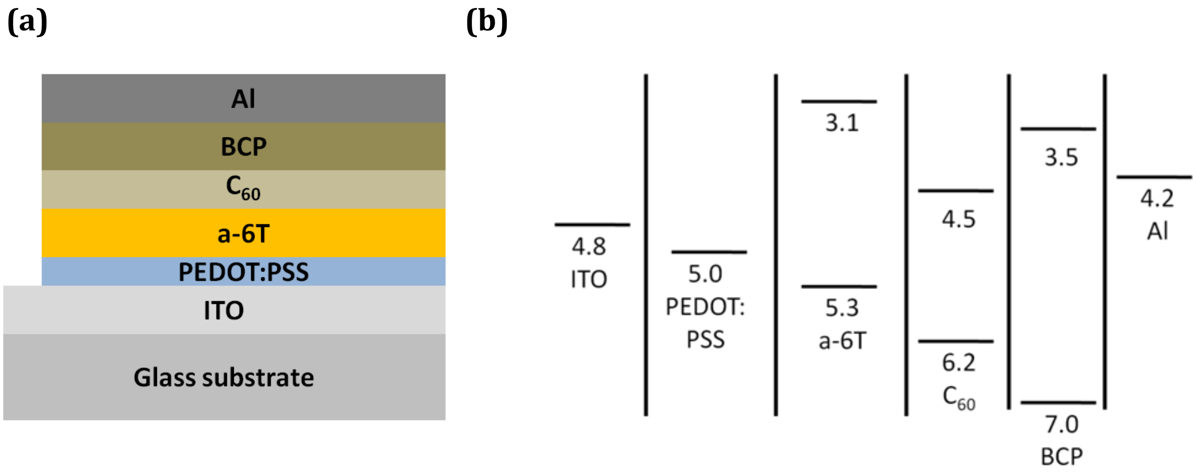

Figure 44. (a) Schematic device structure of 6T/C60 bilayer heterojunction solar cell structure, and (b) diagram showing energy levels of the structure under flat band conditions. (Energy levels after (4), (85)).

I-V characteristics were obtained with a photovoltaic measurement setup made by Michal Radziwon. A Keithley 2400 source meter was used as a voltage source for bidirectional sweep from -0.1 to 0.4 Volt. The sweep was consisting of 60 points with 3sec. settling time after each voltage step. The setup of source meter was done from a Labview program through a GPIB protocol.

A solar simulator equipped with a Universal Arc power supply (Newport Model: 69907) and an Arc lamp housing (Newport Model: 67005) equipped with a 150W Xenon lamp provided the necessary illumination using a AM 1.5G filter.

Two measurements were conducted for each solar cell structure: at ambient light and under illumination that was arbitrary chosen and measured at 1.6 Suns. Figure 45 (a) shows the I-V characteristic for the reference solar cell, whose structure can be seen in Figure 44 (a). Figure 45 (b) shows the I-V characteristics obtained for the bilayer devices made on Au covered glass mentioned before.

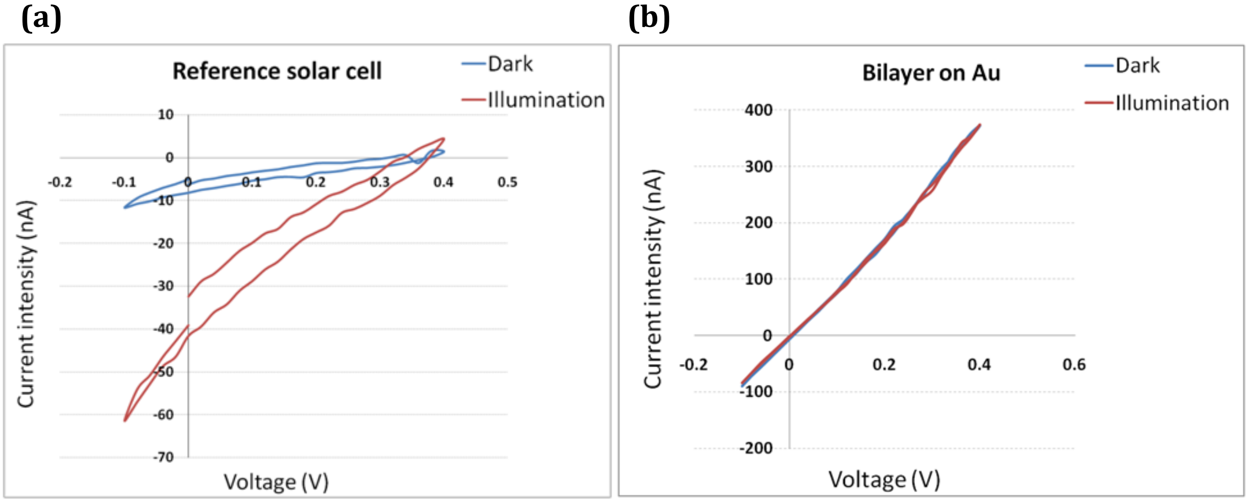

Figure 45. (a) I-V characteristic of the reference solar cell blue line is with ambient light, while the red line is under illumination. (b) I-V characteristic of bilayer device (25nm a6-T:25nm $C_{60}$) made on Au covered glass, ohmic behavior is evident.

It can be observed from the I-V characteristic in Figure 45 (a) that under practically no illumination (ambient) the structure behaves like a diode while under illumination the structure produces current, evidence of photovoltaic effect. The facts that trace and retrace from the sweep do not much denote defects in the structure. Analysis of the trace of the I-V curve under illumination showed that the solar cell delivers $V_{OC}$= 0.32V, $I_{SC}$= 3.241e-08A, $J_{SC}$≈84nA/cm$^2$ and FF=0.224. The efficiency of the solar cell was calculated to be n=0.00098%.

The efficiency of the reference solar cell is very low compared to the one in the reference (4) where the efficiency reported was *n*=0.75%. It can be because the process and the conditions of the production of the current structure might defer in a large extent compared to the one reported. Moreover it was of interest to observe any photovoltaic effect in order to assure that the deposited active layer can act as a solar cell.

The characteristic shown in Figure 45 (b) denotes that fabricated structures behave as a pure resistance with no photovoltaic effect. There are no data for the present on why this is observed, only the assumption that somehow gold comes into contact either with the Al electrode. In any case further research is required to try and obtain a working device on Au substrates.

# Conclusions

Control over structuring the active layer is organic solar cells has been prolonged troubling the photovoltaic industry. Even the best BHJ devices are based on the probability of the photogenerated exciton to diffuse towards an active layer within the solar cell where it is going to be split into an electron and a hole. Organic solar cells being limited in one case by the small diffusion length of the excitons and in the other case by low mobility due to the amorphous nature usually of the organic materials point out the need for the ability to structure active layer composed of crystalline organic materials. The attractive properties for photovoltaic applications of α-6T as donor material and $C_{60}$ as acceptor material are limited by the ability on control over the morphology of the structures.

Organic materials were deposited via organic material beam deposition system (OMBD). Different paragons affecting the deposition process have been discussed (cleanliness, OMBD setup ect.). The OMDB setup used for this research has been presented extensively along with the related changes applied to it. The changes were mandatory as short circuit conditions affected the readings of the equipment regarding deposition of organic material. The major changes that were done included new oven designs for deposition of α-6T, $C_{60}$ and BCP, and sample holder modifications for better temperature distribution over the samples area. It has been concluded that careful design and planning regarding the OMBD setup in advance can save a lot of precious time during deposition experiments. Repeatable and concrete results are vital and based on the setup. Changes can affect the experiments forcing one to start them over again in order to obtain solid results.

Growth control of α-6T on Au has not been demonstrated previously. Square samples with 20nm Au were prepared to be used as a substrate for the deposition of α-6T. The structural behavior of α-6T was examined by deposition at different sample holder temperatures. It has been demonstrated, that α-6T deposited via OMBD process on Au covered glass substrates allows control over the growth behavior of the material. By tuning the substrates temperature one can go from a thin film at room temperature (30˚C) to elongated fibers at substrate temperatures above 100˚C until 180˚C where the growth stops. To show this and to determine the sizes (roughness, height, width and length) of the structures over the different growth temperatures the samples were characterized using fluorescence microscopy and AFM. Additionally fluorescence spectroscopy was used to compare the emission spectra of the samples to a reference (79) and observe the relevance of the findings to spectra of a 6T single crystal. Illumination of the samples under normal incidence and observation through a polarizer showed indications of different molecular orientations.

Before incorporating any α-6T structures (clusters or fibers) into a solar cell, a bilayer device was fabricated according to reference (4), in order to observe the presence of any photovoltaic effect. The device was fabricated on a glass substrate covered with 20nm Au forming the anode. The organic layer was formed by sequential deposition of 25nm α-6T followed by 25nm of C60. To complete the device 100nm of Al were thermally evaporated and served and the cathode. For the present structures deposited on Au show ohmic behavior and they are not fully adoptable for solar cell fabrication as better understanding of structural order of the intermediate layers is required.

Fabrication of a bilayer device with same organic material ratio on ITO substrates covered with PEDOT:PSS showed indications of photovoltaic effect, indicating the function of α-6T and $C_{60}$ in solar cell structures.

There is still a lot of room for further development and improvement as this is an experimental research. Nevertheless, this project proved to be a very challenging and rewarding experience as a huge amount of knowledge and a better understanding in building an OMBD, solar cells and growth of organic materials was acquired. Yet there is still so much to learn!

# Outlook

Deposition of organic materials via OMBD relies on the setup parameters (oven design, oven/holder distance ect.) as well as at the deposition conditions (pressure, sample temperature ect.). More specifically homogeneous temperature distribution at the sample surface can lead to more accurate results and identical structures over the whole sample.

It was shown that due to this effect the measurements of the growth of α-6T were conducted continuously at the approximate center of the sample as if going towards the edges of the sample the growth behavior showed slight changes due to different temperature distributions. This can be attributed due to either bending of the copper plates or not full contact of the thermocoax that was sandwiched between the copper plates.

In order to avoid these effects, to be minimized or perhaps eliminated a new sample holder design is required. This could be done by incorporating two copper plates with grooves equal to half the diameter of the thermocoax, on one side of each plate. With the thermocoax placed in the grooves and sandwiched in between, the bending of the material can be limited to a large extend, and simultaneously a stable, constant contact will exist between thermocoax and plates. In addition to that a water cooling system mounted on the plates can allow investigation of the behavior of α-6T at temperatures below 30˚C.

Hence this change of the sample holder can have a threefold advantage. First homogenous temperature distribution over the whole sample area, secondly homogenous temperature distribution and deposition of α-6T to up to three samples upon one deposition (considering the size of current setup), and third deposition at lower temperatures which could be of interest for thin film deposition.

In the current study Au anode was deposited over the largest area on the sample in the general case, while the Al cathode was deposited through alumina vacuum foil masks resulting in three to four usable devices on a 25mm x 25mm area. By making proper masks for depositing the materials though them could increase the usable devices for experiments, as Au thin film can form defect structures upon deposition over a large area which is dependent on defects present on the glass substrate, for example scratches. On the other hand Al deposited through the homemade Al masks tends to spread at the edges instead of forming better defined rectangular structures, because of gaps present being present between foil mask and sample. Three masks for deposition of Au, organic material and Al, properly aligned together would result in more and better defined isolated structures. After obtaining a working device in a small scale the investigation could proceed forward to larger areas.

In addition improvements can be applied on the Al deposition process by incorporating a crystal microbalance for monitoring the thickness of the material and the deposition rate more accurately.

Contaminants are a serious issue as particles deposit on the sample surface upon exposure to ambient environment. This shows the necessity for experiments under cleaner environment and limitation of the contaminations and requires further investigation. It might seem futuristic but making a homemade glove box surrounding the chamber would avoid contamination of the samples at a large extent.

It was shown that a working device can be obtained using the current setup and processes, organic layer deposited on ITO substrate covered with PEDOT:PSS, while organic layers on Au covered glass substrate do not show signs of photovoltaic effect. Further research can be focused on the incorporation of the different materials in the structures made on Au samples in order to point out the reason of why those devices do not operate and how this can be improved.

A starting point towards this would be to apply the previous mentioned changes on the production setup. The next step would be to produce a fully functional solar cell based on a reference cell. By doing these, questions like if the specific organic material and setup work for solar cells could be eliminated and the research on Au samples could move forward.

# Bibliography

1. Solar energy. *EEM 08 International Conference on the European Electricity Market.* [Online] [Cited: May 30, 2012.] http://www.eem08.com/solar-energy.

2. **Koppelaar, R.** World energy consumption - beyond 500 exajoules. *Energy Bulletin.* [Online] 2012. [Cited: May 29, 2012.] http://www.energybulletin.net/stories/2012-02-16/world-energy-consumption-beyond-500-exajoules.

3. Technologies. *Solarbuzz.* [Online] 2012. [Cited: May 30, 2012.] http://www.solarbuzz.com/going-solar/understanding/technologies.

4. *Efficient oligothiophene:fullerene bulk heterojunction organic photovoltaic cells.* **Sakai J., Taima T., Saito K.** 5, 2008, Organic electronics, Vol. 9, pp. 582-590. DOI: 10.1016/j.orgel.2008.03.008.

5. *Polymere-Fullerene Composite Solar Cells.* **B.C., Thompson and J.M.J, Fréchet.** 1, 2007, Angew. Chem. Int. Ed., Vol. 47, pp. 58-77. DOI: 10.1002/anie.200702506.

6. *Molecular model T6:C60 bulk-heterojunction solar cells.* **S., Alem, et al.** 3, J. Vac. Sci. Technol. A, Vol. 24, pp. 645-648. DOI: 10.1116/1.2183160.

7. *Sexithiophene-C60 blends as model systems for photovoltaic devices.* **S.C., Veenstra, et al.** 1-3, 1997, Synthetic Metals, Vol. 84, pp. 971-972. DOI: 10.1016/S0379-6779(96)04235-X.

8. *Effect of traps on the performance of bulk heterojunction organic solar cells.* **M.M., Mandoc, et al.** 26, 2007, App. Phys. Let., Vol. 91, pp. 263505 (1-3). DOI: 10.1063/1.2821368.

9. **K., Al-Shamery, H-G., Rubahn and H., Sitter.** *Organic Nanostructures for Next Generation Devices.* s.l. : SpringerLink, 2008. DOI: 10.1007/978-3-540-71923-6.

10. *Tailoring the growth of p-6P nanofibers using ultrathin Au layers: an organic-metal-dielectric model system.* **F., Balzer, et al.** 4, 2006, Nanotechnology, Vol. 17, pp. 984-991. DOI: 10.1088/0957-4484/17/4/024.

11. Uses of Solar Energy. *Solarbuzz.* [Online] [Cited: April 21, 2012.] http://www.solarbuzz.com/going-solar/using/uses.

12. Rise of petrol price and use of solar energy. *HubPages.* [Online] 2011. [Cited: April 21, 2012.] http://liltu88.hubpages.com/hub/rise-of-petrol-price-and-use-of-solar-energy.

13. **L., Bergeron.** Wind, water and sun beat other energy alternatives, study finds. *Stanford University News.* [Online] 2008. [Cited: April 21, 2012.] http://news.stanford.edu/news/2009/january7/power-010709.html.

14. **Nave, R.** P-N Junction. *Hyperphysics.* [Online] [Cited: March Saturday, 2012.] http://hyperphysics.phy-astr.gsu.edu/hbase/solids/pnjun.html#c3.

15. How does Solar Power work? *solarpower.* [Online] [Cited: April 4, 2012.] http://solarpower.com/how-does-solar-power-work/.

16. Voltage and Current. *All About Circuits.* [Online] [Cited: April 3, 2012.] http://www.allaboutcircuits.com/vol_1/chpt_1/4.html.

17. **Pagliaro, M., Palmisano, G. and Ciriminna, R.** *Flexible Solar Cells.* s.l. : WILEY-VCH, 2008. ISBN:978-3-527-32375-3.

18. **R., Gaughan.** How to Plot Solar Cell I-V Characteristics With Load Line. *eHOW.* [Online] [Cited: April 3, 2012.] http://www.ehow.com/how_8711500_plot-iv-characteristics-load-line.html.

19. *Solar cell fill factors: General graph and empirical expressions.* **Green, M. A.** 8, 1981, SolidState Electronics, Vol. 24, pp. 788-789. DOI: 10.1016/0038-1101(81)90062-9.

20. **Nelson, J.** *The Physics of Solar Cells.* s.l. : Imperial College Press, 2003. ISBN: 978-1860943492.

21. *The Path to 25% Silicon Solar Cell Efficiency: History of Silicon Cell.* **Green, M. A.** 3, 2009, Prog. Photovolt: Res. Appl., Vol. 17, pp. 183-189. DOI: 10.1002/pip.892.

22. Solar Efficiency Limits. *Solar Cell Central.* [Online] [Cited: April 22, 2012.] http://solarcellcentral.com/limits_page.html.

23. **C., Honsberg and S., Bowden.** Photovoltaic Effect. *PV Education.* [Online] [Cited: May 19, 2012.] http://pveducation.org/pvcdrom/solar-cell-operation/photovoltaic-effect.

24. ASTM G173 - 03(2008). *ASTM International.* [Online] 2008. [Cited: April 17, 2012.] http://www.astm.org/Standards/G173.htm. DOI: 10.1520/G0173-03R08.

25. Russell Ohl. *IEEE Global History network.* [Online] [Cited: April 17, 2012.] http://www.ieeeghn.org/wiki/index.php/Russell_Ohl.

26. *Industrial Silicon Wafer Solar Cells.* **D-H, Neuhaus and A., Münzer.** 2007, Advances in OptoElectronics, Vol. 2007, p. 15. DOI:10.1155/2007/24521.

27. *19.8% efficient "honeycomb" textured multicrystalline and 24.4% monocrystalline silicon solar cells.* **J., Zhao, et al.** 14, 1998, Appl. Phys. Lett., Vol. 73, p. 3. DOI: 10.1063/1.122345.

28. *Influence of wafer thickness on the performance of multicrystalline Si solar cells: an experimental study.* **J., Tool C. J., et al.** 4, 2002, Prog. Photovolt: Res. Appl., Vol. 10, pp. 279-291. DOI: 10.1002/pip.421.

29. *Three-dimensional nanopillar-array photovoltaics on low-cost and flexible substrates.* **Fan, Zhiyong, et al.** 2009, Nature Materials, Vol. 8, pp. 648-653. DOI: 10.1038/nmat2493.

30. **Yastrebova, V.N.** SUNLab Whitepapers. *SUNLAB.* [Online] 2007. [Cited: April 18, 2012.] http://sunlab.site.uottawa.ca/pdf/whitepapers/HiEfficMjSc-CurrStatus&FuturePotential.pdf.

31. **Shahan, Z.** High-Efficiency Solar Cells Getting More Efficient, Cheaper. *CleanTechnica.com.* [Online] 2011. [Cited: April 18, 2012.] http://cleantechnica.com/2011/02/17/high-efficiency-solar-cells-getting-more-efficient-cheaper/.

32. Konarka Technologies Advances Award Winning Power Plastic Solar Cell Efficiency with 9% Certification. *MarketWatch.* [Online] 2012. [Cited: April 18, 2012.] http://www.marketwatch.com/story/konarka-technologies-advances-award-winning-power-plastic-solar-cell-efficiency-with-9-certification-2012-02-28.

33. **A., Carr, et al.** Solar Cell Principles and Applications. *ESDAL COLLEDGE.* [Online] 1999. [Cited: April 18, 2012.] http://www.esdalcollege.nl/eos/vakken/na/zonnecel.htm.

34. Power Plastic Products. *KONARKA.* [Online] 2012. [Cited: April 18, 2012.] http://www.konarka.com/index.php/power-plastic/power-plastic-products/.

35. Progress Report 1 - Processable Organic Photovoltaics. *Mitsubishi Chemical.* [Online] [Cited: April 18, 2012.] http://www.m-kagaku.co.jp/english/aboutmcc/RC/special/feature1.html.

36. **Ver-Bruggen, S.** Solarmer organic solar cell efficiency nears 8.5%. *Plus Plastic Electronics.* [Online] 2012. [Cited: April 18, 2012.] http://www.plusplasticelectronics.com/energy/solarmer-organic-solar-cell-efficiency-nears-8-5-percent-43149.aspx.

37. Gridmaxx 2.3kw Bundle Pack. *Silicon Solar.* [Online] [Cited: May 30, 2012.] http://www.siliconsolar.com/gridmaxx-2-3kw-bundle-pack.html.

38. UCLA's Yang Yang on Upping the Efficiency of Polymer Solar Cells. *Science Watch.* [Online] 2011. [Cited: May 30, 2012.] http://www.sciencewatch.com/inter/aut/2011/11-may/11mayYang/.

39. **Carpi, A.** Organic Chemistry: An Introduction. *Visionlearning.* [Online] 2003. [Cited: May 20, 2012.] http://www.visionlearning.com/library/module_viewer.php?mid=60.

40. *Coulomb Barrier for Charge Separation at an Organic Semiconductor Interface.* **Muntwiler, M., et al.** 19, 2008, Phys. Rev. Lett., Vol. 101, p. 4. DOI: 10.1103/PhysRevLett.101.196403.

41. *Charge Carrier Transporting Molecular Materials and Their Applications in Devices.* **H., Kageyama and Y., Shirota.** 4, 2007, Chem. Rev., Vol. 107, pp. 953-1010. DOI: 10.1021/cr050143.

42. *Efficiency Improvement of Organic Solar Cells by Tuning Hole Transport Layer with Germanium Oxide.* **C., Moon Kee, et al.** 1, 2012, J Nanosci Nanotechnol., Vol. 12, pp. 623-628(6). DOI: 10.1166/jnn.2012.5368.

43. *Organic solar cells: An overview.* **Hoppe, H. and Sariciftci, N. S.** 7, 2004, J. Mater. Res., Vol. 19. DOI: 10.1557/JMR.2004.0252.

44. **Deibel, C.** Picture Story – How Do Organic Solar Cells Function? *Notes on Disordered Matter.* [Online] 2008. [Cited: April 19, 2012.] http://blog.disorderedmatter.eu/2008/06/05/picture-story-how-do-organic-solar-cells-function/.

45. **R., Raghu.** Organic solar cells. *National Centre for Photovoltaic Research and Education (NCPRE).* [Online] 2011. [Cited: April 24, 2012.] http://www.ncpre.iitb.ac.in/page.php?pageid=50&pgtitle=Organic-Solar-Cells.

46. *Organic photovoltaic films.* **Nelson, J.** 1, 2002, Current Opinion in Solid State and Materials Science, Vol. 6, pp. 87-95. DOI: 10.1016/S1359-0286(02)00006-2.

47. *The Limits to Organic Photovoltaic Cell Efficiency.* **F. R., Stephen.** 01, 2005, MRS Bulletin, Vol. 30, pp. 28-32. DOI: 10.1557/mrs2005.5.

48. *Optimal film thickness for exciton diffusion length measurement by photocurrent response in organic heterostructures.* **Yang, L.-G., Chen, H.-Z. and Wang, M.** 21, 2008, Thin Solid Films, Vol. 516, pp. 7701–7707. DOI: 10.1016/j.tsf.2008.03.027.

49. **Archer, M. D. and Hill, R.** *Clean Electricity from Photovoltaics.* s.l. : Imperial College Press, 2001. eISBN: 9781848161504.

50. *Two-layer organic photovoltaic cell.* **Tang, C. W.** 2, 1985, Appl. Phys. Lett., Vol. 48, p. 183. DOI: 10.1063/1.96937.

51. *Photoinduced Electron Transfer from a Conducting Polymer to Buckminsterfullerene.* **Sariciiftci, N.S., et al.** 5087, 1992, Science, Vol. 258, pp. 1474-1476. DOI: 10.1126/science.258.5087.1474.

52. *Polymer Photovoltaic Cells: Enhanced Efficiencies via a Network of Internal Donor-Acceptor Heterojunctions.* **Yu, G., et al.** 5243, 1995, Science, Vol. 270, pp. 1789-1791. DOI: 10.1126/science.270.5243.1789.

53. *Efficient Tandem Polymer Solar Cells Fabricated by All-Solution.* **Kim, Jin Young, et al.** 5835, 2007, Science, Vol. 317, pp. 222-225. DOI: 10.1126/science.1141711.

54. *Organic co-evaporated films of a PPV-pentamer and C 60 : model systems for donoryacceptor polymer blends.* **Geens, W., et al.** 2002, Thin Solid Films, Vol. 404, pp. 438-443. DOI: 10.1016/S0040-6090(01)01585-1.

55. *Effect of concentration gradients in ZnPc:C60 bulk heterojunction organic solar cells.* **Wolfgang T., Karl L., Moritz R.** 11, 2011, J. Sol. Mat., Vol. 95, pp. 2981-2986. DOI: 10.1016/j.solmat.2011.06.003.

56. *Efficient thin-film organic solar cells based on pentacene/C60 heterojunctions.* **S., Yoo, B., Domercq and B., Kippelen.** 22, 2004, Appl. Phys. Lett., Vol. 85, p. 3. DOI: 10.1063/1.1829777.

57. **Langa, F. and Nierengarten, J.-F.** *Fullerenes: Principles and Applications.* s.l. : Royal Society of Chemistry, 2007. ISBN-13: 978-0-85404-551-8.

58. *Thermal annealing effects on morphology and electrical response in ultrathin film organic transistors.* **Dinelli, F., et al.** 3, 2004, Synth. Met., Vol. 146, pp. 373-376. DOI: 10.1016/j.synthmet.2004.08.016.

59. *The electronic structure of solid a-sexithiophene.* **Taliani, C. and Blinov, L. M.** 4, 1996, Adv. Mater., Vol. 8, pp. 353-359. DOI: 10.1002/adma.19960080415.

60. *Structural order in conjugated oligothiophenes and its implications on opto-electronic devices.* **F., Denis.** 3, 2000, J. Mater. Chem., Vol. 10, pp. 571-588. DOI: 10.1039/A908312J.

61. *Annealing effect in the sexithiophene:C70 small molecule bulk heterojunction organic photovoltaic cells.* **J., Sakai, et al.** 6-7, 2009, Sol. Energy Mater. Sol. Cells, Vol. 93, pp. 1149-1153. DOI: 10.1016/j.solmat.2009.02.007.

62. *Organic nanofibers from thiophene oligomers.* **L., Kankate, et al.** 1, 2009, Thin Solid Films, Vol. 518, pp. 130-137. DOI: 10.1016/j.tsf.2009.06.003.

63. *Selective Growth of α-Sexithiophene by Using Silicon Oxides Patterns.* **C., Albonetti, et al.** 9, s.l. : Int. J. Mol. Sci., 2011, Int. J. Mol. Sci., Vol. 12, pp. 5719-5735. ISSN: 1422-0067.

64. *Sexithiophene films on ordered and disordered TiO2(110) surfaces: Electronic, structural and morphological properties.* **J., Ivanco, et al.** 1, 2007, Surf. Sci., Vol. 601, pp. 178-187. DOI: 10.1016/j.susc.2006.09.020.

65. *Energy level alignment between sexithiophene and buckminsterfullerene films.* **Y., Ge and J.E., Whitten.** 1-3, 2007, Chem. Phys. Let., Vol. 448, pp. 65-69. DOI: 10.1016/j.cplett.2007.09.075.

66. **J.D., Plummer, D., Micharl and P.D., Griffin.** *Silicon VLSI Technology: Fundamentals, Practice, and Modeling.* s.l. : Prentice Hall, 2000. ISBN-10: 0130850373.

67. *Electron beam deposition system causing little damage to organic layers.* **M., Yamada, M., Matsumura and Y., Maeda.** 19, Thin Solid Films : s.n., 2011, Vol. 519, pp. 6219-6223. DOI: 10.1016/j.tsf.2011.03.056.

68. Epitaxial growth of thin films. *Mansic.* [Online] 2008. [Cited: May 26, 2012.] http://www.mansic.eu/documents/PAM1/Ferro.pdf.

69. *Organic molecular beam deposition: Growth studies beyond the first monolayer.* **Schreiber, F.** 6, 2004, Phys. Stat. Sol. (A), Vol. 201, pp. 1037-1054. DOI: 10.1002/pssa.200404334.

70. *From clusters to fibers: Parameters for discontinuous para-hexaphenylene thin film growth.* **L., Kankate, et al.** 8, 2008, Chem. Phys., Vol. 128, p. 12. DOI: 10.1063/1.2839296.

71. *The surface microstructure controlled growth of organic nanofibers.* **M., Madsen, J., Kjelstrup-Hansen and H.-G., Rubahn.** 11, 2009, Nanotechnology, Vol. 20. DOI:10.1088/0957-4484/20/11/115601.

72. *Electronic properties of interfaces between different sexithiophenes and gold.* **T., Schwieger, et al.** 12, 2005, J. App. Phys., Vol. 97, pp. 123712 (1-5). DOI: 10.1063/1.1929860.

73. **B., Wolfgang.** *Physics of Organic Semiconductors.* s.l. : Willey, 2005. ISBN-10: 352740550X.

74. **Edvard.** Resistive heating explained in details. *Electrical Engineering Portal.* [Online] 2011. [Cited: May 2, 2012.] http://electrical-engineering-portal.com/resistive-heating-explained-in-details.

75. **W., Umrath.** Fundamentals of Vacuum Technology. *Physics Books.* [Online] 1998. [Cited: May 2, 2012.] http://sites.google.com/site/pbookssite/fundamentals-of-vacuum-technology.

76. *The influence of substrate temperature on the structure and morphology of sexiphenyl thin films on Au(111).* **S., Müllegger, et al.** 1, 2007, App. Phys. A, Vol. 87, pp. 103-111. DOI: 10.1007/s00339-006-3845-0.

77. *Polymorphism and Charge Transport in Vacuum-Evaporated Sexithiophene Films.* **B., Servet, et al.** 10, 1994, Chem. Mater., Vol. 6, pp. 1809-1815. DOI: 10.1021/cm00046a039.

78. *Polymer:fullerene bulk heterojunction solar cells.* **Nelson, J.** 10, 2011, Materials Today, Vol. 14, pp. 462-470. ISSN: 1369 7021.

79. *J-aggregation in alpha-sexithiophene submonolayer films on silicon dioxide.* **E., Da Como, et al.** 13, 2006, J. Am. Chem. Soc., Vol. 128, pp. 4277-4281. DOI: 10.1021/ja056060s.

80. **C., Brabec, U., Scherf and V., Dyakonov.** *Organic Photovoltaics.* s.l. : Wiley, 2008. ISBN: 978-3-527-31675-5.

81. *Orientation of α-Sexithiophene on Friction-Transferred Polythiophene Film.* **T., Mizokuro, C., Heck and N., Tanigaki.** 1, 2012, J. App. Phys. Chem. B, Vol. 116, pp. 189-193. DOI: 10.1021/jp207487z.

82. *On the function of a bathocuproine buffer layer in organic photovoltaic cells.* **M., Vogel, et al.** 16, 2006, App. Phys. Let., Vol. 89, p. 163501 (3 pages). DOI: 10.1063/1.2362624.

83. **Rohde, R. A.** Solar Radiation Spectrum. *Global Warming Art.* [Online] 2007. [Cited: April 17, 2012.] http://www.globalwarmingart.com/wiki/File:Solar_Spectrum_png.

84. *Organic solar cells: an overview focusing on active layer morphology.* **L., Benanti T. and D., Venkataraman.** 1, 2006, Photosynthesis Research, Vol. 87, pp. 73-81. DOI: 10.1007/s11120-005-6397-9.

85. *Efficient Vacuum-Deposited Organic Solar Cells Based on a New Low-Bandgap Oligothiophene and Fullerene C60.* **K., Schulze, et al.** 21, 2006, Adv. Mater., Vol. 18, pp. 2872-2875. DOI: 10.1002/adma.200600658.

# **APPENDIX 1** NREL Research Cell Efficiency Records over the years.

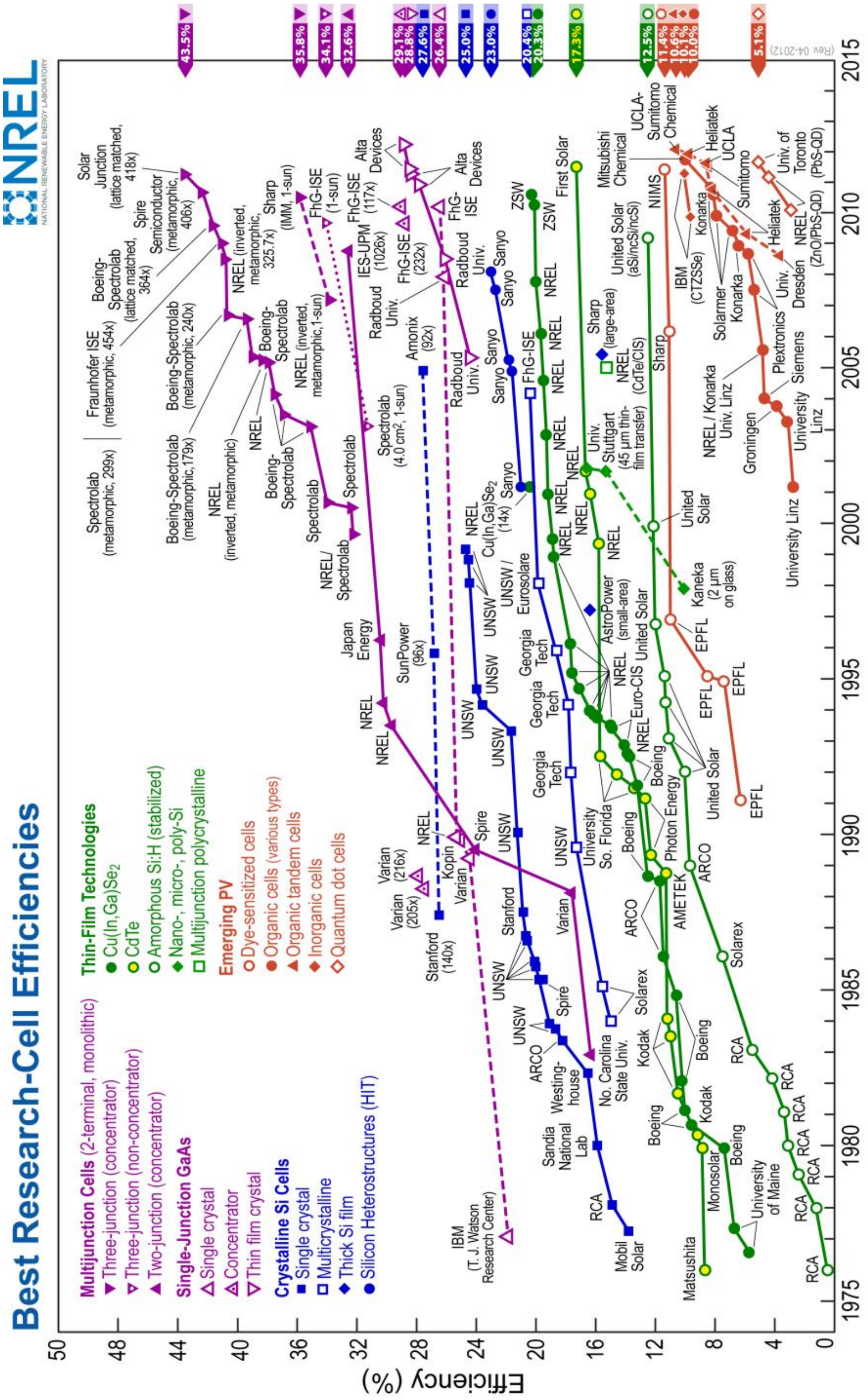

# APPENDIX 2 Graphical illustration of the connection of the peripheral equipment to the deposition chamber.

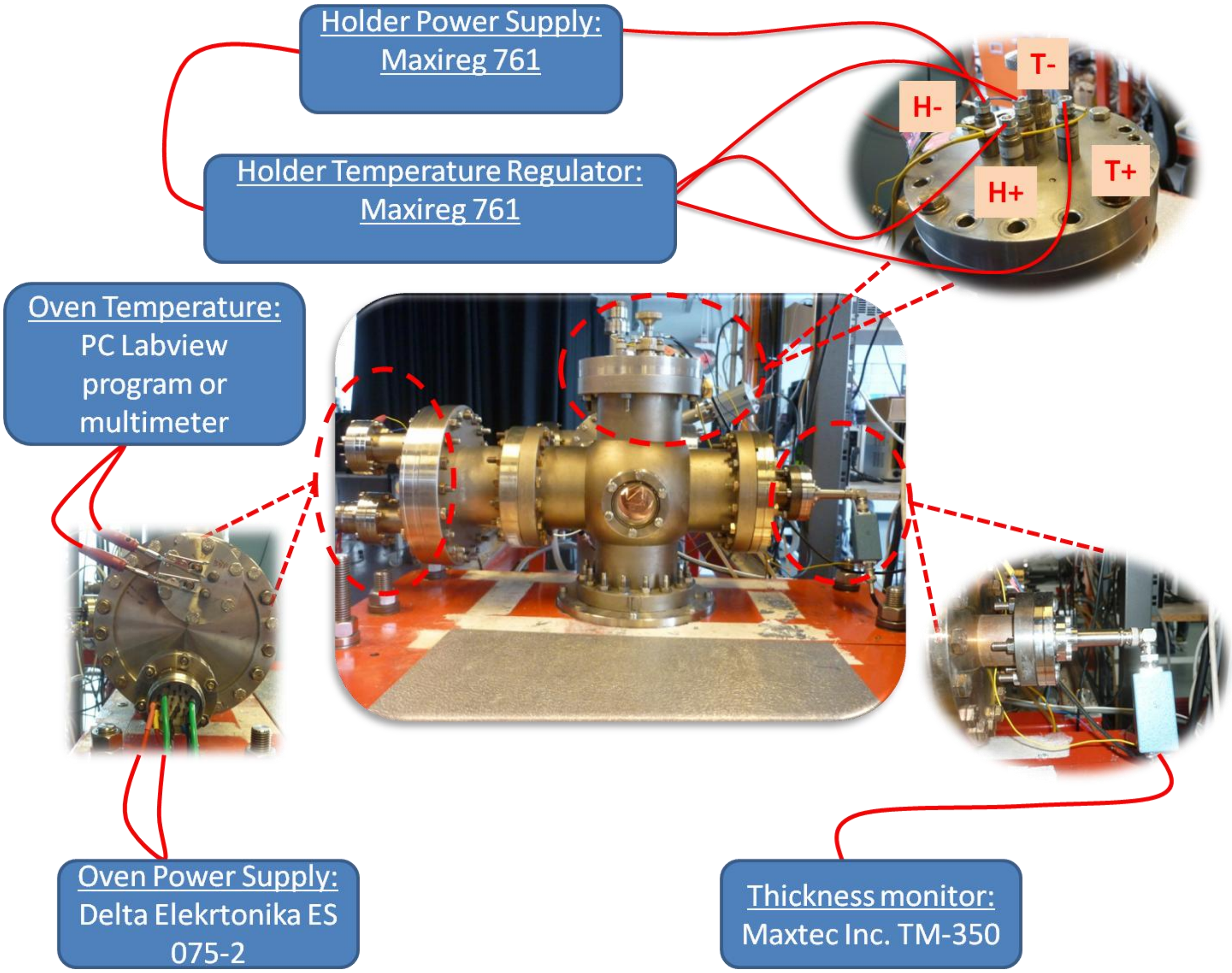

# APPENDIX 3 Oven plate connector support designs.

**Front view**

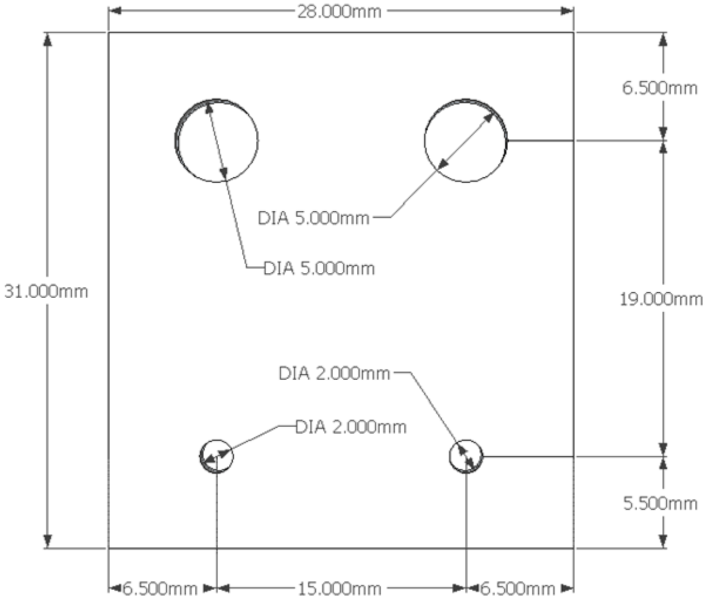

**Rear view**

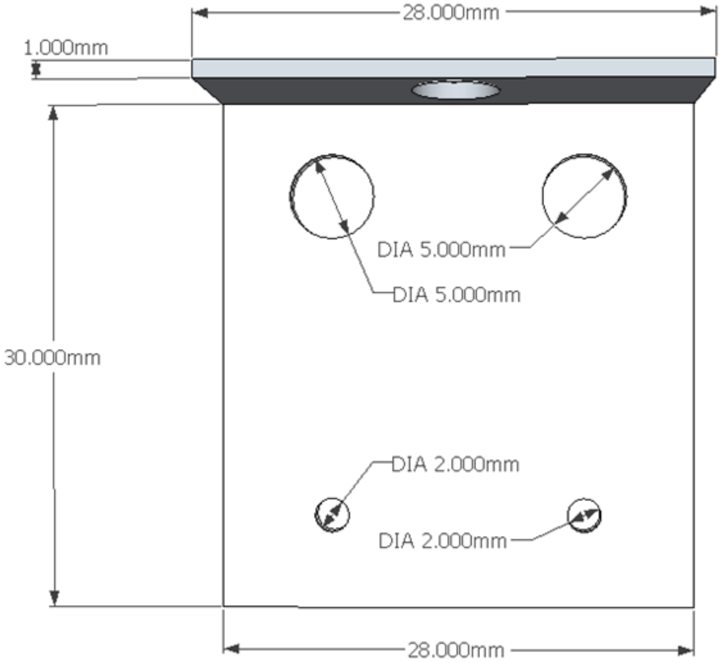

## Left/Right view

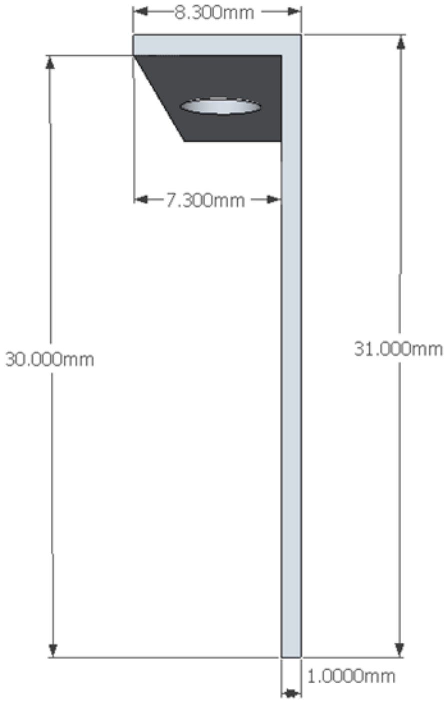

## Top view

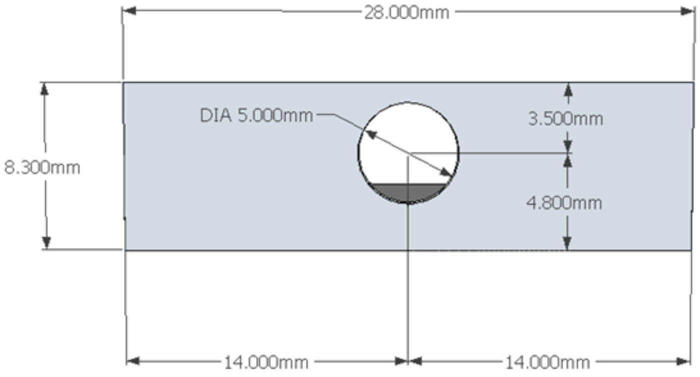

## Bottom view

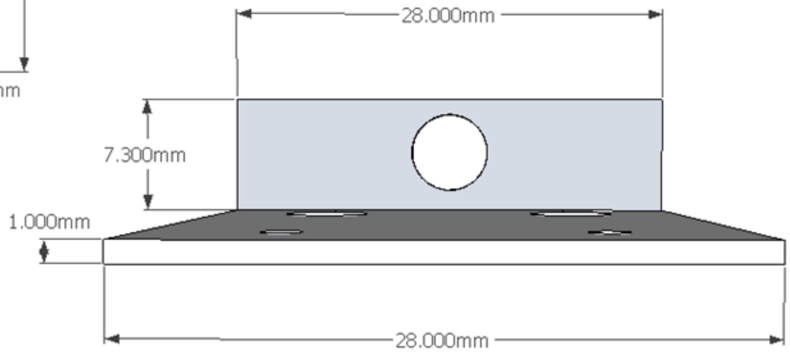

# APPENDIX 4 Process recipe for sample preparation, metal deposition and organic material deposition.

| Step # | Process | Description |
|---|---|---|
| **Wafer selection and pre-cleaning** | | |
| **1** | Wafer type | Glass wafer, BK-7, 4", 500µm thick, double side polished |
| **2** | Pre-cleaning | 1) Sonication in acetone, Time=20min.<br>2) Rinse sequence: Acetone->Isopropanol<br>3) Blow dry |
| **Dicing a wafer using: DISCO DAD-2H/5** | | |
| **3** | Wafer dicing | Dice the BK-7 wafer into 25mm x 25mm squares<br>CAUTION! Carefully crack the wafer into the small squares without scratching the surface. |
| **Post-cleaning** | | |
| **4** | Post-cleaning | 1) Sonication in acetone, Time=20min.<br>2) Rinse sequence: Acetone->Isopropanol<br>3) Blow dry<br>Use desired samples and store the rest in a sealed container. |
| **Gold (Au) deposition: E-Beam** | | |
| **5** | Au deposition | - Attach cleaned samples on the proper sample holder<br>- Edit parameters:<br>Deposition rate: 0.5 Å/s<br>Thickness: 20nm<br>After deposition obtain the samples and place them in a sealed container to transfer them to OMDB chamber. |
| **Organic material deposition (OMBD)** | | |
| **6** | Open chamber | 1) Close rough pump valve<br>2) Close turbo pump<br>3) Close ion gauge monitor<br>4) Wait until turbo pump rotation speed=0 (time≈ 30min.)<br>5) Acquire very low flow from nitrogen bottle and attach the tube to the chamber. |

| | | |
|---|---|---|
| | | 6) Slowly open the air valve to start flow into chamber.<br>7) Open the chamber by unscrewing the four screws on top<br>IMPORTANT: Wear gloves!<br>8) Take out the sample holder<br>9) Close the top with aluminum foil to avoid contaminants entering the chamber<br>10) Close the air valve and close the nitrogen flow |
| **7** | Load sample | 1) Unscrew the copper frame<br>2) Load carefully the sample, reattach the frame and tighten it with the screws.<br>3) Put the sample holder back to the chamber and put the screws back on without tightening them |
| **8** | Pumping down | 1) Open the valve for the rough pump<br>2) When pressure reaches $10^{-3}$ Torr, tighten the screws and start the turbo pump.<br>3) Turn on the ion gauge monitor<br>4) Wait until pressure reaches ≈2-3 x $10^{-7}$ Torr prior to any action (Time ≥ 1hour) |
| | **α-6T deposition** | |
| **9*** | Sample holder heat | In case of deposition of α-6T at elevated temperature otherwise go to next step.<br>1) Set the desired temperature on the temperature controller (Altec AL808e)<br>2) Turn on power supply (Maxireg 761), leave current at max and regulate voltage value.<br>3) Wait until desired temperature is reached then go to next step. |
| **10** | Heating the oven | 1) Select Film number: 2 on thickness monitor<br>2) Connect temperature measurement cables (yellow is positive and blue is negative) to T+ and T- of α-6T proper feedtrhoughs<br>3) Connect power cables from power supply (Delta Elektronika ES 075-2)accordingly to H+ and H- of α-6T proper feedthroughs<br>4) Turn on power supply and set current to 0.35 Amps<br>5) Gradually increase supply by steps of 0.1 Amps until it |

| | | |
|---|---|---|
| | | reaches 0.68 Amps for deposition rate of 0.1Å/s<br>**To increase deposition rate increase oven supply!** |
| **11** | Deposition | Oven temperature=310˚C<br>Deposition rate=0.1Å/s<br>Thickness:<br>- 20nm (for α-6T growth behavior test)<br>- 25nm (for solar cell structure)<br>Turn off power supply and wait for deposition rate=0 prior to next deposition |
| **12*** | In case of deposition at elevated temperature close power supply and let sample holder temperature cool down to room T=30˚C prior depositing other materials (Effect of holder temperature on $C_{60}$ and BCP is unknown in our case) | |
| | **$C_{60}$ deposition** | |
| **13** | Heating the oven | 1) Select Film number: 3 on thickness monitor<br>2) Connect temperature measurement cables (yellow is positive and blue is negative) to T+ and T- of $C_{60}$ proper feedthroughs<br>3) Connect power cables from power supply (Delta Elektronika ES 075-2)accordingly to H+ and H- of $C_{60}$ proper feedthroughs<br>4) Turn on power supply and set current to 0.5 Amps<br>5) Gradually increase supply by steps of 0.2 Amps until it reaches 1.1 Amps for deposition rate of 0.1Å/s<br>**To increase deposition rate increase oven supply!** |
| **14** | Deposition | Oven temperature=350˚C<br>Deposition rate=0.1Å/s<br>Thickness<br>- 25nm (for solar cell structure)<br>Turn off power supply and wait for deposition rate=0 prior to next deposition |
| | **BCP deposition** | |
| **15** | Heating the oven | 1) Select Film number: 4 on thickness monitor<br>2) Connect temperature measurement cables (yellow is |

| | | |
|---|---|---|
| | | positive and blue is negative) to T+ and T- of BCP proper feedtrhoughs<br>3) Connect power cables from power supply (Delta Elektronika ES 075-2)accordingly to H+ and H- of BCP proper feedthroughs<br>4) Turn on power supply and set current to 0.3 Amps<br>5) Gradually increase supply by steps of 0.1 Amps until it reaches 0.5 Amps for deposition rate of 0.1Å/s<br>**To increase deposition rate increase oven supply!** |
| **16** | Deposition | Oven temperature=250˚C<br>Deposition rate=0.1Å/s<br>Thickness:<br>- 25nm (for solar cell structure)<br>Turn off power supply |
| **17** | Unload sample | Follow steps 6-8. Unload the sample wearing gloves |
| **Aluminum (Al) deposition (thermal evaporation)** | | |
| **18** | Al deposition | 1) Wear gloves<br>2) Cut a 25mm Al wire and place it in the filament<br>3) Attach sample in the sample holder and place the mask on top<br>4) Pump down chamber until pressure≈2 x $10^{-5}$ Torr<br>5) Turn on rotation<br>6) Slowly increase supply to evaporate the Al wire<br>7) Unload the sample |
| **19** | Create electrode contacts | Apply a small amount of silver paste to create solid contacts with the electrodes |